APPLIED COMPUTATIONAL ELECTROMAGNETICS SOCIETY JOURNAL

April 2026
Vol. 41 No. 04
ISSN 1054-4887

The ACES Journal is abstracted in INSPEC, in Engineering Index, DTIC, Science Citation Index Expanded, the Research Alert, and to Current Contents/Engineering, Computing & Technology.

The illustrations on the front cover have been obtained from the ARC research group at the Department of Electrical Engineering, Colorado School of Mines

Published, sold and distributed by: River Publishers, Broagervej 10, 9260 Gistrup, Denmark

APRIL 2026 REVIEWERS

Intan Sorfina Zainal Abidin
Chakravarthy
Vinh Dang
Junbing Duan
Javad Ebadi
Pere Ferrer
Simone Genovesi
Muyu Hou
Azharuddin Khan
Yashwant Kumar Kolli
Yinghua Lv
Maria Evelina Mognaschi
Mirjana Peric
Sayidmarie
Kannadhasan S.
Sivaprakash S. C.
Fusun Oyman Serteller
Partha Shome
Cheng-An Sun
Mario Versaci
Steven Weiss
Shihyuan Yeh
Wei-Hua Zong

THE APPLIED COMPUTATIONAL ELECTROMAGNETICS SOCIETY JOURNAL

Vol. 41 No. 04 April 2026

TABLE OF CONTENTS

A Comparative Study of Anti-Jamming Beamforming Using Deep Learning in Planar Phased Array Antennas

Aymen Alhamdan[1], Lotfi Laadhar[1], Mohammed Aseeri[2*], Abdullah Dobaie[1], and Hatem Rmili[1]

[1]Faculty of Engineering, Electrical and Computer Engineering Department
King Abdulaziz University, P.O. Box 80204, Jeddah 21589, Saudi Arabia
Aalhamdan0025@stu.kau.edu.sa, lladhar@kau.edu.sa,
adobaie@kau.edu.sa, hatem.rmili@kau.edu.sa

[2]Next Generation Connectivity and Wireless Sensors Institute
King Abdulaziz City of Science and Technology (KACST), Riyadh, Saudi Arabia
masseri@kacst.gov.sa
*Corresponding Author

Abstract – In this study, a deep learning-based beamforming comparative study for anti-jamming applications in 2D-planar phased arrays is presented. For better array architecture benchmarking, three different geometries (circular, rectangular, hexagonal) are considered. Convolutional Neural Network (CNN) is employed to translate a target radiation pattern, generated as an image, directly into the optimal antenna currents. Adaptive antenna array beamforming weights can be estimated efficiently by the deep learning-based MATLAB code according to the desired beam steering angle and the null direction of the jammer. This approach establishes a smart, non-iterative mapping that bypasses traditional optimization algorithms, reducing computation time by up to 260x. Once trained, the model delivers optimal currents and weights in a single and efficient forward pass.

Index Terms – Antenna arrays, anti-jamming, beamforming, deep learning.

I. INTRODUCTION

Active Electronically Scanned Arrays (AESA) provide rapid electronic beam steering, flexible beamshaping, and spatial filtering capabilities that are fundamental to modern radar [1–7], wireless communications [8–10], and electronic-warfare systems [11–13]. The ability to steer beams and place deep nulls enables effective target tracking and interference mitigation without mechanical motion. However, practical AESA operation depends critically on fast, reliable computation of the complex excitation coefficients for large antenna arrays. Traditional adaptive beamforming and null-steering methods (e.g., Minimum Variance Distortionless Response [MVDR], projection-based nulling, optimization-based synthesis) often involve iterative solvers or large linear-algebra operations whose runtime grows unfavorably with array size and can limit system responsiveness in highly dynamic or contested electromagnetic environments. Deep learning has emerged as a promising alternative to reduce runtime complexity by learning a direct mapping from high-level beam specifications or measured field patterns to antenna excitations [14–16]. Several recent works have shown that neural networks can produce near-optimal beamforming weights for specific array architectures or tasks (beam steering, sidelobe shaping, null placement), typically achieving large reductions in online computation time once trained [17–20]. Most deep learning studies, however, focus on a single array geometry or a narrow set of scenarios; systematic comparisons across different planar array geometries are scarce. Such comparative evaluations are important because array geometry affects beamwidth, sidelobe distribution, element coupling, and robustness to constraints-factors that influence the effectiveness of learned mappings and the practical choice of array architecture.

This paper addresses that gap by presenting a comparative study of deep learning-based anti-jamming beamforming across three planar phased-array geometries: uniform rectangular, circular, and hexagonal. We train a convolutional neural network (CNN) that accepts a desired 2D radiation-pattern image (including main-beam direction, side-lobe mask, and jammer direction) and directly predicts the complex excitation coefficients for all array elements. The image-based input encodes the target spatial specifications in a form that is geometry-agnostic, allowing a single modeling

Submitted On: January 21, 2026
Accepted On: May 04, 2026

https://doi.org/10.13052/2026.ACES.J.410401

approach to be applied to different array topologies while preserving spatial relationships in the pattern. Training reference weights are computed using the MVDR beamforming method, which provides optimal interference suppression while preserving the desired signal direction.

The key contributions of this work are:

- A unified CNN framework that translates 2D radiation-pattern images into complex excitation coefficients, enabling non-iterative beam synthesis for large planar arrays.
- A controlled comparative evaluation of three planar geometries (rectangular, circular, hexagonal) with comparable element counts, isolating the influence of geometry on deep learning prediction accuracy, beam-pointing error, sidelobe behavior, and jammer suppression.
- Comprehensive runtime and performance analysis showing that, after training, the CNN yields excitation weights with closely matching beam characteristics to conventional methods while reducing online computation time dramatically (up to $\approx 260\times$ with GPU acceleration in our experiments).
- Practical insights about geometry-dependent behaviors: the rectangular array achieved the best pattern agreement in our tests, while circular and hexagonal geometries exhibited different sidelobe placement characteristics that affected prediction fidelity.

The remainder of the paper is organized as follows. Section II details the array geometries and element placement. Section III formulates the beamforming problem and describes the CNN architecture and training procedure. Section IV presents simulation results, quantitative comparisons against conventional beamforming, runtime benchmarks, and a discussion of geometry-dependent effects. Section V concludes and outlines directions for future work.

II. ARRAYS DESIGN

We have considered three geometries (rectangular, circular, hexagonal) of phased array antennas operating at 3.2 GHz with spacing equal to lambda by 2 (see Fig. 1). The number of elements for the rectangular, circular, and hexagonal arrays are 640, 616, and 632, respectively. We tried to select comparable number of elements for better comparison of their performance when we apply the deep learning technique. The radiating element is assumed to be an isotropic source.

The rectangular array is of length 16λ and width 10λ. The radius of the circular array and the size of each edge of the hexagonal array is 7λ, where λ is the wavelength corresponding to the operating frequency 3.2 GHz.

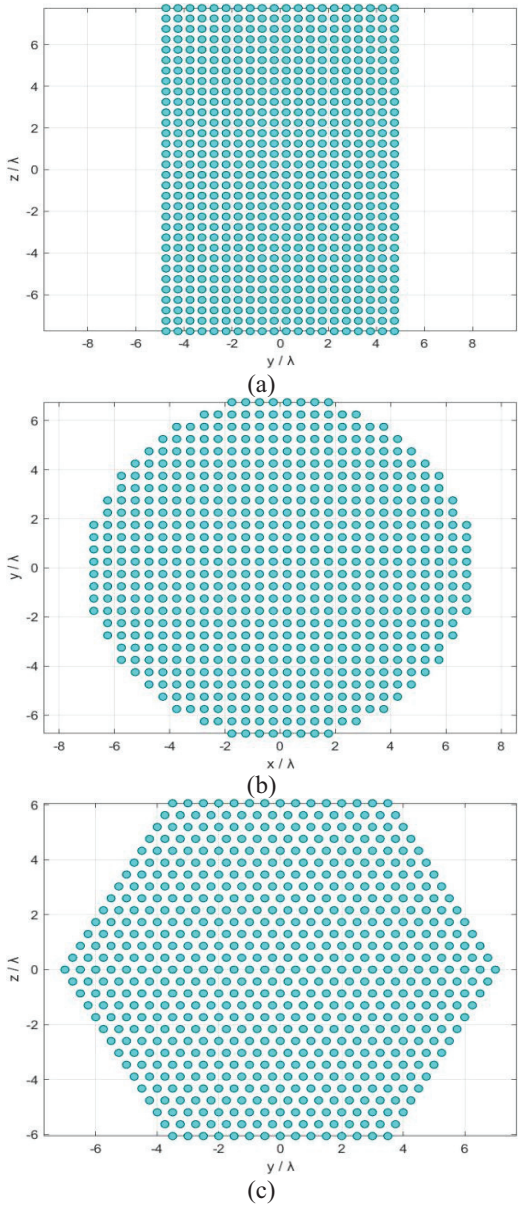

Fig. 1. Geometry of the proposed arrays: (a) rectangular array (640 elements), (b) circular array (616 elements), (c) hexagonal array (631 elements).

III. DEEP LEARNING-BASED BEAMFORMING

A. Problem formulation

We consider a rectangular planar antenna array situated in the *yz* plane where the radiating elements are separated by lambda by 2. The mathematical formulation of the problem is detailed in [21, 22]. The array

factor is given by:

$$F_A = \sum_{n=0}^{N_A-1} c_n e^{jk_0 \mathbf{k}\cdot\mathbf{r}_n}, \tag{1}$$

where $\mathbf{r}_n$ and c_n are the position vector and the complex excitation coefficient of the element n, respectively. N_A is the total number of radiating elements, k_0 is the wavenumber, and $\mathbf{k}$ is the cosine vector.

The array directivity is maximum in the direction (θ_0, ϕ_0), and is expressed by:

$$D_{\max} = K\frac{\max|F_A(\theta_0,\phi_0)|^2}{P_{\text{rad}}} = \frac{K}{P_{\text{rad}}}, \tag{2}$$

where P_{rad} is the total radiated power by the array and K is a constant. The optimization problem consists of determination of the excitation set c_i such that the total radiated power is minimum [21, 22].

In this work, we used the same procedure adopted in [15], which consists of the determination of the real and imaginary parts $(\text{Re}[c_n], \text{Im}[c_n])$ of the complex excitation coefficients c_n in the presence of four constraints: main beam direction $(\theta_{\max}, \phi_{\max})$, jammer direction (θ_j, ϕ_j), side lobe level (SLL), and required suppression level SSL_J.

B. Convolutional neural network architecture

Several CNN architectures were investigated in this work. The final architecture of the selected CNN configuration is illustrated in Fig. 2. Based on experimental evaluation, a 9-layer deep neural network was chosen, consisting of six convolutional layers followed by three fully connected layers, with the last layer serving as the output layer. The network accepts 721×721 single-channel grayscale radiation pattern images as input. Each convolutional layer employs 3×3 kernels with same zero padding. The stride is set to 1 in the first convolutional layer and 2 in the subsequent layers to progressively reduce the spatial resolution and increase the receptive field. Batch normalization and ReLU activation functions are applied after each convolutional and fully connected layer to improve training stability and convergence.

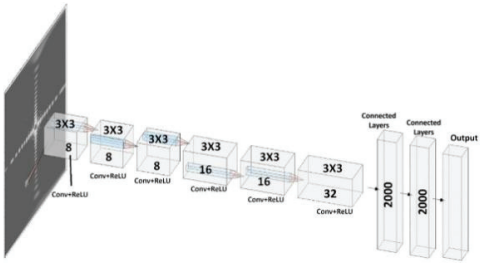

Fig. 2. Architecture of the used CNN.

The number of feature maps increases gradually from 8 to 32 across the convolutional layers, enabling hierarchical feature extraction and progressive learning of spatial features from the radiation pattern. The fully connected section consists of two hidden layers with 2000 neurons each, followed by an output layer whose size depends on the antenna geometry under consideration. Specifically, the network generates a 1280-dimensional output vector for the Uniform Rectangular Array, 1232-dimensional output vector for the Circular Planar Array, and 1262-dimensional output vector for the Hexagonal Array. Each output vector represents the concatenated real and imaginary components of the optimized antenna weights predicted by the network.

C. Training

During the training phase, we have generated 7000 radiation patterns for each phase array geometry (Rectangular, Circular, Hexagonal) corresponding to different values of $(\theta_{\max}, \phi_{\max})$, SLL, (θ_j, ϕ_j), and SLL_J. Each radiation pattern was represented as an 8-bit, single-channel grayscale image with a spatial resolution of 721×721 pixels. The simulated radiation patterns were generated using the MATLAB Phased Array System Toolbox under the following constraints.

Main lobe direction:

$$-35^\circ \le \theta_{\max} \le +35^\circ \quad \text{and} \quad -45^\circ \le \phi_{\max} \le +45^\circ,$$

Side Lobe Level:

$$\text{SLL} = -13 \text{ dB},$$

Jammer (Interference) direction:

$$-20^\circ \le \theta_j \le +20^\circ \quad \text{and} \quad -15^\circ \le \phi_j \le +15^\circ,$$

Required suppression level of SLL:

$$\text{SLL}_J = -30 \text{ dB}.$$

The generated radiation patterns were converted to decibel (dB) scale and normalized using min-max scaling to the range $[0, 1]$ before being used as inputs to the CNN. The target directions were randomly sampled within the specified angular ranges to ensure dataset diversity.

The reference beamforming weights used for training were computed using the MVDR beamforming algorithm, which minimizes the array output power while maintaining a distortionless response in the desired target direction. Consequently, interference and noise are effectively suppressed, leading to significant attenuation in the jammer direction while preserving the main beam.

The complex beamforming weights were separated into real and imaginary components and normalized

prior to training to improve numerical stability. During the training process, the Adam optimizer was used with a learning rate of 0.00025, a batch size of 32, and 60 epochs. The loss function was defined as the Mean Squared Error (MSE) between the predicted weights and the corresponding reference weights.

The dataset was randomly divided into 80% for training, 10% for validation, and 10% for testing. Training, validation, and initial testing were performed on a workstation equipped with an Intel Xeon Gold 6230R processor (20 cores at 2.1 GHz), 64 GB RAM, and a single NVIDIA Quadro RTX 4500 GPU. An additional independent testing stage was conducted on a separate system using a 4-core Intel i7 processor (3.6 GHz) with 12 GB RAM.

IV. RESULTS AND DISCUSSION

For comparison, we have calculated the radiation patterns of the specified arrays under mask constraints using the conventional beamforming method MVDR (true weights) and the deep learning technique (predicted weights). We have chosen to present the results for the following case: $(\theta_{\max}, \phi_{\max}) = (0,0)$, SLL $= -13$ dB, $(\theta_j, \phi_j) = (20,15)$, and $\text{SLL}_J = -30$ dB.

These results are depicted in Fig. 3, which shows the 2D contour plot of the radiation patterns obtained using both true and predicted weights for the three arrays considered.

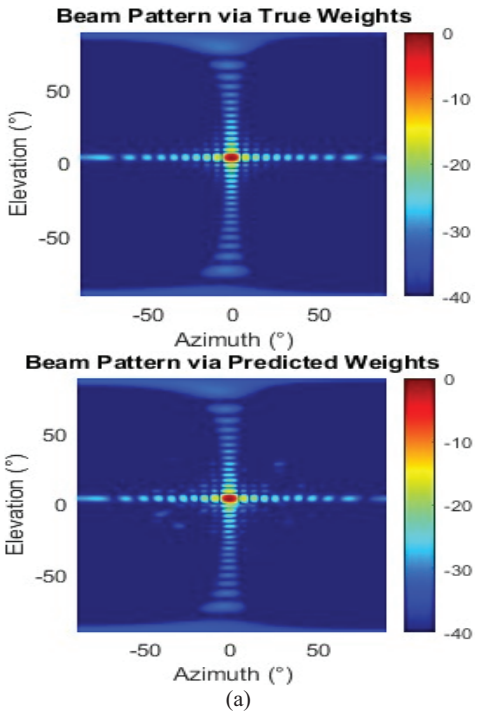

(a)

Fig. 3. Continued

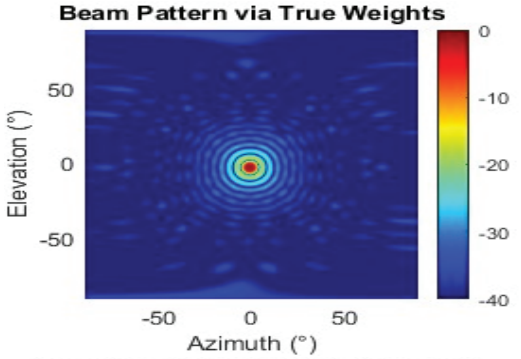

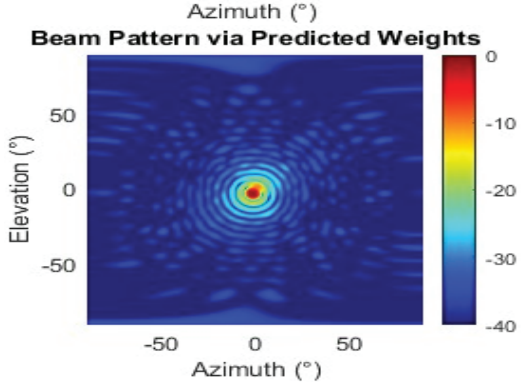

(b)

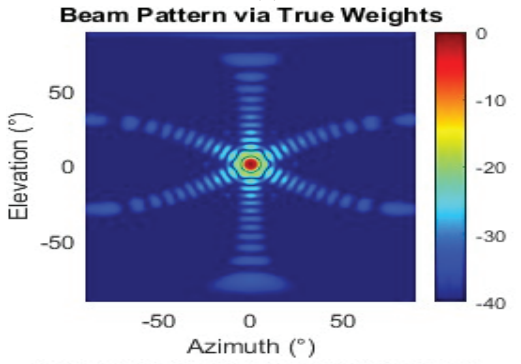

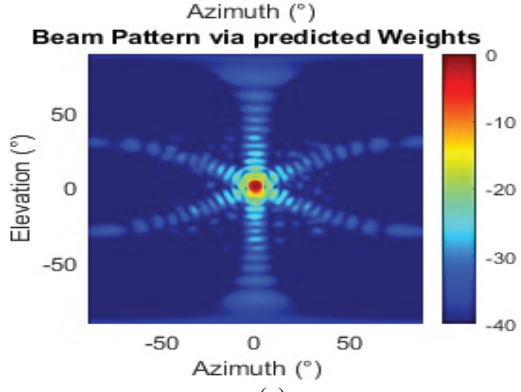

(c)

Fig. 3. 2D contour plot of the radiation patterns obtained separately with true and predicted weights (deep learning) for (a) rectangular array, (b) circular array, (c) hexagonal array.

In Fig. 3, the radiation patterns show the main lobe centered at $(0,0)$ for all the array geometries with

good agreement between patterns calculated with the true values of the excitation coefficients and the patterns determined with the predicted values by using the deep learning method. Analysis of the patterns shows that the agreement is excellent for rectangular, but less effective for circular arrays and hexagonal arrays. It is also noticeable that the secondary lobes are positioned around the main beam in the circular array, while they are distributed in various directions in the other arrays.

To enhance comparison, we have displayed the 2D radiation patterns derived from both true and predicted values in the azimuth and elevation planes, as illustrated in Fig. 4. This representation effectively highlights the alignment between conventional and deep learning beamforming techniques, as well as locating the directions of the target and the jammer within the plot.

Table 1 summarizes the key results for the three array geometries using both MVDR and the proposed deep learning method. As shown, the beam pointing error remains very small for all geometries, with deviations within a fraction of a degree, indicating accurate beam steering. The required interference suppression level is successfully achieved in all cases, with null depths exceeding −30 dB at the jammer direction. Additionally, the sidelobe levels remain within acceptable limits, confirming that the radiation pattern constraints are satisfied. The Half Power Beam Width (HPBW) values obtained using the predicted weights closely match

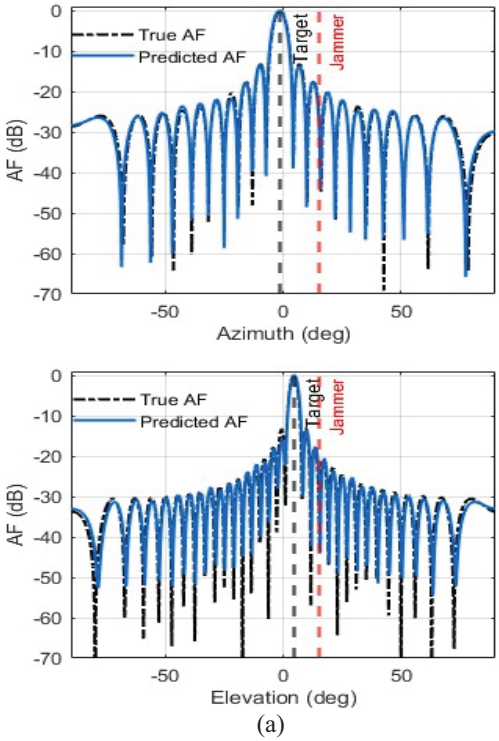

(a)

Fig. 4. Continued

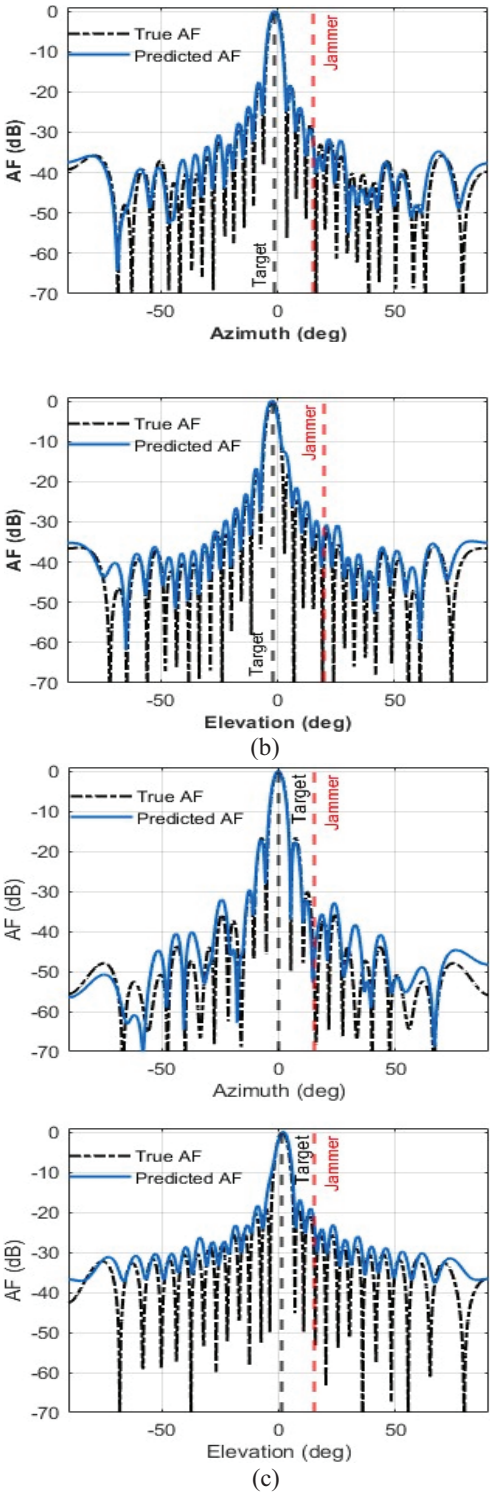

(b)

(c)

Fig. 4. 2D radiation patterns in both azimuth and elevation plans, obtained separately with true and predicted weights (deep learning) for (a) rectangular array, (b) circular array, (c) hexagonal array.

those of the MVDR reference, demonstrating that the beamwidth characteristics are well preserved.

Table 1: Summary of the comparative study results

Parameter	Notation/Description	Rectangular Array	Circular Array	Hexagonal Array
Main lobe direction (°)	$(\theta_{\max}, \phi_{\max})$	$(0,0)$	$(0,0)$	$(0,0)$
Pointing error (°)	Azimuth/Elevation	$-0.25/0.25$	$-0.25/-0.5$	$-2.5/0.5$
Side lobe level dB	SLL Az/Elev	$-14/-17.1$	$-17.8/18.5$	$-16.9/-17.6$
Jammer direction	(θ_J, ϕ_J)	$(20,15)$	$(20,15)$	$(20,15)$
Suppression level dB	SLL_J	$-30/-30.7$	$-31/-32.5$	$-30.1/-34.1$
HPBW (ϕ-plane) (°)	True	5.09	4.20	4.45
	Predicted	5.11	4.26	4.50
HPBW (θ-plane) (°)	True	3.17	4.21	4.45
	Predicted	3.26	4.22	4.77
MSE amplitude	Error	1.4×10^{-4}	4.5×10^{-4}	5.2×10^{-4}
Training time [h]	T_t (with GPU)	8:08	8:17	8:25
Running time [s]	Conventional techniques (CPU)	8.19	8.11	8.13
	CNN (CPU)	0.095	0.075	0.090
	CNN (GPU)	0.038	0.031	0.038

In terms of accuracy, the CNN achieves MSE values in the order of 10^{-4} across all array geometries, confirming the high fidelity of the predicted weights. However, more importantly, the results demonstrate that the proposed method preserves the key beamforming characteristics, including precise beam steering, effective sidelobe control, and strong interference suppression.

In addition to accuracy, the computational efficiency of the proposed approach is evaluated. To ensure a fair and consistent runtime comparison, the execution time for both the conventional MVDR method and the proposed CNN-based approach was measured under a clearly defined timing scope. For the MVDR method, the reported runtime includes the full beamforming computation process, namely covariance matrix estimation, matrix inversion, and weight computation. In contrast, for the CNN-based approach, the runtime corresponds only to the forward inference pass for predicting the beamforming weights.

All runtime measurements were conducted under identical hardware conditions to ensure a fair comparison. Results show that the CNN-based approach significantly reduces the computation time compared to the conventional MVDR method. For the rectangular array, the MVDR method requires approximately 8.19 s on a CPU, whereas the CNNbased approach requires only 0.095 s on a CPU and 0.038 s when executed on a GPU. For the circular array, the MVDR method requires 8.11 s, compared to 0.075 s (CPU) and 0.031 s (GPU) for the CNN-based approach. Similarly, for the hexagonal array, the MVDR method requires 8.13 s, while the CNN-based approach requires 0.090 s (CPU) and 0.038 s (GPU).

It is worth noting that the slight variation in runtime across different array geometries is mainly due to the difference in the number of antenna elements (640 for the rectangular array, 616 for the circular array, and 631 for the hexagonal array). However, this variation does not affect the overall conclusion, as the CNN-based approach consistently achieves a significant reduction in computation time compared to the conventional MVDR method across all configurations. These results correspond to a speed-up of approximately $90\times$ on CPU and up to $260\times$ with GPU acceleration across all array geometries.

In terms of computational complexity, the MVDR method involves matrix inversion with a complexity on the order of $O(N^3)$, where N is the number of antenna elements, whereas the CNN inference has a significantly lower computational cost dominated by convolutional operations. This substantial reduction in computational complexity explains the observed runtime improvement and highlights the suitability of the proposed approach for real-time anti-jamming applications.

V. CONCLUSION

In conclusion, this research presents a comparative study of deep learning-based beamforming techniques for anti-jamming applications utilizing 2D-planar phased arrays. By examining three distinct array geometries (circular, rectangular, hexagonal), we provide a robust framework for array architecture benchmarking. The implementation of a CNN enables the direct translation of target radiation patterns, expressed as images, into optimal antenna currents. This method efficiently estimates adaptive antenna array beam forming weights

based on specific beam steering angles and jammer null directions. Notably, our deep learning approach establishes a smart, noniterative mapping that significantly reduces computation time by up to 260 times compared to conventional optimization algorithms. Once the model is trained, it can generate optimal currents and weights swiftly in a single forward pass, demonstrating the potential of deep learning in enhancing beamforming strategies.

ACKNOWLEDGMENT

This work was funded by the Deanship of Scientific Research (DSR), King Abdulaziz University, Jeddah, Saudi Arabia, under grant No. (135-676-D1435). The authors, therefore, acknowledge with thanks DSR technical and financial support.

REFERENCES

[1] H. Hommel and H.-P. Feldle, "Current status of airborne active phased array (AESA) radar systems and future trends," in *IEEE MTT-S International Microwave Symposium Digest*, vol. 3, pp. 1449–1452, 2005.

[2] R. J. Mailloux, *Phased Array Antenna Handbook*. Norwood, MA: Artech House, 2017.

[3] E. Brookner, "Recent developments and future trends in phased arrays," in *2013 IEEE International Symposium on Phased Array Systems and Technology*, pp. 43–53, 2013.

[4] T. Kinghorn, I. Scott, and E. Totten, "Recent advances in airborne phased array radar systems," in *2016 IEEE International Symposium on Phased Array Systems and Technology (PAST)*, pp. 1–7, 2016.

[5] M. I. Skolnik, *Radar Handbook*, 3rd ed. New York, NY: McGraw-Hill, 2015.

[6] S. Maddio, G. Pelosi, M. Righini, S. Selleri, and I. Vecchi, "Optimization of the shape of non-planar electronically scanned arrays for IFF applications via multi-objective invasive weed optimization algorithm," *Applied Computational Electromagnetics Society (ACES) Journal*, vol. 35, no. 5, pp. 563–571, May 2020.

[7] R. M. Shubair, S. A. Jimaa, and A. A. Omar, "Robust adaptive beamforming using least mean mixed norm algorithm," *Applied Computational Electromagnetics Society (ACES) Journal*, vol. 23, no. 3, pp. 255–262, Sep. 2008.

[8] M. Cheng, Q. Wu, C. Yu, H. Wang, and W. Hong, "Synthesis of a thinned pre-phased electronically steered phased array using excitation control of both the small amplitude dynamic range ratio and low-resolution phase," *IEEE Transactions on Antennas and Propagation*, vol. 72, no. 1, pp. 600–613, Jan. 2024.

[9] D. Xu, Y. Zhang, H. Liu, Z. Wang, J. Chen, X. Li, Y. Wu, and K. Kang, "Ultrawideband filtering phased array antenna based on multilayer PCB and BGA-Via for AESA vertical heterogeneous integration," *IEEE Transactions on Components, Packaging and Manufacturing Technology*, vol. 15, no. 1, pp. 182–195, Jan. 2025.

[10] G. G. Khang, H.-J. Yang, Y. Lee, J. Kim, S. J. Kim, and J. Min Park, "Design results of a wideband active electrically scanned array (AESA) antenna for X-band satellite synthetic aperture radar (SAR) application," in *2024 International Symposium on Antennas and Propagation (ISAP)*, Incheon, Republic of Korea, pp. 601–602, 2024.

[11] S. Kemkemian and M. Nouvel-Fiani, "Toward common radar & EW multifunction active arrays," in *2010 IEEE International Symposium on Phased Array Systems and Technology*, Waltham, MA, USA, pp. 676–681, 2010.

[12] S. Celentano, A. Farina, L. Timmoneri, and G. Foglia, "Co-existence of (AESA) (Active Electronically Scanned Array) radar and Electronic Warfare (EW) systems on board of a military ship," in *2020 IEEE Radar Conference (RadarConf20)*, pp. 1–6, 2020.

[13] P. Sai, S. Shirsat, B. Ramkrishna, A. Bazil Raj, G. R. Shinde, and U. Sateesh, "Improvement for design of digital T/R module of X/Ka/Ku band for EW with multi-functional AESA RADAR using FPGA," in *2022 International Conference on Augmented Intelligence and Sustainable Systems (ICAISS)*, pp. 1508–1512, 2022.

[14] S. Z. M. Hamzah, N. Farihah Abdul Malek, S. Yasmin Mohamad, F. Nadia Mohd Isa, T. Surya Gunawan, and K.-S. Chin, "Deep learning-driven beam-steering for dual-polarized 28 GHz antenna arrays in 5G wireless networks," *IEEE Access*, vol. 13, pp. 80680–80694, 2025.

[15] S. Bianco, M. Feo, P. Napoletano, G. Petraglia, A. Raimondi, and P. Vinetti, "AESA adaptive beamforming using deep learning," in *Proceedings of 2020 IEEE Radar Conference*, pp. 1–6, 2020.

[16] M. Abdullah, A. Zaib, S. Khan, S. Azmat, S. Khattak, B. D. Braaten, and I. Ullah, "Antenna array pattern with sidelobe level control using deep learning," *Applied Computational Electromagnetics Society (ACES) Journal*, vol. 40, no. 5, pp. 612–620, May 2025.

[17] J. Lim, H. Yoo, E. Lee, S. Oh, and J. Lee, "Robust anti-jamming method for large-array radar systems using deep learning-based null-space beamforming," *IEEE Access*, vol. 13, pp. 103599–103612, 2025.

[18] P. Nguyen, V. Nguyen, and V. Do, "A deep double-Q learning-based scheme for anti-jamming communications," in *2020 28th European Signal Processing Conference (EUSIPCO)*, pp. 171–175, 2021.

[19] X. Liu, Y. Xu, L. Jia, Q. Wu, and A. Anpalagan, "Anti-jamming communications using spectrum waterfall: A deep reinforcement learning approach," *IEEE Communications Letters*, vol. 22, no. 5, pp. 998–1001, May 2018.

[20] G. Han, L. Xiao, and H. Poor, "Two-dimensional anti-jamming communication based on deep reinforcement learning," in *2017 IEEE International Conference on Acoustics, Speech and Signal Processing (ICASSP)*, pp. 2087–2091, 2017.

[21] C. A. Balanis, *Antenna Theory: Analysis and Design*. Hoboken, NJ: John Wiley & Sons, 2016.

[22] G. Oliveri, G. Gottardi, F. Robol, A. Polo, L. Poli, M. Salucci, M. Chuan, C. Massagrande, P. Vinetti, and M. Mattivi, "Codesign of unconventional array architectures and antenna elements for 5G base stations," *IEEE Transactions on Antennas and Propagation*, vol. 65, no. 12, pp. 6752–6767, 2017.

Aymen Alhamdan received the M.Sc. degree in electronic and electrical engineering from Strathclyde University, Glasgow, UK, in 2011. He is currently working toward the Ph.D. degree in Electronic and Computing Engineering at King Abdulaziz University, Jeddah, Saudi Arabia. His research interests are antenna array design and deep learning.

Lotfi Laadhar received his Engineering and Ph.D. degrees in Telecommunications from High Institute of Communications of Moscow, Russia, in 1985. From 1990 to 2001, he was Assistant Professor at the Air Force Academy in Tunis, Tunisia. From 2001 to 2012, he was Assistant Professor at College of Telecommunications of Jeddah. September 2012 to June 2015, he was Associate Professor at King Abdulaziz University-North Jeddah Branch College of Engineering. He became Electrical Engineering Department Chair in September 2015 and Associate Professor, King Abdelaziz University College of Engineering, Electrical Engineering Department. His research activities include wireless protocols, management of VSAT (Very Small Aperture Terminal) services such as IP connect and IP access, including internet through the satellite (one-way and the 2-way), in addition to antennas and metasurfaces.

Mohammed Aseeri is currently Full Professor at King Abdulaziz City for Science and Technology (KACST), Saudi Arabia, working within the National Center for Radar and Electronic Technology, and serves as Co-Principal Investigator at the Center of Excellence for Microwave Sensor Technology (CMST), a joint initiative between KACST and the University of Michigan, USA. He received his Bachelor's and M.Sc. degrees in Electrical and Computer Engineering (Electronics and Communications) from King Abdulaziz University, and his Ph.D. in Electronics from the University of Kent, Canterbury, UK. He is a certified Consultant Engineer by the Saudi Council of Engineers (SCE) and holds a Project Management Professional (PMP) certification from PMI. He has gained international research experience through his work as a researcher at the Australian National University (ANU) and the University of Canberra (UC). His professional experience includes managing and supervising advanced electronic surveillance systems and leading multiple national-level projects. His research interests focus on radar systems, electronic warfare, signal processing, wireless sensor networks (WSN), and AI-integrated intelligent sensing systems, including anti-jamming techniques and advanced beamforming for phased array antennas. He is also actively engaged in innovation, technology localization, and the development of smart IoT-based solutions for environmental monitoring and infrastructure protection. He is a senior member of IEEE and IET and has authored numerous scientific publications in highimpact journals and international conferences. He also holds several patents and contributes actively to advancing research, innovation, and strategic technology development.

Abdullah Dobaie received his B.Sc. in 1981 and M.Sc. in 1989, both in Electronic and Communication Engineering from King Abdulaziz University in Saudi Arabia, and Ph.D. in 1995 from Colorado State University, USA. He has supervised many masters and doctoral students in electrical and communication area and has directed many projects concerning communication, digital filters, antenna, and digital signal processing. His recent interests include adaptive communication systems, digital image processing, wave propagation, and communication networks.

Hatem Rmili (Senior Member, IEEE) received the B.S. degree in physics from the Science Faculty of Monastir, Tunisia, in 1995, and the DEA diploma (Master) from the Science Faculty of Tunis, in quantum mechanics, in 1999. He received the Ph.D. degree in physics (electronics) from the University of Bordeaux 1, France, in 2004. From December 2004 to March 2005, he was a research assistant in the PIOM laboratory at the University of Bordeaux 1. From March 2005 to March 2007, he was a Postdoctoral Fellow at the Rennes Institute of Electronics and Telecommunications. From March to September 2007, he was a Postdoctoral Fellow at the ESEO engineering school, in Angers. From September 2007 to August 2012, he was an assistant professor with the Mahdia Institute of Applied Science and Technology (ISSAT), Department of Electronics and Telecommunications, Tunisia. He was an Assistant/Associate/Full Professor (from 2012 to 2024) with the Electrical and Computer Engineering Department, Faculty of Engineering, King Abdulaziz University, Jeddah, Saudi Arabia. In March 2024, Rmili joined Prince Sultan Defense Studies and Research Center (PSDSARC), Riyadh, as Radar Systems Expert. Rimli's research interests concern applied electromagnetic applications involving radar, antennas, AESA, metamaterials, and metasurfaces. The main targeted applications are reconfigurable antennas for multi-standard wireless communications systems, security of chipless RFID systems with fractal tags, terahertz photoconductive antennas for infra-red energy harvesting, UWB nano rectennas for collection of solar energy, phase shifters for low-cost 5G communication systems, radar beamforming, high power microwave, and microwave absorbing materials for stealth technologies.

Air-to-Ground Path Loss Modeling in UAV Networks Via GSA-Based Hyperparameter Optimization

Pham Thi Quynh Trang[1,2], Nguyen Thi Phuoc Van[3], Duong Thi Hang[4], Dinh Trieu Duong[2,*], and Trinh Anh Vu[2]

[1]Department of Electronic Engineering
Hanoi University of Industry, Hanoi, 100000, Vietnam
pham.trang@haui.edu.vn

[2]Department of Electronic and Telecommunication Engineering
Vietnam National University, Hanoi, 100000, Vietnam
duongdt@vnu.edu.vn, vuta@vnu.edu.vn
*Corresponding Author

[3]Department of Information Technology
Thanh Do University, Hanoi, 100000, Vietnam
ntpvan@thanhdouni.edu.vn

[4]Department of Electronic and Telecommunication Engineering
Electric Power, Hanoi, 100000, Vietnam
hangdt_dtvt@epu.edu.vn

***Abstract* –** In Unmanned Aerial Vehicle (UAV) communications, Air-to-Ground (A2G) channel modeling is complex due to high mobility and environmental dynamics. While Machine Learning (ML) and Deep Learning (DL) techniques have been adopted to improve prediction accuracy over traditional empirical models, their performance remains highly dependent on hyperparameter configuration. Recent techniques such as Random Search and Bayesian Search are commonly used for hyperparameter tuning; however, they often struggle with convergence efficiency and prediction stability. To address these challenges, this study aims to develop a hyperparameter tuning framework based on the Gravitational Search Algorithm (GSA) to enhance the predictive performance of ML-based A2G models. The framework is applied to K-Nearest Neighbors (KNN), Decision Tree (DT), Random Forest (RF), and Long Short-Term Memory (LSTM) models at 1 GHz, 2 GHz, and 5.8 GHz. Experimental results demonstrate that GSA-optimized models demonstrate improved predictive stability and competitive accuracy, with GSA-LSTM and GSA-RF achieving an Root Mean Square Error (RMSE) of 5.46 dB, representing a 56% improvement over the free-space model. The proposed approach demonstrates improved robustness compared to conventional search strategies.

***Index Terms* –** Air-to-Ground channel modeling, Bayesian search, deep learning, gravitational search algorithm, hyperparameter optimization, machine learning, path-loss prediction, random search, unmanned aerial vehicles.

I. INTRODUCTION

The rapid expansion of 5G and the emergence of beyond-5G (B5G/6G) networks are driving an unprecedented increase in wireless traffic and intensifying the need for adaptable, high-capacity communication infrastructures [1]. Among emerging technologies, UAV have become a prominent trend due to their flexible deployment, strong line-of-sight connectivity, and effectiveness in enhancing coverage, disaster recovery, and capacity offloading in dense urban environments. As these cutting-edge systems transition toward 6G, the integration of intelligent and autonomous components becomes essential to manage the dynamic nature of A2G links [2, 3].

Accurate A2G path-loss (PL) modeling is critical for UAV-assisted communication, as it directly influences link budget design, coverage estimation, and interference management [4]. Traditional PL models, such as empirical, deterministic, and analytical, often

Submitted On: August 07, 2025
Accepted On: April 17, 2026

https://doi.org/10.13052/2026.ACES.J.410402

struggle to capture the complexity of A2G propagation, particularly in dense urban scenarios. Empirical models (e.g., Log-Distance, Okumura–Hata) fit measurement-based path-loss formulas, offering simplicity and fast computation. Their accuracy, however, is limited to the environments and frequencies used for calibration, making them poorly suited for highly variable A2G channels.

Deterministic models, particularly ray-tracing techniques, rely on physical propagation laws and detailed three-dimensional environmental information to achieve high prediction accuracy. However, their practical applicability is often constrained by substantial computational complexity and the requirement for high-resolution geographical data, which limit scalability in large-scale or dynamically evolving environments [5–7]. Consequently, recent research has increasingly focused on ML and DL-based path-loss modeling approaches, which have demonstrated strong predictive capability across diverse propagation scenarios [8–10].

Despite these advancements, the performance of ML/DL models remains highly sensitive to hyperparameter configuration. It is widely recognized that hyperparameter optimization (HPO) plays a critical role in influencing convergence behavior, generalization performance, and training efficiency [11]. In the context of ML-based path-loss prediction, hyperparameter tuning is frequently conducted through manual adjustment or conventional search strategies, which may result in suboptimal convergence and increased computational burden, particularly in complex A2G propagation environments. Furthermore, a unified and systematic optimization framework capable of consistently supporting heterogeneous ML and DL architectures under varying propagation conditions has not been comprehensively investigated.

To address these challenges, this paper proposes a hyperparameter optimization framework based on the GSA for A2G path-loss prediction. The main contributions are:

(i) Development of a GSA-based hyperparameter optimization framework for KNN, DT, and RF models.
(ii) Architecture and hyperparameter optimization for LSTM, including the number of neurons, learning rate, and training epochs.
(iii) A comprehensive evaluation of KNN, DT, RF, and LSTM models for A2G PL prediction using a publicly available dataset in dense urban environments.

The rest of this paper is organized as follows. Section II introduces the system model, while section III presents the path-loss modeling approach. Section IV formulates the optimization problem, and section V describes the proposed GSA-based solution. Numerical results and discussions are provided in section VI, and conclusions are drawn in section VII.

II. SYSTEM MODEL

A. UAV-to-Ground Link

The system model is illustrated in Fig. 1. A communication link is established between a UAV and ground receivers. The UAV hovers at an altitude of 200 meters, while the receivers are located 2 meters above ground. The A2G communication channel is characterized by three key parameters: the distance between the UAV and the receiver, the elevation angle formed by the transmitter-receiver line, and the carrier frequency. In this work, the carrier frequencies of 1 GHz, 2 GHz, and 5.8 GHz are investigated.

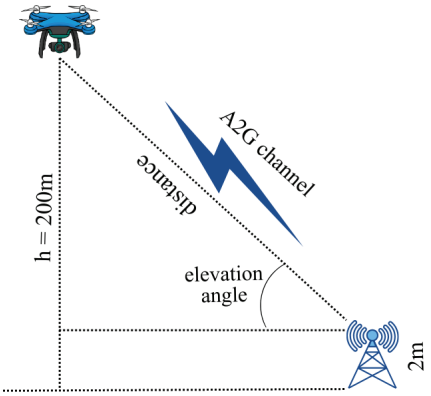

Fig. 1. The system model.

B. The data set

The dataset utilized in this study was obtained from the publicly available Mendeley Data repository [12], which is associated with the work reported in [7]. The dataset was originally generated through electromagnetic ray-tracing simulations using Wireless Insite in a dense urban environment. The surveyed region covers approximately 0.748 km² and includes 1,419 buildings, predominantly high-rise structures. It comprises 36,753 propagation samples collected at carrier frequencies of 1 GHz, 2 GHz, and 5.8 GHz. Each record contains parameters such as the 3D UAV–receiver distance, elevation angle, and measured path loss.

In this work, the dataset is used solely to evaluate the proposed GSA-based hyperparameter tuning framework. No additional simulation or virtual laboratory platform was developed or accessed by the authors.

Each data record consists of the following features: distance, elevation angle, carrier frequency, and receiver location (altitude and 3D coordinates). After preprocessing, the dataset is randomly split into training and testing sets in an 80/20 ratio.

III. PATH LOSS MODELING

Accurate modeling of path loss is essential for predicting the performance of A2G channels. In this study, both traditional free-space models and machine learning-based approaches are considered.

A. The free space model

The free space path loss (FSPL) model is commonly used as a baseline for channel loss estimation. The path loss is expressed as:

$$PL_{CI}(d,f) = PL_{FS,ref}(f) + 10n_{CI}\log_{10}(d) + \xi_{\sigma,CI}. \tag{1}$$

Where $PL_{FS,ref}(f)$stands for the route loss calculated for free space propagation using Friis' law at a reference distance of one meter.

$$PL_{FS,ref}(f) = 20log_{10}\left(\frac{4\pi f}{c}\right). \tag{2}$$

Where: c is speed of light; f is carrier frequency; n_{CI} is the path loss exponent; and $\xi_{\sigma,CI}$ is the shadow fading obey Gaussian distribution with zero mean 0 and standard deviation of σ [13].

Although FSPL provides a simple estimate, it cannot capture complex urban propagation effects, motivating the use of machine learning models.

B. Machine learning-based path loss prediction

Machine learning has recently been applied to model path loss under complex propagation conditions. The performance of each ML model depends on factors such as the dataset, algorithm, network architecture, and hyperparameters. While certain parameters can adjust automatically during training, key hyperparameters, such as the number of layers, number of neurons, and learning rate, must be defined in advance and have a substantial influence on overall model performance [14, 15].

Common hyperparameter optimization methods include:

Grid Search performs an exhaustive evaluation of all defined hyperparameter combinations to identify the optimal model. However, this brute-force approach is often computationally prohibitive and time-consuming [16].

Random Search (RS) improves efficiency by randomly sampling hyperparameters but fails to utilize historical performance data to guide the optimization process, resulting in limited convergence efficiency [17].

Bayesian Optimization (BO) is an informed search strategy that builds a probabilistic surrogate model to guide the selection of hyperparameters based on past evaluations. This iterative learning process makes it highly effective for complex, high-dimensional search spaces where exhaustive testing is infeasible [18].

Metaheuristic algorithms, such as Genetic Algorithm (GA) and Particle Swarm Optimization (PSO), are widely used for complex hyperparameter optimization. GA mimics evolutionary processes but often suffers from slow convergence [19, 20]. Conversely, PSO leverages swarm intelligence for faster convergence but remains sensitive to initialization and prone to local optima trapping [21].

In this work, the GSA is utilized due to its algorithmic simplicity and demonstrated global search capability. It is proposed as an efficient solution for the specific task of ML hyperparameter tuning, providing researchers with another reliable option for accurate A2G path loss estimation.

IV. PROBLEM FORMULATION

Let P_{obs} and P_{pre} denote the observed and predicted path loss values, respectively. Let $\mathscr{H}$ denote the hyperparameter search space and $x \in \mathscr{H}$ represent a candidate hyperparameter vector. The HPO problem is formulated as minimizing the mean absolute error (MAE):

$$f(x) = min\ \frac{1}{No}\sum_{i=1}^{No}|PL^i_{obs} - PL^i_{pre}(x)|$$
$$\text{s.t.} \quad x \in \mathscr{H}. \tag{3}$$

This formulation constitutes a non-convex optimization problem, where the search space $\mathscr{H}$ typically contains mixed continuous, discrete, and categorical variables. Given the high dimensionality and non-linearity of this space, conventional tuning strategies are often computationally inefficient or prone to suboptimal convergence. Therefore, a global optimization strategy is required to effectively explore the feasible set $\mathscr{H}$. In the next section, the GSA is introduced as a suitable metaheuristic framework to address this challenging optimization problem.

V. PROPOSED APPROACH

A. Gravitational search algorithm

The GSA is a population-based metaheuristic inspired by Newton's law of gravity and mass interactions [22]. In GSA, each agent (candidate solution) is treated as an object whose mass reflects the quality of its solution. Better solutions correspond to heavier masses that exert stronger gravitational forces, attracting other agents towards promising regions of the complex search space. This mechanism facilitates simultaneous exploration (global search) and exploitation (local refinement).The gravitational force $F_{ij}(t)$ exerted by agent j on agent i at time t is calculated based on their masses

and distance:

$$F_{ij}(t) = G(t)\frac{M_i(t) \times M_j(t)}{R_{ij}(t) + \varepsilon}(X_j(t) - X_i(t)), \quad (4)$$

where $G(t)$ is the gravitational constant, M represents the masses, $R_{ij}(t)$ is the Euclidean distance between agents i and j, and ε is a small constant. The net force (F_i) acting on agent i is the randomized sum of forces from all better agents (Kbest).

$$F_i(t) = \sum_{j \in \text{Kbest}, j \neq i} \text{rand}_j F_{ij}(t). \quad (5)$$

The acceleration (a_i) and subsequent velocity (v_i) are updated based on the net force and inertial mass:

$$a_i(t) = \frac{F_i(t)}{M_i(t)}, \quad v_i(t+1) = \text{rand}_i v_i(t) + a_i(t). \quad (6)$$

Finally, the agent's position X_i, which represents the candidate solution, is updated:

$$X_i(t+1) = X_i(t) + v_i(t+1). \quad (7)$$

GSA has been widely used in various optimization tasks, including hyperparameter tuning in machine learning [23, 24]. However, to the best of our knowledge, no prior work has applied GSA to the HPO problem for A2G channel modeling. In this study, GSA is selected for its simplicity and strong global search capability, which make it well-suited for non-convex optimization. In the A2G path-loss HPO problem, each agent encodes a candidate hyperparameter vector, and its fitness is evaluated based on the model's prediction error (Equation 3). Through iterative updates, GSA effectively explores the search space to identify near-optimal configurations, thereby improving model accuracy and generalization.

B. The hyperparameter tuning algorithm

In machine learning, hyperparameters are predefined configuration variables that control the training process and model structure, such as the number of layers, the number of neurons, or the learning rate. Proper selection of hyperparameters significantly influences model accuracy and generalization performance.

Figure 2 presents the detailed workflow of the proposed GSA-based hyperparameter tuning algorithm for A2G path loss prediction. The process begins with data preprocessing, including normalization and train–test splitting. The preprocessed dataset is then distributed into two parallel branches corresponding to conventional ML models and DL models.

In the ML branch, KNN, DT, and RF models are first initialized with default hyperparameters. In parallel, the DL branch initializes the LSTM architecture and its associated training parameters.

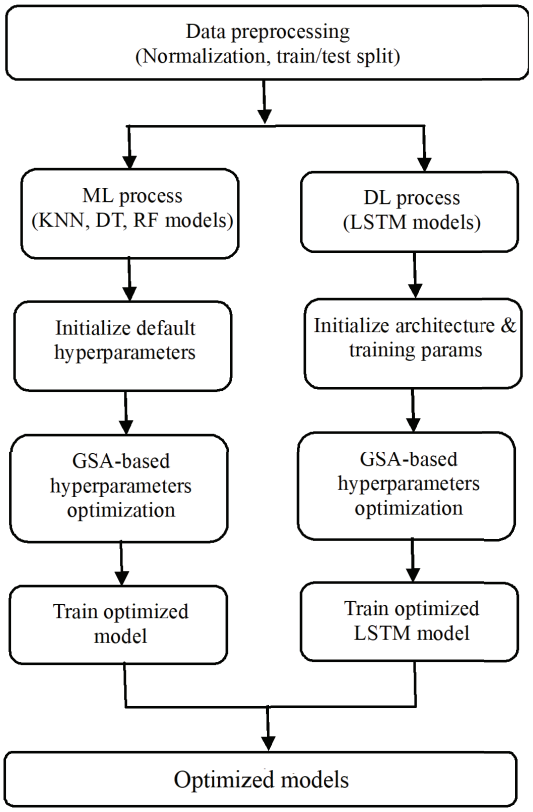

Fig. 2. Proposed GSA-ML/DL process.

For both branches, hyperparameter tuning is formulated as a numerical optimization problem and solved using the GSA. The algorithm searches the predefined hyperparameter space by iteratively generating candidate configurations and evaluating them using a prediction error metric computed on the validation data.

Once the optimal hyperparameter set is identified for each model, the models are retrained using the optimized configuration. Finally, the optimized ML and DL models are evaluated and compared to determine the most accurate model for A2G channel prediction.

This structured and parallel tuning strategy ensures consistent hyperparameter optimization across heterogeneous learning paradigms while maintaining fairness in model comparison.

Set $X = \{x_1, x_2, \ldots, x_k\} \in \mathscr{H}$ as the hyperparameter vector to be optimized, where k is the number of hyperparameters. In the GSA context, each X represents an agent's position.

$\mathscr{D}_{train}$ and $\mathscr{D}_{test}$ denote the training and testing datasets, respectively.

The hyperparameter optimization procedure using GSA is summarized in Algorithm 1.

Figure 3 shows a flowchart of the GSA-based hyperparameter optimization process. The algorithm iteratively updates a population of agents (candidate

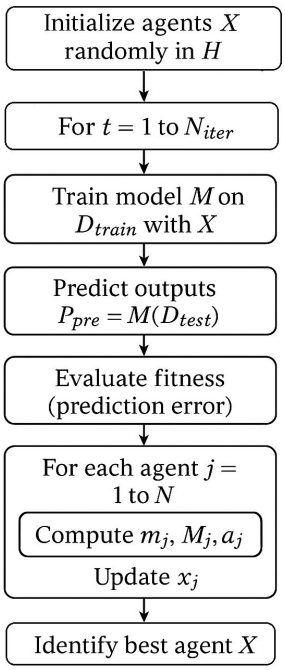

Fig. 3. Flowchart of GSA-based hyperparameter optimization.

Algorithm 1 HPO via GSA

Input: k, N (number of agents), N_{iter} (number of iterations), $\mathscr{D}_{train}$, $\mathscr{D}_{test}$
Output: X = [x1, x2, …, xk], the best hyperparameters
1: Initialize X randomly in $\mathscr{H}$
2: For t = 1 to N_{iter}:
3: Train model $\mathscr{M}$ on $\mathscr{D}_{train}$ with parameters X
4: Predict outputs $PL_{pre} = \mathscr{M}(\mathscr{D}_{test})$
5: Evaluate fitness (Equation 3)
6: For each agent j = 1 to N:
7: For each hyperparameter i = 1 to k:
8: Compute m_j^i, M_j^i, a_j^i (Equation 4–6)
9: Update x_j^i (Equation 7)
10: End for
11: End for
12: Identify the best agent X
13: End for

hyperparameters) based on gravitational forces, evaluates model fitness, and returns the best hyperparameters. The overall time complexity is $O\big(N_{\text{iter}} \cdot (T_{\text{train}} + N \cdot k)\big)$, where N_{iter} is the number of iterations, N is the number of agents, k is the number of hyperparameters, and T_{train} is the model training cost.

VI. RESULTS AND DISCUSSION

Predicted values were generated by feeding the held-out test dataset into the trained ML/DL model, while observed values (ground truth) were sourced directly from the target variable of the test data (as described in Section B).

A. Performance evaluation

Two statistical properties, namely MAE and RMSE [25], are selected as measures to assess the performance of various models. By comparing the anticipated path loss with the test set's data, they may be computed as:

$$MAE = \frac{1}{N}\sum_{i=1}^{N}|y_i - \hat{y}_i|, \tag{8}$$

$$RMSE = \sqrt{\frac{1}{N}\sum_{i=1}^{N}(y_i - \hat{y}_i)^2}. \tag{9}$$

In this:

N denotes the overall count of test samples
$\hat{y}_i$ is the i^{th} predicted and y_i is the i^{th} observed value.

B. Hyperparameters tuning for machine learning

This section presents the results of hyperparameter optimization for the RF, KNN, and DT algorithms in predicting path loss. Although each algorithm provides a large set of hyperparameters, not all of them have a significant impact on model performance. Therefore, in this study, we focus on optimizing only the core hyperparameters that directly influence prediction accuracy, such as depth, number of estimators, split criteria, and neighborhood size [26]. This reduces the search space and makes the optimization more efficient while preserving modeling performance. The reduced sets considered in this study are:

$$\{\mathscr{H}\}_{RF} = \{\textit{n-estimators, max-depth, max-features, min-samples-split, min-samples-leaf}\}.$$

$$\{\mathscr{H}\}_{KNN} = \{\textit{n-neighbors, p, weights}\}.$$

$$\{\mathscr{H}\}_{DT} = \{\textit{max-depth, max-features, min-samples-split, min-samples-leaf}\}.$$

Table 1 shows the accuracy based on MAE and RMSE parameters of each model in predicting A2G channel loss when selecting the hyperparameters based on the suggestions of the optimization methods.

The quantitative results in Table 1 indicate that machine learning models substantially outperform the traditional free-space path-loss model in predicting A2G channel loss. The free-space model yields an MAE of 9.29 dB and an RMSE of 12.63 dB, which are considerably higher than those achieved by data-driven approaches such as DT, KNN, and RF. This confirms that learning-based models are more capable of

Table 1: The accuracy of models

Optimize Method	Model	MAE	RMSE
Default hyperparameters	Decision tree	4.79	7.25
	KNN	5.82	7.95
	Random forest	3.80	5.41
Random Search	Decision tree	5.76	7.89
	KNN	4.13	5.81
	Random forest	5.62	7.69
Bayes Search	Decision tree	5.83	7.98
	KNN	4.09	5.93
	Random forest	4.34	5.90
GSA	Decision tree	4.49	6.43
	KNN	3.98	5.59
	Random forest	3.85	5.46
	Free space	9.29	12.63

capturing the complex propagation characteristics in A2G environments.

It can also be observed that default hyperparameter configurations do not consistently provide optimal performance. While the RF model achieves relatively strong results with default parameters (MAE = 3.80 dB, RMSE = 5.41 dB), the DT and KNN models exhibit noticeable performance gaps under default settings. This highlights the importance of systematic hyperparameter tuning, particularly for models that are sensitive to parameter selection.

To ensure fair comparison, RS, BO, and the proposed GSA-based hyperparameter optimization were conducted within the same search space and using the same dataset. The results show that the GSA-based approach provides competitive and consistently strong performance across different models. For example, the GSA-optimized DT, KNN, and RF models achieve MAE values of 4.49 dB, 3.98 dB, and 3.85 dB, respectively, with corresponding RMSE values of 6.43 dB, 5.59 dB, and 5.46 dB. Although the RF model with default parameters achieves slightly lower RMSE in a single run, the proposed GSA-based framework demonstrates stable and comparable performance across multiple architectures, indicating its effectiveness as a unified and model-independent optimization strategy.

To further analyze the performance characteristics of the optimization strategies, 100 independent runs were conducted for each method (RS, BO, and GSA) using the RF model. RF is selected as a representative ensemble tree-based model due to its practical relevance and sensitivity to hyperparameter configuration.

Figure 4 presents the boxplots of RMSE, R^2, and execution time distributions. Here, R^2 denotes the coefficient of determination, which measures the proportion of variance in the target variable explained by the model [25].

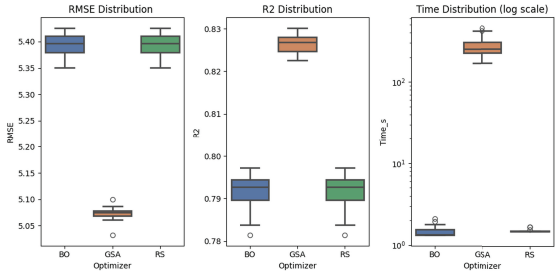

Fig. 4. Distribution of RMSE, $R2$ and execution time for the RF model.

The accuracy distributions indicate that the GSA-based approach achieves the lowest median RMSE and the highest median R^2 among the compared methods. In addition, the interquartile range (IQR) of GSA is relatively narrower, suggesting reduced variability and more consistent convergence behavior across repeated runs. By contrast, RS and BO exhibit slightly larger dispersion, indicating higher sensitivity to stochastic sampling and initialization.

The runtime analysis shows that GSA requires longer computation time compared to RS and BO, which is expected for population-based metaheuristic algorithms. However, this additional cost occurs during the offline hyperparameter tuning phase and does not affect real-time inference once the optimal configuration is determined. Overall, these results illustrate the trade-off between computational overhead and optimization stability, with the proposed method offering improved robustness at the expense of increased search time.

Table 2: Hyperparameters for LSTM model

Hyperparameter	Value
Number LSTM node	44
Number Dense node	35
Learning rate	0.001
Epoch	100

C. Hyperparameter tuning for deep learning

This section presents the results of hyperparameters search for an LSTM-based deep learning model. The path loss prediction model consists of an LSTM layer, a dropout layer, one dense layer, and an output layer. Using Algorithm 1, the searched hyperparameters include the number of LSTM nodes, Dense nodes, and learning rate. A population of 20 agents with 10 iterations was used; the results are summarized in Table 2.

Figure 5 compares the MAE and RMSE of the proposed models with the free space model, showing

that machine learning methods achieve significantly higher accuracy. Accuracy depends on the model and chosen hyperparameters. With the recommended hyperparameters, KNN, RF, and LSTM models yield nearly equivalent A2G path loss predictions, confirming the effectiveness of the proposed hyperparameter search achieve.

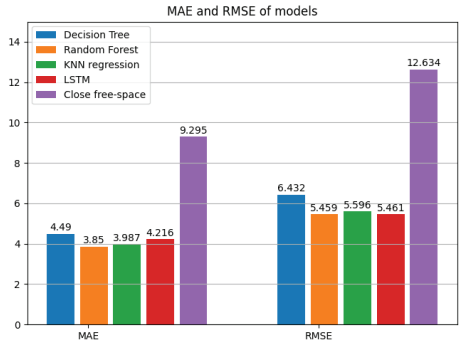

Fig. 5. Predictive accuracy of various ML and DL schemes.

In summary, the experimental evaluation demonstrates the effectiveness of the proposed GSA-based hyperparameter tuning algorithm from three complementary perspectives. First, in terms of predictive performance, the optimized models consistently achieve improved accuracy across different learning architectures, with substantial RMSE reduction compared to the traditional free-space model and competitive results relative to RS and BO. Second, the robustness analysis based on 100 independent runs confirms that the proposed approach provides enhanced convergence stability and reduced variability, as reflected by narrower interquartile ranges and higher median R^2 values. Third, the framework exhibits strong generalizability, as it successfully enhances both conventional machine learning models and deep learning architectures such as LSTM. While the proposed GSA-based approach improves predictive performance and robustness, like other population-based metaheuristic algorithms, it does not provide a strict mathematical guarantee of global optimality. Nevertheless, its empirical results demonstrate clear and consistent advantages over conventional search strategies. Collectively, these findings indicate that the proposed method serves not merely as a model-specific tuning strategy, but as a systematic and architecture-independent optimization framework suitable for reliable A2G path-loss modeling in UAV communication systems.

VII. CONCLUSION

This study proposes a machine learning-based framework for predicting A2G path loss between a UAV and a ground-based user device. In addition, a HPO approach based on the GSA is developed to automate model configuration and improve predictive performance. Numerical results show that the GSA-optimized hyperparameters enhance the accuracy of the A2G path-loss prediction model compared with default configurations and conventional optimization strategies, such as RS and BO. Future work will extend the proposed framework to multi-UAV scenarios and more complex propagation environments to better reflect practical deployment conditions. Furthermore, deep learning models tailored for terahertz (THz) band communications will be investigated, where propagation characteristics exhibit heightened sensitivity to environmental factors.

REFERENCES

[1] M. Z. Chowdhury, M. Shahjalal, S. Ahmed, and Y. M. Jang, "6G wireless communication systems: Applications, requirements, technologies, challenges, and research directions," *IEEE Open Journal of the Communications Society*, vol. 1, pp. 957–975, 2020.

[2] O. T. H. Alzubaidi, M. N. Hindia, K. Dimyati, K. A. Noordin, A. N. A. Wahab, F. Qamar, and R. Hassan, "Interference challenges and management in B5G network design: A comprehensive review," *Electronics*, vol. 11, 2022.

[3] B. Li, Z. Fei, and Y. Zhang, "UAV communications for 5G and beyond: Recent advances and future trends," *IEEE Internet of Things Journal*, vol. 6, no. 2, pp. 2241–2263, 2019.

[4] M. Polese, M. Giordani, T. Zugno, A. Roy, S. Goyal, D. Castor, and M. Zorzi, "Integrated access and backhaul in 5G mmWave networks: Potential and challenges," *IEEE Communications Magazine*, vol. 58, no. 3, pp. 62–68, 2020.

[5] T. S. Rappaport, Y. Xing, G. R. MacCartney, A. F. Molisch, E. Mellios, and J. Zhang, "Overview of millimeter wave communications for fifth-generation (5G) wireless networks—with a focus on propagation models," *IEEE Transactions on Antennas and Propagation*, vol. 65, no. 12, pp. 6213–6230, 2017.

[6] Q. Zhu, M. Yao, F. Bai, X. Chen, W. Zhong, B. Hua, and X. Ye, "A general altitude-dependent path loss model for UAV-to-ground millimeter-wave communications," *Front Inform Technol Electron Eng 22*, vol. 22, p. 767–776, 2021.

[7] N. E.-D. Safwat, F. Newagy, and I. M. Hafez, "Air-to-ground channel model for UAVs in dense urban environments," *IET Communications*, vol. 14, pp. 1751–8628, 2020.

[8] K. J. Jang, S. Park, J. Kim, Y. Yoon, C.-S. Kim, Y.-J. Chong, and G. Hwang, "Path loss model based on machine learning using

multi-dimensional Gaussian process regression," *IEEE Access*, vol. 10, pp. 115061–115073, 2022.

[9] A. Tahat, T. Edwan, H. Al-Sawwaf, J. Al-Baw, and M. Amayreh, "Simplistic machine learning-based air-to-ground path loss modeling in an urban environment," in *2020 Fifth International Conference on Fog and Mobile Edge Computing (FMEC)*, pp. 177–183, IEEE, Paris, France, 2020.

[10] J. Ethier and M. Chateauvert, "Machine learning-based path loss modeling with simplified features," *IEEE Antennas and Wireless Propagation Letters*, vol. 23, no. 7, pp. 2238–2242, 2024.

[11] B. Bischl and M. Binder, "Hyperparameter optimization: Foundations, algorithms, best practices, and open challenges," *Wiley Interdisciplinary Reviews: Data Mining and Knowledge Discovery*, vol. 13, no. 2, p. e1484, 2023.

[12] N. E.-D. Safwat, "Path loss data for UAV channel modeling," Mendeley Data, 2021.

[13] T. S. Rappaport, Y. Xing, G. R. MacCartney, A. F. Molisch, E. Mellios, and J. Zhang, "Overview of millimeter wave communications for fifth-generation (5G) wireless networks—with a focus on propagation models," *IEEE Transactions on Antennas and Propagation*, vol. 65, no. 12, pp. 6213–6230, 2017.

[14] E. Elgeldawi, A. Sayed, A. R. Galal, and A. M. Zaki, "Hyperparameter tuning for machine learning algorithms used for Arabic sentiment analysis," *Informatics*, vol. 8, no. 4, p. 79, 2021.

[15] P. Probst, A.-L. Boulesteix, and B. Bischl, "Tunability: Importance of hyperparameters of machine learning algorithms," *Journal of Machine Learning Research*, vol. 20, no. 53, pp. 1–32, 2019.

[16] P. R. Lorenzo, J. Nalepa, M. Kawulok, L. S. Ramos, and J. Ranilla, "Particle swarm optimization for hyper-parameter selection in deep neural networks," in *Proceedings of the Genetic and Evolutionary Computation Conference*, GECCO '17, pp. 481–488, 2017.

[17] J. Bergstra and Y. Bengio, "Random search for hyper-parameter optimization," *Journal of Machine Learning Research*, vol. 13, no. 10, pp. 281–305, 2012.

[18] V. Nguyen, "Bayesian optimization for accelerating hyper-parameter tuning," in *2019 IEEE Second International Conference on Artificial Intelligence and Knowledge Engineering (AIKE)*, pp. 302–305, 2019.

[19] F. G. Lobo, D. E. Goldberg, and M. Pelikán, "Time complexity of genetic algorithms on exponentially scaled problems," in *Annual Conference on Genetic and Evolutionary Computation*, pp. 151–158, Morgan Kaufmann Publishers, Las Vegas, Nevada, USA, 2000.

[20] F. Itano, M. A. de Abreu de Sousa, and E. Del-Moral-Hernandez, "Extending MLP ANN hyper-parameters optimization by using genetic algorithm," in *2018 International Joint Conference on Neural Networks (IJCNN)*, pp. 1–5, IEEE, Rio de Janeiro, Brazil, 2018.

[21] L. Yang and A. Shami, "On hyperparameter optimization of machine learning algorithms: Theory and practice," *Neurocomputing*, vol. 415, pp. 295–316, 2020.

[22] A. Hashemi, M. B. Dowlatshahi, and H. Nezamabadi-Pour, "Gravitational search algo rithm: Theory, literature review, and applications," *Handbook of AI-based Metaheuristics*, pp. 119–150, 2021.

[23] D. Ezzat, A. E. Hassanien, and H. A. Ella, "An optimized deep learning architecture for the diagnosis of COVID-19 disease based on gravitational search optimization," *Applied Soft Computing*, vol. 98, pp. 106742–106742, 2020.

[24] W. M. Alenazy and A. S. Alqahtani, "Gravitational search algorithm based optimized deep learning model with diverse set of features for facial expression recognition," *J Ambient Intell Human Comput*, vol. 13, no. 2, pp. 829–844, 2020.

[25] J. Isabona and V. M. Srivastava, "Hybrid neural network approach for predicting signal propagation loss in urban microcells," in *2016 IEEE Region 10 Humanitarian Technology Conference (R10-HTC)*, pp. 1–6, IEEE, Agra, India, 2016.

[26] scikit learn. (2025). User Guide [Online]. Available: https://scikitlearn.org/stable/user_guide.html

Pham Thi Quynh Trang received the B.S. and M.S. degrees from VNU University of Engineering and Technology in 2000 and 2006, respectively. She is currently pursuing a Ph.D. degree in telecommunication engineering at VNU. She is interested in wireless communication, wireless sensor network optimization algorithms, digital signal processing, neural networks, applications of nature-inspired algorithms, and FPGA technology.

Nguyen Thi Phuoc Van completed her doctoral degree at Massey University in New Zealand in 2020, specializing in the School of Engineering and Advanced Technology. From 2020 to 2022, she worked as a researcher at the Big Data Integration Research Center at the National Institute of Information and Communications Technology (NICT) in Japan. She was a research fellow at the Centre for Health Research, University of Southern Queensland, Australia, from

2022 to 2024. Currently, she is a lecturer at Thanh Do University in Hanoi, Vietnam. Her research interests encompass communication systems, vital signs sensing systems, sensing technology for monitoring human healthcare conditions, and the application of artificial intelligence in communication and healthcare navigator systems.

Duong Thi Hang has been a lecturer at the Faculty of Electronic Engineering, Hanoi University of Industry since 2000. She received the B.S and M.S. degrees from VNU University of Engineering and Technology in 2000 and 2005, respectively. She is currently pursuing a Ph.D. degree in telecommunication engineering at VNU. Her main research interests are indoor positioning systems, machine learning, pattern classification, and nature-inspired algorithm applications.

Dinh Trieu Duong is a lecturer at Wireless Communication Department of VNU University of Engineering and Technology. His main research interests are Signal Processing for Multimedia Communications, Development of High Performance Multimedia Image, Video Codecs for Real-time Image, Video Transmission over Wire/Wireless Networks.

Trinh Anh Vu is a retired Assoc. Prof. at Wireless Communication Department of VNU University of Engineering and Technology. His main research interests are High-speed Transmission in wireless communications, Massive MIMO systems for 5G, Milimeter wave communications, FPGA design of communication System.

Optimization of a Wideband Rectangular TEM Device by Genetic Algorithms

Shiqi Wang, Yangyi Fu, Jinyu Deng, Guojie Wang, and Jiayu Sun

Department of Intelligence and Engineering
Shenyang City University, Shenyang, Liaoning 116026, China
1609900643@qq.com

Abstract – In recent years, artificial intelligence has been widely introduced into the design of electromagnetic devices. Traditional designs of DC-5.2 GHz wideband rectangular transverse electromagnetic (TEM) devices depend on complex formulas and electromagnetic simulation software such as HFSS and CST Microwave Studio Suite TM 2013. This paper proposes a DC-5.2 GHz rectangular TEM device optimized by genetic algorithms (GAs). The main innovation is the comparison between AI-based optimization and traditional design methods while ensuring excellent wideband transmission performance. The GA-optimized TEM device presents favorable performance and is suitable for cellular radiation experiments in wireless communication systems.

Index Terms – Genetic algorithms, rectangular TEM device.

I. INTRODUCTION

With the rapid development of modern communication technology, wireless communication has become an indispensable cornerstone of social operation and people's daily life, penetrating into every field from industrial production to personal information interaction. In order to adapt to the rapid development of the information society, broadband, high-speed transmission, core network integration, and information personalization have gradually become the main development trends of future wireless communication technology. As a key component in microwave communication systems, the DC-5.2 GHz wideband rectangular transverse electromagnetic (TEM) device [15] directly affects the signal transmission quality, efficiency, and stability of the entire communication system; its performance advantages or disadvantages directly affect the overall operation effect of wireless communication networks and even restrict the breakthrough and upgrading of the entire communication industry. Therefore, optimizing the structural parameters of the DC-6 GHz wideband rectangular TEM device to improve its comprehensive performance is of great strategic significance for promoting the high-quality development of wireless communication technology, meeting the growing demand for high-speed and high-quality communication services, and enhancing the core competitiveness of communication equipment.

Traditional design methods for such TEM devices rely heavily on empirical formulas and professional electromagnetic simulation software. However, these methods not only consume enormous time and computing resources but also have obvious limitations in dealing with complex structural optimization problems, making it difficult to efficiently find the optimal parameter combination, which has become a bottleneck restricting the rapid design and performance improvement of TEM devices. The emergence of artificial intelligence algorithms has broken this predicament and provided a new, efficient technical path for solving complex engineering optimization problems. Among various intelligent optimization algorithms, the genetic algorithm (GA) stands out due to its unique evolutionary mechanism and superior optimization performance and has become the most widely used and most effective algorithm in the optimization of microwave cavity structural parameters [1–4]. Different from other algorithms, the GA simulates the natural selection and genetic variation process of organisms, which enables it to handle multi-parameter coupling, non-linear and multi-constraint optimization problems inherent in TEM device structural design with remarkable advantages. It can encode the structural parameters of the cavity into solution vectors, and through operations such as selection, crossover, and mutation in the iterative evolution mechanism, continuously screen and optimize each parameter, thereby breaking through the limitations of traditional methods, effectively improving the performance of the cavity, and avoiding the blindness of empirical design. The application of GA not only greatly shortens the design cycle of TEM devices but also reduces the dependence on empirical experience and,

Submitted On: January 19, 2026
Accepted On: May 04, 2026

https://doi.org/10.13052/2026.ACES.J.410403

more importantly, it can explore the potential optimal parameter space that traditional methods are difficult to touch, which is of great practical value for promoting the intelligent, high-precision, and efficient design of microwave communication components.

At present, scholars and research teams domestic and abroad have carried out relevant research on the application of intelligent algorithms in the optimization of coaxial cavity structural parameters, but there are obvious differences in research focus, technical paths, and research results between domestic and foreign studies, and there is still significant room for improvement in the overall research level.

Foreign research in this field started earlier and has formed relatively mature technical systems, focusing more on the application of classic intelligent algorithms in the optimization of specific microwave components and the combination with professional electromagnetic simulation tools, among which the GA has been widely and in-depth applied and achieved remarkable results [5–12]. A research team used a GA to optimize the structural parameters of coaxial cavity filters. Through multiple iterations and calculations, the team successfully reduced the insertion loss of the filter by more than 15% and significantly improved its out-of-band suppression performance by 20 dB, which has been widely applied in practical wireless communication systems and achieved good application benefits. Another scholar used particle swarm optimization algorithm to optimize the parameters of coaxial cavity combiner, effectively improving the performance of the combiner and enhancing the signal processing capability of the communication system. In addition, some studies have combined intelligent algorithms with electromagnetic simulation software, such as HFSS and CST. Through collaborative simulation, the performance of filters can be accurately predicted and optimized in the early stages of design, significantly improving design efficiency and shortening product development cycles.

Domestic researchers have also achieved many results in this field. A research group used a GA to optimize the DC-6 GHz wideband rectangular device. By finely adjusting the structural parameters, the insertion loss of the cavity in the target frequency band was reduced by 12%, and the signal transmission stability was significantly improved, perfectly meeting the practical application needs of domestic communication systems. A research institution applied particle swarm optimization algorithm to the design of coaxial cavities and, after multiple experiments and optimizations, achieved optimization of cavity performance and cost reduction [13–19]. At the same time, there are also studies in China dedicated to developing improved versions of intelligent algorithms suitable for optimizing the structural parameters of coaxial cavities, in order to improve the search efficiency and optimization accuracy of the algorithms [20].

However, there are still some shortcomings in current research. On the one hand, some intelligent algorithms are prone to getting stuck in local optimal solutions when dealing with complex coaxial cavity structures, resulting in the inability to find the globally optimal parameter combination, thereby affecting the further improvement of cavity performance. On the other hand, existing research often struggles to balance the relationships between various performance indicators when considering multi-objective optimization. For example, pursuing low insertion loss may lead to a decrease in out-of-band suppression performance.

The significant contributions of this paper are as follows:

(1) improved genetic algorithm;
(2) structural parameter optimization;
(3) DC-5.2 GHz wideband rectangular TEM device.

In view of the above research gaps and the important strategic significance of DC-5.2 GHz wideband rectangular TEM devices in wireless communication systems, this paper proposes a wideband, high-precision, parameter rectangular TEM device, and designs an improved GA for its performance optimization. The proposed GA further improves the global search ability and convergence speed on the basis of the traditional GA, making up for the defect that the traditional GA is prone to falling into local optimal solutions in complex cavity optimization. Compared with traditional electromagnetic simulation software, the proposed improved GA has the advantages of shorter computation time, lower memory occupation, and stronger adaptability to multi-parameter coupling problems. The application of this improved GA not only solves the key technical bottlenecks in the optimization of the DC-5.2 GHz wideband rectangular TEM device but also further enriches the application system of GAs in microwave component design, gives full play to the core value of GAs in intelligent optimization, and provides a new technical reference for the intelligent optimization of similar microwave devices.

The remainder of the paper is organized as follows. Section II conducts theoretical analysis on the designed DC-5.2 GHz wideband rectangular TEM device and its performance evaluation index system, laying a theoretical foundation for subsequent work. Section III verifies the rationality of the proposed device and the effectiveness of the improved GA through simulation and analyzes results to support practical application.

II. THEORY ANALYSIS OF PROPOSED DEVICE

Traditionally, we use formulas to calculate the device parameters. Figure 1 shows the middle section of radiation device. The cross-section size for the middle part of the inner conductor of the rectangular square cone coaxial cavity is obtained by:

$$Z_0 = \frac{188.31}{2\frac{C}{\varepsilon_0} + \frac{w}{h} + \frac{t}{g}}, \tag{1}$$

$$\frac{w}{h} + \frac{b}{g} = 3.7662 - 2\frac{C}{\varepsilon_0}, \tag{2}$$

where C is the unit capacitance between inner and outer conductors, ε_0 is the dielectric constant of media between inner and outer conductors, w is the cross-section width of inner conductor plate, t is the thickness of inner conductor, g is the distance from the inner conductor to the outer conductors on sides, and h is the distance from the inner conductor to the top or bottom outer conductors.

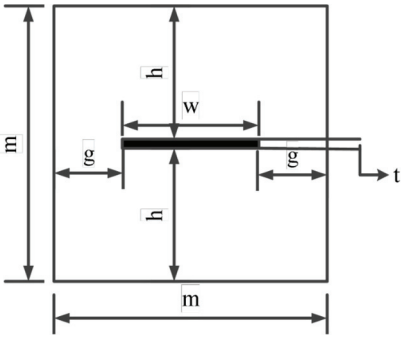

Fig. 1. Calculation model of middle section of radiation device.

Insertion loss refers to the power loss of a signal as it passes through an ultra-wideband coaxial cavity, caused by the cavity's absorption and reflection of the signal, and is typically measured in decibels (dB). The lower the insertion loss, the smaller the energy loss of the signal during transmission, and the better the transmission performance of the cavity for the signal.

Nowadays, the GA is a random search algorithm that simulates the process of biological evolution, and its core idea originates from Darwin's theory of evolution and Mendel's theory of genetics. In GAs, the solution to a problem is encoded into chromosomes, with each chromosome representing an individual, and all individuals forming a population. Individuals in a population continuously evolve through genetic operations such as selection, crossover, and mutation to find the optimal solution.

Coding is the first step of GAs, which maps the solution space of the problem to the genetic space. In optimization problems, GAs iteratively improve the fitness of individuals within a population, ultimately finding the optimal or near-optimal solution. In each generation, the fitness of each individual is first calculated. The fitness function is designed based on the specific optimization problem and is used to measure the adaptability of individuals to the environment, i.e., the quality of the solution represented by the individual. Subsequently, selection, crossover, and mutation operations are performed to generate a new population. As iterations progress, individuals in the population gradually approach the optimal solution. When predefined termination conditions are met, such as reaching the maximum number of iterations, achieving a predetermined solution quality threshold, or observing stable fitness changes, the algorithm stops and outputs the optimal solution.

Parameter settings play a critical role in determining the convergence speed, optimization stability, and final accuracy of the algorithm. Therefore, reasonable parameter configuration should be determined according to the complexity of the optimization problem, the dimension of design variables, and the characteristics of the objective function. The main parameters of the GA and their functions are listed in Table 1, and the corresponding reasonable selection ranges are given based on engineering experience and numerical experiments.

Table 1: Parameter and its function

Parameter Name	**Function**
Population size *N*	Determining population diversity, if *N* is too small, it is prone to premature maturity; if *N* is too large, the computational load will increase
Crossover probability *Pc*	Control the frequency of crossover operations, balance the generation of new solutions with the preservation of high-quality genes
Mutation probability *Pm*	Control the frequency of mutation operations, balance diversity maintenance with random disturbances
Maximum evolutionary generations *G*	Control the number of iterations to avoid the algorithm running indefinitely

In this study, the GA is employed to optimize the structural parameters of the transmission component, with the optimization objective of minimizing the reflection coefficient S_{11}. Strict constraints are imposed to ensure $S_{11} = -10$ dB over the entire DC-5.2 GHz frequency band, while the characteristic impedance Z_0 is stabilized at 50 Ω to achieve good impedance matching.

The geometric variables to be optimized, their physical implications, and design ranges are given in Table 2.

Table 2: Optimized structural variables

Variables	Physical Meaning	Range	Unit
w	width of the cross-section in the middle section of the inner conductor	[120,140]	mm
H_1	length of conical transition section	[350,380]	mm

The fitness function is directly related to the optimization objective, and the degree of achievement of $\boldsymbol{S_{11}}$ needs to be quantified:

$$\boldsymbol{Fit}(\boldsymbol{w},\boldsymbol{H_1}) = \begin{cases} -\boldsymbol{S_{11}}(\boldsymbol{w},\boldsymbol{H_1}) & (\mathbf{S_{11}} \le -\mathbf{10\ dB}) \\ -\mathbf{10}+(\mathbf{S_{11}}+\mathbf{10})\cdot(-\mathbf{5}) & (\boldsymbol{S_{11}} > -\mathbf{10\ dB}) \end{cases}. \tag{3}$$

III. SIMULATION AND ANALYSIS

A. CST simulation and optimization

The electromagnetic simulation and optimization for the rectangular square cone coaxial cavity is carried out with CST Microwave Studio Suite TM 2013. Figure 2 shows the structure diagram of H_1. The impedance matching of the structure is mainly affected by the width w of the middle section of the inner conductor plate and the length H_1 of the transition section, thus the optimization and parameter scanning analysis of w and H_1 is carried out in Fig. 3.

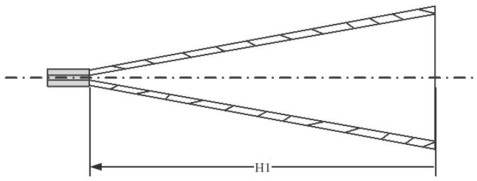

Fig. 2. Structure diagram of identification H_1.

B. Genetic algorithm simulation and optimization

For wideband coaxial cavities, their structural parameters mainly include size, shape, and material properties. Before applying these parameters to intelligent algorithms, the first step is to complete parameter encoding for algorithm recognition and operation. Continuous dimensional parameters such as inner conductor radius, outer conductor radius, cavity length, resonator length, and width can adopt real-number encoding, which directly uses actual values to represent genes, accurately reflecting real parameter values and avoiding

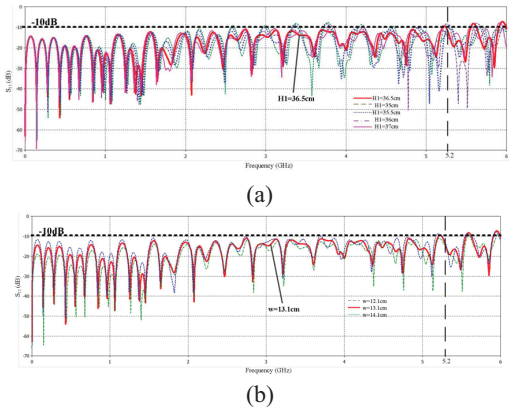

Fig. 3. Simulated $\boldsymbol{S_{11}}$ versus frequency with (a) length of the tapered transition H_1 and (b) width of the inner plate structure.

accuracy loss in the binary encoding-decoding process. The fitness function is a key basis for optimizing intelligent algorithms, which is used to evaluate the performance of the wideband coaxial cavity corresponding to each parameter combination. Then we construct a fitness function based on the main performance indicators of the wideband coaxial cavity, such as insertion loss and out-of-band suppression.

GA testing mainly includes population initialization, iterative evolution, fitness evaluation, and convergence verification. The algorithm is validated by testing whether the optimized cavity parameters meet the performance requirements, and its optimization effect is assessed via repeated tests. The GA parameters are established in Fig. 4 in the Python program.

```
pop_size = 50
max_gen = 100
cross_prob = 0.8
mut_prob = 0.05
w_bounds = [120, 140]
H1_bounds = [350, 380]
```

```
if (gen + 1) % 20 == 0:
    print(f"=== {gen + 1:3d} ===")
    print(f"best parameter: w={best_w:6.2f}mm, H1={best_H1:6.2f}mm")
    print(f"performance: S11={best_s11:6.2f}dB, Z0={best_z0:6.2f}Ω, fitness={best_fit:6.2f}")
    print("-" * 60)
```

Fig. 4. Genetic algorithm parameters.

For the convenience of observing progress, iteration information is output every 20 generations as shown in Fig. 5.

C. Experimental results

Fitting to the optimization results, a rectangular square cone coaxial cavity is fabricated. The experimental prototype is shown in Fig. 6. It is tested with vector network analyzer AV3629B.

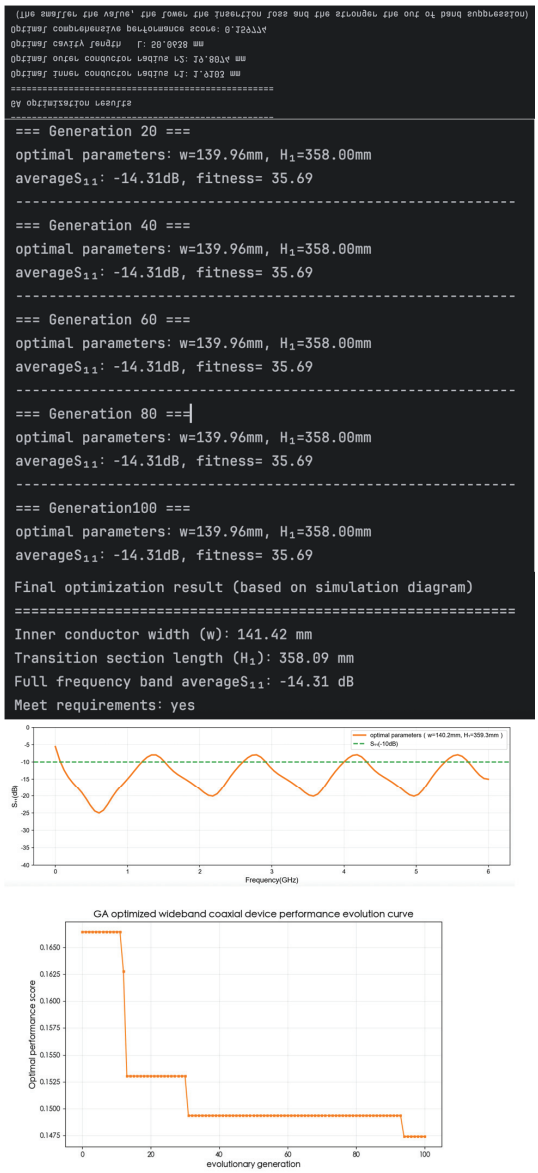

Fig. 5. Genetic algorithm simulation results.

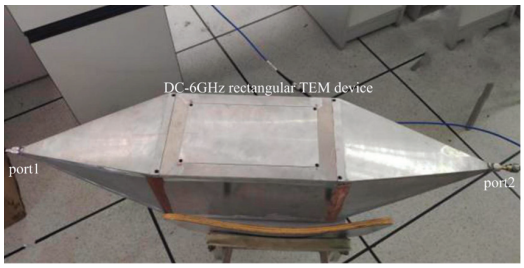

Fig. 6. Photograph of the rectangular device.

The simulated and measured results of the device are depicted in Fig. 7. The reflection coefficient S_{11} is depicted in Fig. 7 (a) and the transmission coefficient S_{21} is depicted in Fig. 7 (b).

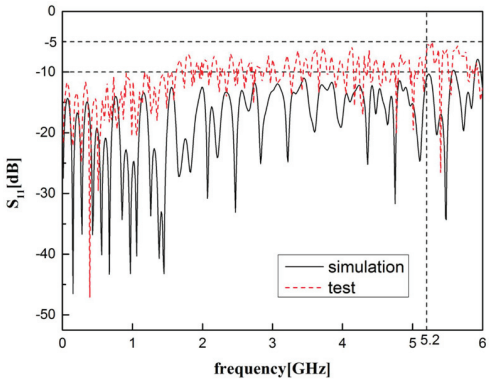

(a)

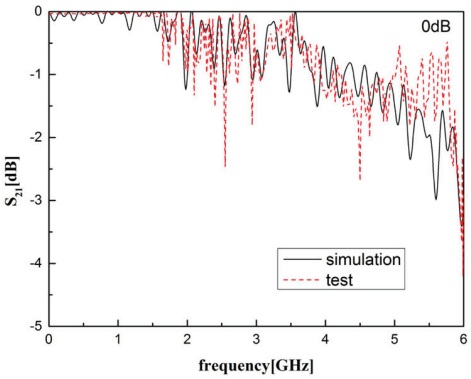

(b)

Fig. 7. (a) Simulated and measured results of reflection coefficient S_{11} from DC-6 GHz and (b) simulated and measured results of transmission coefficient S_{21} from DC-6 GHz.

Comparing the optimized results with the initial structural parameters before optimization, the average insertion loss of the wideband coaxial cavity in the DC-6 GHz frequency band before optimization was 0.5 dB, and the out-of-band suppression in the stopband was only 50 dB. After optimization, both GA and particle swarm optimization algorithm significantly reduced insertion loss and improved out-of-band suppression capability. GA reduced insertion loss by 0.2 dB and increased out-of-band suppression by 15 dB; particle swarm optimization algorithm reduced insertion loss by 0.18 dB and increased out-of-band suppression by 13 dB.

Compared with traditional design methods based on empirical formulas and trial and error methods, traditional design methods can reduce insertion loss to 0.4 dB and achieve out-of-band suppression of 55 dB after multiple adjustments and optimizations. The performance advantages of intelligent algorithm optimization are obvious. GA reduces insertion loss and out-of-band suppression by 0.1 dB and improves by 10 dB, respectively, compared to traditional methods. Particle swarm

optimization algorithm also reduces and improves by 0.08 dB and 8 dB, respectively, in these two indicators compared to traditional methods. This fully verifies the superiority of GA and particle swarm optimization algorithm in optimizing the structural parameters of DC-6 GHz wideband coaxial cavity, which can effectively improve the performance of the cavity and meet the demand of modern communication systems for high-performance coaxial cavities.

GAs have exhibited remarkable effectiveness in optimizing the structural parameters of DC-5.2 GHz wideband rectangular TEM cavities, and their application scope has been further expanded to the optimization of various electromagnetic devices across diverse frequency bands. In the sub-6 GHz (300 MHz–6 GHz) band, the core frequency range for 5G FR1, LTE and Wi-Fi systems, GAs are widely used to optimize coaxial cavity filters, combiners, microstrip antennas, and arrays, effectively reducing insertion loss, improving out-of-band suppression and antenna performance, and solving multi-frequency signal interference to meet integration requirements. For millimeter-wave (6 GHz–300 GHz) devices applied in 5G FR2, 6G and short-range communication, GAs tackle design challenges such as high transmission loss and strict structural precision, optimizing waveguides, dielectric resonator filters, millimeter-wave antennas and radio frequency front-end modules to reduce signal loss, enhance detection accuracy, and realize module miniaturization. GAs are also extended to special electromagnetic devices, including 300 MHz–3 GHz UHF partial discharge sensors, 0.1–10 THz detectors, S/C/Ku/Ka band spaceborne electromagnetic devices, and 915 MHz/2.45 GHz biomedical electromagnetic devices like microwave ablation antennas, effectively improving their sensitivity, environmental adaptability, therapeutic precision, and other performance indicators. The successful adaptive application of GAs in different devices and frequency bands relies on four key technical points: adopting adaptive parameter encoding matching precision requirements, designing multi-objective fitness functions with weighted core performance indicators and NSGA-III algorithm, building a closed-loop GA-EM simulation co-simulation system, and improving GAs for specific scenarios with adaptive crossover/mutation probability, elite retention mechanism, and penalty functions. In general, GAs have broken through the application limitation of DC-5.2 GHz TEM device optimization and been widely applied in the design of electromagnetic devices across the entire frequency spectrum from UHF to THz, effectively solving complex optimization problems such as multi-parameter coupling, non-linearity and multi-constraint in device design, and realizing the optimization of electrical performance, miniaturization, and reliability. With the development of 6G, terahertz communication, intelligent manufacturing, and biomedical engineering, GAs will be further combined with neural networks, reinforcement learning, and other artificial intelligence technologies, evolving toward more intelligent, efficient, and multi-scale optimization, and playing a more important role in the innovative design of next-generation electromagnetic devices.

IV. CONCLUSIONS

This study delves into the application of genetic algorithms in optimizing the structural parameters of a DC-6 GHz ultra-wideband coaxial cavity. Through a detailed analysis of the structure, working principles, and performance metrics of ultra-wideband coaxial cavities, key structural parameters influencing their performance are identified. These parameters are then appropriately encoded to make them suitable for intelligent algorithm processing. Using a genetic algorithm to optimize the structural parameters of the selected wideband coaxial device, after multiple iterations of calculations, the structural parameter combination that significantly improves the performance of the cavity has been successfully identified. The insertion loss optimized by genetic algorithm is reduced to an average of 0.3 dB in the DC-6 GHz frequency band, and the out-of-band suppression reaches 65 dB in the stopband. Compared with before optimization and traditional design methods, the performance advantage of the cavity optimized by intelligent algorithm is obvious, fully verifying the effectiveness and superiority of genetic algorithm in optimizing the structural parameters of wideband coaxial device, providing new ideas and methods for the design of wideband coaxial device.

REFERENCES

[1] Q. Huang, “Research of gigahertz transverse electromagnetic cell,” Dissertation, School of Physical Electronics, 2013.

[2] J. Zhang, X. Wu, and L. Hu, “Research of optimization methods on the ANN-based virtual beamline platform,” *Radiation Detection Technology and Methods*, pp. 1–13, 2025.

[3] A. Yilmaz and I. Kuş, “General CNN model for biomedical image classification via genetic algorithm-based hyperparameter optimization,” *Ain Shams Engineering Journal*, vol. 17, no. 1, pp. 103891–103891, 2026.

[4] X. Yang, G. Lin, and J. Wang, “Optimized fractional-order extended Kalman filtering for IMU-based attitude estimation using the Hippopotamus algorithm,” *Sensors*, vol. 25, no. 22, p. 6942, 2025.

[5] H. Yin, L. Guo, and M. Pan, “ISAL imaging algorithm for spaceborne non-uniformly rotating

targets based on matched Fourier transform and a genetic algorithm," *Remote Sensing*, vol. 17, no. 20, p. 3447, 2025.

[6] S. Lin, W. Zhang, and N. Xu, "Automatic design of CNN architecture based on genetic algorithm and particle swarm optimization," *Evolving Systems*, vol. 16, no. 3, p. 110, 2025.

[7] W. Yuan, "Research on quality assessment method of university distance teaching based on AGG neural network and genetic algorithm," *International Journal of High-Speed Electronics and Systems*, vol. 35, no. 4, p. 2540699, 2025.

[8] T. Zhang, Q. Yin, and S. Li, "An optimized genetic algorithm-based wavelet image fusion technique for PCB detection," *Applied Sciences*, vol. 15, no. 6, p. 3217, 2025

[9] D. Zhao, H. Liu, and A. Xie, "Optimization methods of carbon fiber composite antenna surface precision based on genetic algorithms," *Polymer Composites*, vol. 46, no. 13, pp. 12002–12012, 2025.

[10] S. Singh, S. A. Nandan, and G. Sikka, "Genetic algorithm-based data controlling method using IoT enabled WSNs," *Soft Computing*, vol. 29, no. 5, pp. 1–18, 2025.

[11] S. Tayebnaimi and K. Kiasaleh, "Scintillation index analysis for multi-wavelength Gaussian beams in turbulent underwater channels," *Optical Engineering*, vol. 63, no. 12, p. 128105, 2024.

[12] S. Tayebnaimi and K. Kiasaleh, "On the performance of multi-wavelength underwater optical channels in the presence of optical turbulence," in *2025 IEEE Texas Symposium on Wireless and Microwave Circuits and Systems (WMCS)*, 2025

[13] Q. Zhang, R. Shi, and R. Gou, "Genetic algorithm optimized BP neural network for fast reconstruction of three-dimensional radiation field," *Applied Radiation and Isotopes*, vol. 217, p. 111668, 2025.

[14] D. A. C. Silva and C. A. M. Fernandes, "New approach of blind adaptive equalizer based on genetic algorithms," *Telecom*, vol. 6, no. 1, p. 6, 2025.

[15] H. Mrabet, F. Bahloul, and A. Cherifi, "Capacity optimization of the next-generation passive optical networks based on genetic algorithm," *Optical Fiber Technology*, vol. 88, p. 104041, 2025.

[16] A. Johnson, T. Landecker, and T. Johnson, "Frequency multiplexing excitation network for ultra-wideband coaxial waveguide feeds," *Electronics Letters*, vol. 51, no. 20, pp. 1580–1582, 2015.

[17] J. Wei, F. Liang, H. Feng, and L. Ran, "Condition monitoring of discrete power devices: A data-driven approach with stress quantification and mold temperature sensing," *IEEE Journal of Emerging and Selected Topics in Power Electronics*, vol. 12, no. 3, pp. 2569–2579, 2024.

[18] Y. Wen, Y. Yang, and Y. Li, "A novel short-circuit protection scheme for silicon carbide (SiC) MOSFET module considering operation temperature," *IEEE Transactions on Power Electronics*, vol. 40, no. 8, pp. 10661–10671, 2025.

[19] X. Dong, J. Zhao, Z. Zhou, P. Chen, H. Zhang, and X. Dang, "DOA estimation of non-circular signals with nested arrays: A block tensor sparse representation," *IEEE Transactions on Aerospace and Electronic Systems*, pp. 1–6, 2025.

[20] S. Wang, S. Fang, and P. Chen, "Design and optimization of a wideband rectangular TEM device for cell experiments," *Applied Computational Electromagnetics Society (ACES) Journal*, vol. 37, no. 1, 2022.

Shiqi Wang was born in Shenyang, China. She received the B.Eng. and M.Eng. degrees in information and communication engineering from Dalian Maritime University, Liaoning, China, in 2014 and 2017, respectively. She is currently a Lecturer with the School of Department of Intelligence and Engineering, Shenyang City University. Her current research interests include wideband electromagnetic field, bioelectromagnetics and algorithm optimization method.

Yangyi Fu was born in Jinzhou, China. She received the B.Eng. and M.Eng. degrees in Communication Engineering from Shenyang Ligong University, Liaoning Province, China, in 2021 and 2024, respectively. She is currently a Teaching Assistant with the School of Department of Intelligence and Engineering, Shenyang City University. Her current research interests include wireless communication, signal processing and data encryption.

Jinyu Deng was born in Shenyang, China. She earned a Master of Engineering degree in Software Engineering from Liaoning University, Liaoning Province, China, in 2021. She is currently employed as a Lecturer at the School of Intelligence and Engineering, Shenyang City University. Her current research interests encompass machine learning, image processing, and fuzzy measures.

Guojie Wang was born in Songyuan, China. He received the Bachelor of Engineering (B.Eng.) degree in Network Engineering from Changchun University, Jilin Province, China, in 2019, and the Master of Engineering (M.Eng.) degree in Computer Technology (Electronic Information) from Shenyang Ligong University, Liaoning Province, in 2023. He is currently a Lecturer with the School of Intelligence and Engineering, Shenyang City University. His current research interests include network communication technology and network information security.

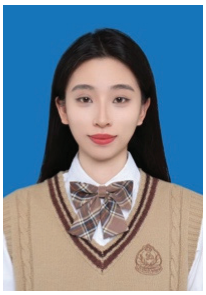

Jiayu Sun was born in Shenyang, China. She obtained a Bachelor of Engineering in Software Engineering from Shenyang University of Technology in 2020 and a Master of Engineering in Computer Science and Technology in 2024. Currently, she serves as an assistant lecturer at the School of Intelligence and Engineering of Shenyang City University, with a primary research focus on computer vision.

Design of All-Dielectric Resonant Metasurface Receiver for Millimeter-Wave Front-Ends

Qiwei Liu[1], Dan Shi[1,*], Yanchi Liu[1], Jintao He[1], Hongbo Tao[2,*], Xiaoyong Liu[2], Zhonghua Xin[3], and Yuhao Jia[3]

[1]School of Electronic Engineering
Beijing University of Posts and Telecommunications, Beijing 100876, China
272044242@qq.com, shidan@bupt.edu.cn, lyc2023018011@bupt.edu.cn, hejint2024@163.com

[2]State Radio Monitoring Center Testing Center, Beijing 102609, China
taohongbo@srtc.org.cn, liuxiaoyong@srtc.org.cn

[3]China Coal Research Institute, Beijing 101320, China
en55015@hotmail.com, jiayuhaobuaa@163.com
*Corresponding Authors

Abstract – In recent years, high-power millimeter waves (HPMMW) have emerged as a severe electromagnetic disturbance that endangers telecommunication networks significantly, as the intense electromagnetic interference induced by HPMMW can damage metallic electronic circuits and front-end devices. To address this issue, this paper proposes an all-dielectric resonant metasurface-based front-end system that enables millimeter-wave components to resist HPMMW-induced damage. The system comprises a laser, an all-dielectric metasurface, an electro-optic resonator, a photodetector, and electronic circuitry. A 3×3 cell-array metasurface antenna is used to capture and transmit a 65 GHz millimeter-wave signal to an electro-optic field sensor. Subsequently, the photodetector converts the optical signal into a demodulated radio-frequency signal, which can be further processed by the subsequent electronic circuitry. With a compact footprint of 7.7×7.7 mm^2 and a high receiver sensitivity of -52 dBm, the proposed system can be integrated with other electronic circuits, facilitating the miniaturization of telecommunication equipment.

Index Terms – All-dielectric metamaterials, Fano resonant effect, high-power millimeter wave (HPMMW), radio frequency front-end.

I. INTRODUCTION

Millimeter waves have been widely utilized in 5 G communication, radar sensors, radio astronomy, remote sensing, imaging, and security screening [1–3]. Millimeter-wave transmitters and receivers are key components for system performance. Meanwhile, high-power millimeter waves (HPMMW) generated by vacuum-electronic traveling-wave tubes or sheet electron beams pose a severe threat to communication systems [4, 5]. HPMMW can disrupt millimeter-wave communication networks by inducing intense electromagnetic interference that damages or destroys electronic circuits.

Therefore, the protection of millimeter-wave systems against HPMMW has become increasingly significant. Since most radio front-end components operating at the millimeter-wave band are typically made of metal [6, 7], HPMMW generates a large current surge that inflicts catastrophic damage by melting metallic interconnects.

According to published literature, an effective method is to apply electromagnetic shielding [8–10]. Although the shield can effectively attenuate electromagnetic energy, millimeter-wave components remain vulnerable because the shield and parts of the components are made of metal, which is meltable under HPMMW. Moreover, the protection circuits that use transient-voltage-suppression (TVS) diodes or metal-oxide varistors (MOV) [11] also perform poorly. A novel circuit with ultra-low capacitance was presented and fabricated using an InGaP/GaAs heterojunction bipolar transistor [11]. Although this Darlington pair is suitable for high-frequency protection from HPMMW, it often works below 20 GHz. In addition, specialized protection modules for electrical equipment against high-altitude electromagnetic pulses (HEMP) and intentional electromagnetic interference (IEMI) have been developed and verified through practical testing, providing feasible engineering solutions for electromagnetic interference shielding [12]. In recent years, an all-dielectric front-end structure has been proposed to replace the metallic

Submitted On: November 23, 2025
Accepted On: April 20, 2026

https://doi.org/10.13052/2026.ACES.J.410404

antenna, particularly suitable for HPMMW applications. Traditionally, the dielectric resonant antenna (DRA) has been investigated in detail [13, 14]. Hsu et al. proposed an effective all-dielectric photonic-assisted radio front-end structure [13]. A device combining an electro-optic crystal field sensor with a textbook DRA was developed, which captured the free-space centimeter-wave RF signal (7.38 GHz) and generated an enhanced electric field on the structure's surface. While this design maintains HPMMW immunity and reasonable receiver sensitivity, it is not optimized for millimeter-wave applications and miniaturized designs. In terms of compact and wideband millimeter-wave antenna design, recent studies have made notable progress. A compact, circularly polarized, crossed-dipole antenna with wide bandwidth was proposed using a split-ring resonator and parasitic patches, providing a valuable reference for miniaturized millimeter-wave front-end antenna design [15]. Meanwhile, a three-dimensional, compact, propeller-shaped, circularly polarized ceiling antenna was developed, further enriching the options for compact antenna structures in communication systems [16]. These works highlight the importance of structural optimization in achieving compact size and excellent performance, aligning with the design goals of the proposed metasurface receiver.

In this paper, an optimized receiver model operating at millimeter-wave frequencies using a metasurface structure is proposed. The proposed receiving antenna exhibits strong resonance at 65 GHz and a small size of 59.29×2.12 mm^3. Meanwhile, compared with traditional DRA antennas, dielectric metasurfaces are much smaller. Presently, metamaterials have been widely applied in antenna design, including minimized cavity resonators, wave-guiding structures, angular-independent surfaces, terahertz switches, and fluid-tunable frequency-agile materials [17–20].

All-dielectric metasurface front-end technologies and the whole system are introduced in section II. Metasurface resonant theory, design of the metasurface antenna, and electro-optic (EO) resonators are illustrated in section III. Simulation results and parametric discussions are presented in section IV. System performance, including system sensitivity measurements, is provided in section V, followed by the conclusion in section VI.

II. RECEIVER DESIGN AND ANALYSIS

A. All-dielectric photonic-assisted radio front-end receiver design

An all-dielectric resonant metasurface receiver is proposed to receive a millimeter-wave signal, immune to HPMMW, while maintaining high receiver sensitivity. As shown in Fig. 1, the photonic-assisted all-dielectric radio-frequency (RF) front-end receiver comprises a laser, a dielectric metasurface, an EO resonator, a photodetector, and electronic circuitry.

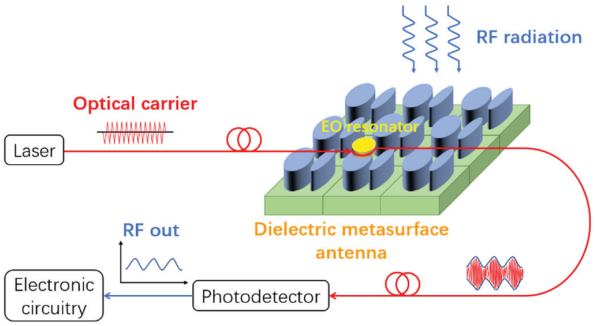

Fig. 1. Components of the all-dielectric photonic-assisted radio front-end receiver.

The incident millimeter-wave signal interacts with the dielectric metasurface, which generates a Fano resonance and consequently an electric-field enhancement at the top of the metasurface. To effectively convert the RF millimeter-wave signal to an optical signal via the $LiNbO_3$ electro-optic disk resonator, the system uses a diamond prism to couple the input optical beam from the laser into the EO resonator. This resonator is positioned in the region of maximum electric-field enhancement on the metasurface to efficiently convert the received millimeter-wave signal into an optical signal. This coupling method is crucial for enabling the subsequent photodetection and signal processing stages [13–21], as shown in Fig. 2.

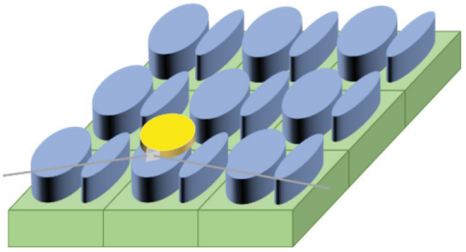

Fig. 2. Using a diamond prism to couple the input optical beam to the EO resonator.

The photodetector converts the optical signal into a demodulated RF signal, which can be further processed by the subsequent electronic circuitry [13–22]. In the entire receiver system, the optical signal is coupled into and transmitted through an optical fiber, thereby enhancing immunity to HPMMW [13].

B. Impact factor analysis of receiver sensitivity

Receiver sensitivity is defined as the minimum detectable incident power when the system carrier-to-noise ratio (CNR) is equal to 1, which can be

calculated as [13]:

$$P_{rf}^{inc} = \frac{(E_{rf}^{inc})^2 A_e}{\eta}, \tag{1}$$

where A_e is the cross-sectional area of the metasurface antenna, and η is the wave impedance of free space (377Ω).

The incident root-mean-square (RMS) RF electric field E_{rf}^{inc} can be written as [13]:

$$E_{rf}^{inc} = \frac{E_m}{\beta}\frac{\varepsilon_{LN}}{\varepsilon_{MT}}, \tag{2}$$

where ε_{LN} and ε_{MT} are the dielectric constants of $LiNbO_3$ and the metasurface antenna, respectively, at microwave frequencies, and β is the field-enhancement factor, which is defined as the ratio of the metasurface-enhanced field strength to the incident free-space field [13].

The electric field E_m experienced by the $LiNbO_3$ electro-optic resonator can be obtained by the formula of the modulation depth m under the condition of CNR = 1 [13–22]:

$$m = \frac{\pi E_m}{E_\pi^{eff}}\frac{P_i}{P_0}, \tag{3}$$

$$E_\pi^{eff} = (4\sqrt{3}\pi^2\lambda)/(9Fn_e^3 r_{33}L), \tag{4}$$

$$CNR = (mRP_0)^2/(2\sigma_T^2) = 1, \tag{5}$$

$$\sigma_T^2 = \sigma_{RIN}^2 + \sigma_{shot}^2 = (N_{RIN})\frac{(RP_0)^2}{2}B + 2qRP_0B, \tag{6}$$

where F is the electro-optic resonator finesse ($F = Q\frac{\lambda \cdot FSR}{c}$, Q is the loaded quality factor), n_e is the refraction index of electro-optic resonator at the operation wavelength $\lambda = 1.55$ μm, r_{33} is the electro-optic coefficient, L is the circumference of the electro-optic disk resonator ($L = 2\pi R_{EO}$), R is the photodetector responsivity, P_i is the input optical power, P_0 is the average optical power at the detector ($P_i = 2P_0$), σ_T^2 is the total variance of noise current generated by relative intensity noise (RIN) power of the source laser (σ_{RIN}^2), shot noise (σ_{shot}^2), and thermal noise power (the thermal noise is negligible because the received power is high enough), N_{RIN} is relative intensity noise of the source laser, q is the elementary charge of 1.6×10^{-19}C, and B is the detection bandwidth [13–22]. E_m is given by:

$$E_m = \frac{2\pi\lambda}{9RP_0Fn_e^3 r_{33}L}\sqrt{6\left[(N_{RIN})\frac{(RP_0)^2}{2}B + 2qRP_0B\right]}. \tag{7}$$

Therefore, receiver sensitivity, namely the minimum detectable incident power per unit bandwidth, is given by:

$$P_{rf}^{inc} = \left(\frac{\varepsilon_{LN}}{\beta\varepsilon_{MT}}\right)^2\left(\frac{2\pi\lambda}{9RP_0Fn_e^3 r_{33}L}\right)^2 \times \left[(N_{RIN})\frac{(RP_0)^2}{2} + 2qRP_0\right]\frac{6A_e}{\eta}. \tag{8}$$

According to (8), better receiver sensitivity can be obtained by increasing the field-enhancement factor β and average optical power P_0, as well as decreasing the metasurface antenna cross-sectional area A_e and the relative intensity noise of the source laser N_{RIN}. Higher field-enhancement factor and smaller cross-section can be realized by means of optimizing the structure of dielectric metasurface according to the principle of Fano resonance. In addition, it is effective to improve receiver sensitivity by increasing the laser power to achieve a higher average optical power and choosing a laser source with better RIN [23].

When the average optical power varies from 1 mW to 100 mW, the receiver sensitivity (minimum detectable free-space power) in different RIN cases is shown in Fig. 3. The parameters used in the analysis are as follows: $FSR = 65$ GHz, $\beta = 25, \varepsilon_{LN} = 35, \varepsilon_{MT} = 22$, $Q = 1.1 \times 10^6, R = 0.8$ AW^{-1}, $r_{33} = 30.8$ pm V^{-1}, $A_e = 6 \times 10^{-5}$ m^2, $n_e = 2.14$, $R_{EO} = 0.34$ mm, and $\lambda = 1.55$ μm.

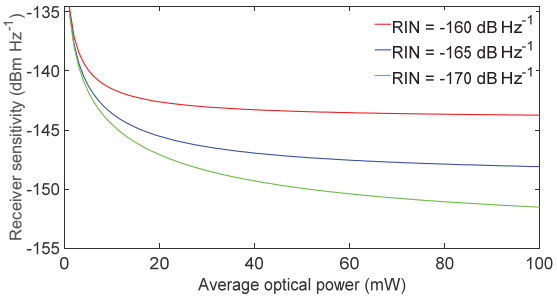

Fig. 3. Receiver sensitivity in different RIN cases when the average optical power varies from 1 to 100 mW.

III. MODEL CHARACTERIZATION

A. Resonance principle of metasurface

Mie and Fano resonances are introduced in this section to illustrate the key parameters for enhancing the received electric field. Mie resonance is produced by the interaction between the dielectric particles and the incident light [21]. Researchers have found that introducing Fano resonance into the design of dielectric metamaterials is the most effective way to increase the resonant quality Q [24–26]. In our proposed structure, the Mie resonance is combined with a Fano resonance to achieve a higher resonant quality factor Q, leading to a stronger electric field.

Fano resonance is a resonant scattering phenomenon characterized by an asymmetric spectral line shape. Fano resonance is distinct in the absorption spectrum, and the spectral shape can be described by [27]:

$$\sigma(E) = D^2 \frac{(q+\Omega)^2}{l+\Omega^2}, \tag{9}$$

$$\Omega = 2 \times \frac{E - E_0}{\Gamma}, \tag{10}$$

$$D = 2 \times \sin\varphi, \tag{11}$$

where E and E_0 represent the absorption and resonant energy, respectively, Γ denotes the resonant width, and q is the Fano parameter, which equals $\cot\varphi$. The continuous phase shift φ depends on geometric and material parameters of the system and the incident waves [28].

For the Fano resonance of dielectric material, bright modes can be directly excited by external light sources, and dark modes cannot be directly coupled with the external light source [28]. Thus, the resonant quality value Q of the dark mode is much higher than that of the bright mode. Since the metasurface is a periodic structure, each dark mode is affected by multiple adjacent bright modes. The bright and dark modes are coupled in a way similar to electromagnetic induction. Since the coupling between the dark mode and adjacent bright mode is anti-phase, this Fano resonant structure has a symmetry-breaking property [29]. In all-dielectric metasurfaces based on Electromagnetically Induced Transparency (EIT), dark modes typically form arrays of perfectly symmetrical disks or rings, which cannot be generated by perpendicularly incident plane waves. It needs to be excited by the bright mode. Several reported resonant metasurfaces with high quality factors all rely on breaking the structure's symmetry to generate Fano resonances [30].

The volume-integrated stored electric energy ($\propto \iiint |E|^2 dV$) over the EO region (55 $\sim$ 75 GHz) shows a distinct peak at 65 GHz (Fig. 4), providing macrophysical proof of strong energy confinement.

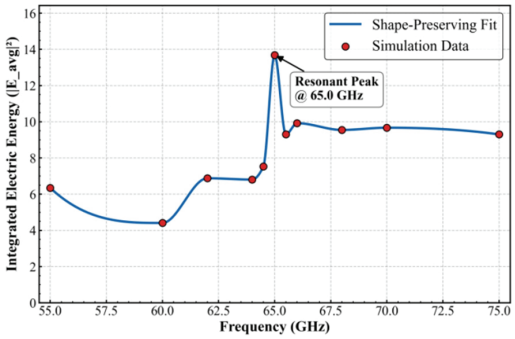

Fig. 4. Volume-integrated stored electric energy in EO region (55 $\sim$ 75 GHz).

B. All-dielectric metasurface configuration

Figure 5 (a) shows an overview of the designed all-dielectric metasurface. The units are periodically placed on a quartz substrate with a thickness of 1.118 mm and a dielectric constant of 3.75. The unit cell of the proposed metasurface is shown in Fig. 5 (b) and consists of two Si ($\varepsilon_r = 11.9$) elliptical cylinders with slightly different minor-axis lengths, and the major axes remain the same. The optimized physical dimensions of the unit cell structure by parameter analysis are as follows: major axis of the elliptical cylinder $L = 2.369$ mm, semi-minor axis lengths of the cylinder $b_1 = 0.3255$ mm and $b_2 = 0.5621$ mm, respectively, central distance between the two cylinders is $d = 1.37$ mm, period of the structure $P = 2.56$ mm, and thickness of the quartz substrate and silicon $h = 1.118$ mm.

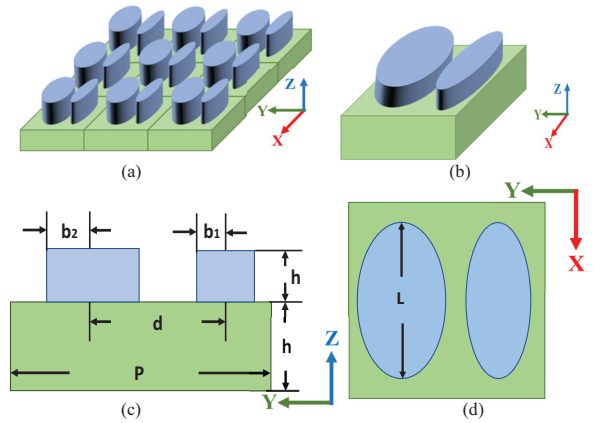

Fig. 5. (a) Overview of the whole structure. (b) Unit cell of the proposed metasurface. (c) Side view of the unit cell. (d) Top view of the unit cell.

To systematically summarize the critical design parameters of the metasurface and EO resonator for clarity and accessibility, key values are compiled in Table 1.

The metasurface shown in Fig. 6 is simulated using CST Microwave Studio. According to published literature, the unit-cell boundary condition is adopted to obtain results more quickly. To meet the system's actual application requirements, we design a finite-array metasurface using the following steps to ensure it exhibits resonance characteristics similar to those of the infinite-array metasurface.

Firstly, the proposed structure in Fig. 5 (b) is modeled as an infinite element, which is simulated using the Floquet incident mode to obtain the ideal resonant frequency. The unit cell boundary conditions are applied along the x- and y-axis, while the z-axis is set to an open (add space) boundary. The Floquet incident port is added at the top of the structure

Table 1: Key design parameters of the proposed metasurface receiver

Parameter	Value
Semi-minor axis of cylinder (b_1)	0.3255 mm
Semi-major axis of cylinder (b_2)	0.5621 mm
Length of elliptical cylinder (L)	2.369 mm
Center-to-center distance of cylinders (d)	1.3706 mm
Unit cell period (P)	2.56 mm
Substrate material	Quartz
Substrate thickness (h)	1.118 mm
Metasurface array configuration	3×3
Metasurface footprint	7.7×7.7 mm^2
EO resonator radius	0.34 mm
EO resonator material	$LiNbO_3$

and generates an incident TM wave. Five sharp Fano resonances excited by the asymmetry of the short axis at 55 GHz, 58 GHz, 64.8 GHz, 66.5 GHz, and 72 GHz can be observed by the transmission performance (black solid curve) in Fig. 6.

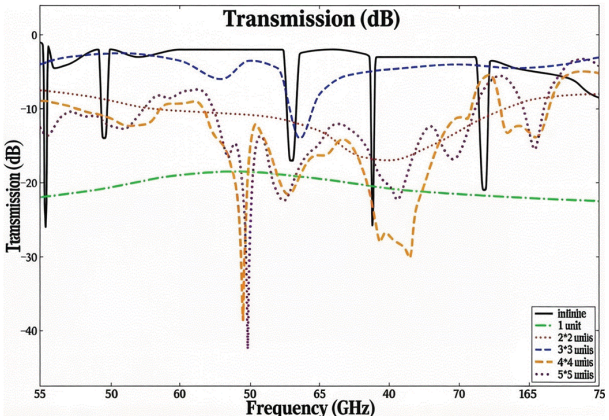

Fig. 6. Transmission spectra of different unit cell structures. Parameters of the metasurface are: $h_1 = 1.118$ mm, $h_2 = 1.118$ mm, $b_1 = 0.3255$ mm, $b_2 = 0.5621$ mm, $d = 1.37056$ mm, $L = 2.369$ mm, $P = 2.56$ mm.

Secondly, since the infinite-array metasurface is an ideal model and cannot be realized in practice, we carefully design a finite-array metasurface with resonance characteristics similar to those of the infinite-array metasurface. Open (add space) boundary conditions are used on the x, y, and z axes. The waveguide ports are added to the upper and lower surfaces of the structure. The structures with 1×1, 2×2, and 3×3 units are simulated, respectively. The three dotted lines in Fig. 6 indicate that the resonance is not obvious with only one or two units. However, the resonance at 65 GHz, similar to that of an infinite periodic structure, can be captured when the structure is designed as a 3×3 unit.

To further verify the rationality of the 3×3 array, we simulated 4×4 and 5×5 finite arrays. As shown in Fig. 6 and Table 1, the 4×4 and 5×5 arrays also exhibit resonant responses at 65 GHz, with S_{21} magnitudes of -36.67 dB and -47.26 dB, respectively. However, their resonant performance (e.g., bandwidth, field enhancement) shows no obvious improvement compared to the 3×3 array, while the footprint increases significantly ($4 \times 4 : 10.24 \times 10.24$ mm^2; $5 \times 5 : 12.8 \times 12.8$ mm^2). Considering the miniaturization requirements of 5G front-end systems, the 3×3 array is determined to be the optimal configuration, achieving a balance between resonant efficiency and compact size.

Finally, the 1 V/m incident plane wave is used to imitate the 65 GHz RF signal emitted by a horn antenna and illuminate the metasurface receiver. Since the structure in Fig. 5 is asymmetric along the x-axis, an electric or magnetic field component along the x-axis can excite the electric or magnetic field circulation mode, leading to an enhancement of the electric field.

Figure 7 shows the electric-field distribution corresponding to the Fano resonance at 65 GHz in the $x0z$ plane. The peak electric field exceeds 12 V/m. It is located between two elliptical cylinders and near the surface of the structure.

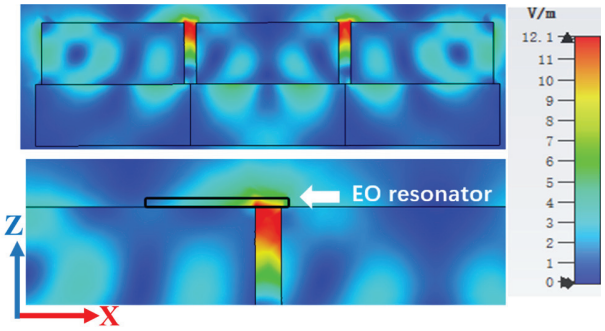

Fig. 7. Electric field distributions corresponding to the Fano resonance modes at 65 GHz in the $x0z$ plane.

A 3D functional bounding volume covering the EO interaction region was defined for volumetric statistics, yielding a peak enhancement of 12.2-fold, a volume-averaged enhancement of 3.7-fold, and a peak-to-average ratio of 3.3 (Fig. 8), validating a uniform field distribution for effective modulation.

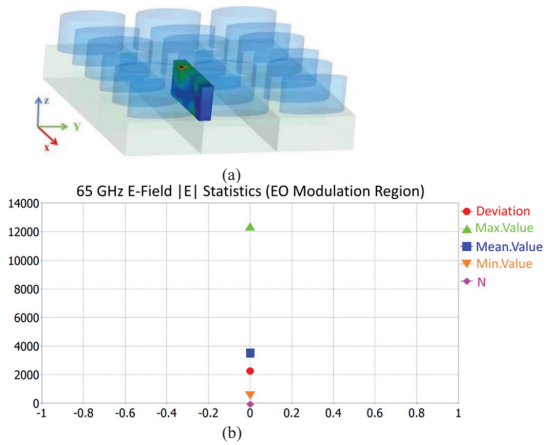

Fig. 8. Volumetric statistical characteristics of electric field in EO interaction region at 65 GHz.

C. Electro-optic resonator configuration

The free spectral range (FSR) of the resonator is defined as the interval between the adjacent resonance peaks of the EO resonator, which can be calculated as [21]:

$$FSR \approx \frac{c}{2\pi R_{EO} n_e}, \tag{12}$$

where R_{EO} is the radius of the EO resonator, $c = 3 \times 10^8$ m/s is the speed of light, and n_e is the refraction index of the EO resonator at the operation wavelength [21].

High-speed electro-optic modulation can be achieved only when the resonant frequency of the proposed dielectric metasurface matches FSR [23]. Therefore, the radius of the EO resonator is determined to be 0.34 mm for a resonant frequency of 65 GHz. As mentioned before, the electro-optic crystal is better located at the position where the maximum RF field occurs. However, for the convenience of processing, the $LiNbO_3$ electro-optic resonator is put at the top of the metasurface, which is close to the position of maximum electric field, as shown in Fig. 7. When the excitation electric field along the x-axis is 1 V/m, the field-enhancement factor $\beta = 12$. The field-enhancement factor of 12 ensures the receiver's high sensitivity, as further verified in section V.

IV. PARAMETRIC DISCUSSION

This section analyzes the effects of key parameters on transmission performance and the electric field distribution. Figure 9 shows the effect of the semi-minor axis of the cylinder b_2 when b_1 is 0.3255 mm. The b_2 is set to two values: b_1 and 60% of b1, respectively, to observe the impact of asymmetry. Two resonant peaks can be seen when b_2 is extremely different from b_1, shown as the solid line in Fig. 9. The first resonance point P1 is highly sensitive to b_2, which indicates that the symmetry of the structure has a great influence on the resonant position and quality Q. Traditional dark mode is usually an array of perfectly symmetrical disks or rings in the all-dielectric metasurface based on the EIT, the metasurface structure is usually an array of perfectly symmetrical disks with same b_1 and b_2. The resonance modes correspond to the circulation of electric and magnetic fields inside the cylinders. Only the dark mode can be excited by the resonance of the bright mode under the condition that the structure is asymmetric, which is an indirect excitation method. The structure's symmetry is broken to allow the mode to leak out, enabling direct coupling with the external light field.

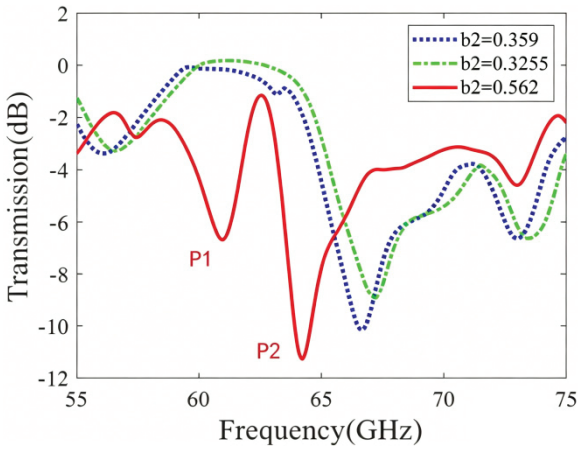

Fig. 9. Transmission spectra for different asymmetry parameters (semi-minor axis length b_2 of the elliptical cylinder). P1 and P2 are the resonant peaks.

Figure 10 indicates the influence of the height of two elliptical cylinders and the substrate on the resonance. It can be seen that the two resonant frequencies are sensitive to the height h. Both Fano resonant peaks shift to the right when h decreases from 1.1358 mm to 1.014 mm. In addition, the height of the two ellipticals affects not only the resonant position but also the resonant intensity. Results show that optimal quality Q can be obtained by increasing h. The slot formed by the two adjacent cylinders gives rise to the slot effect, further enhancing the near-field strength. The electric field loop inside the slot is squeezed and expanded along the z-axis as the height increases. Even though the resonant quality improves with increasing height, the maximum electric field is located inside the cylinders and is not suitable for placing the electro-optic resonator.

Figure 11 shows the transmission coefficient and the distribution of the electric field for different intervals between two elliptical cylinders. The interval d is

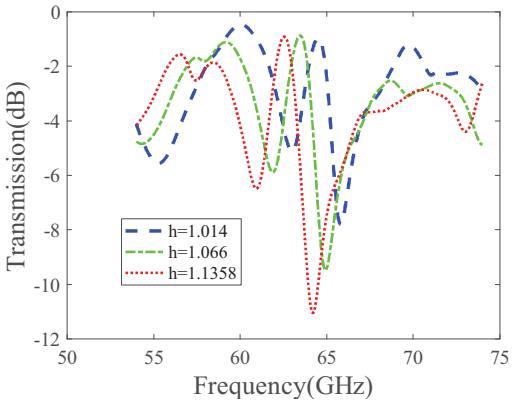

Fig. 10. Transmission spectra versus frequency for different heights of elliptical cylinders and substrates.

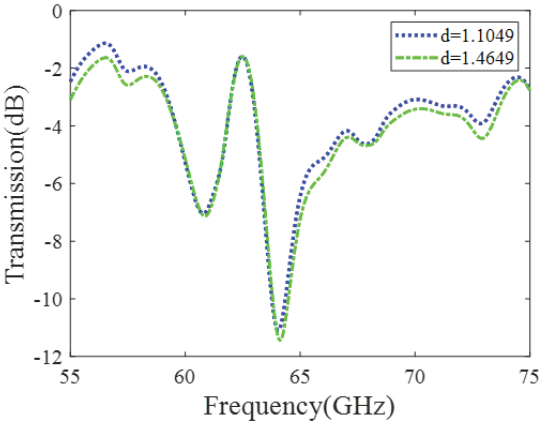

Fig. 11. Transmission spectra versus frequency for different center-to-center distances between two elliptical cylinders.

1.1049 mm and 1.4649 mm, respectively, due to the limitation of the periodic structure and the size of the elliptical cylinders. The spectra are nearly identical for $d = 1.1049$ mm and $d = 1.4649$ mm. This is because the sum of 1.1049 and 1.4649 mm is exactly the period of the structure $p = 2.5698$ mm. Since the unit cell is square and the metasurface is periodic, these two structures are identical. Since the sum of $d = 1.1049$ mm and 1.4649 mm equals the structural period $P = 2.5698$ mm, the two structures are equivalent in periodic metasurfaces, resulting in almost identical transmission spectra. This equivalence confirms that the metasurface's periodicity, rather than the absolute spacing between cylinders within a single unit cell, is the key factor governing transmission performance.

The influence of the major axis on resonance is shown in Fig. 12. As L increases from 2.002 mm to 2.34 mm, the resonant peak shifts to the left, and the quality factor Q decreases. This is because the loss of dielectric material increases with cylinder's surface area.

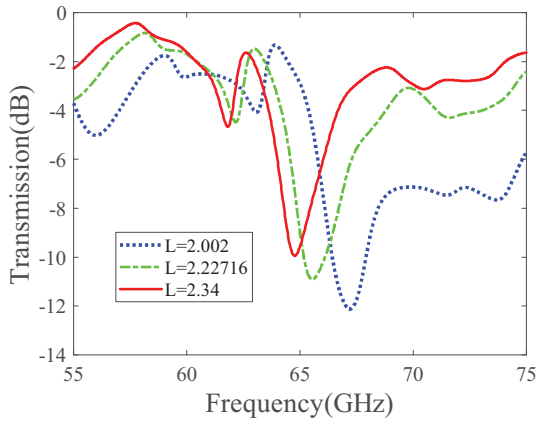

Fig. 12. Transmission spectra versus length of elliptical cylinder.

Fano resonance modes are highly sensitive to structural parameters. The optimal resonant effect and minimized structure can be achieved by increasing the asymmetry of the two elliptical cylinders.

V. SENSITIVITY ANALYSIS

The demodulated RF power after photodetection varies with the power incident on the metasurface, which is determined by the power supplied to the horn antenna. When the power fed into the horn antenna and the distance from the horn antenna to the dielectric metasurface are given, the power impinging on the metasurface antenna can be calculated by a standard radiation model of the horn antenna [23]. Therefore, the relationship between the RF power after photodetection and the power impinging on the dielectric metasurface can be approximately fitted to experimental points obtained by varying the power fed into the horn antenna. When the RF power after photodetection equals the observed noise floor, the corresponding free-space power impinging on the metasurface antenna, namely the measured receiver sensitivity, can be obtained by the previously fitted linear relationship.

The theoretically detected RF power P_{det} can be calculated [22]:

$$P_{det} = \frac{(mRP_0)^2}{2} R_D, \tag{13}$$

where m is the modulation depth of the light in the EO resonator, R is the photodetector responsivity, P_0 is the average optical power at the detector, and R_D is the detector resistance.

On the basis of Equations (1), (2), (3), (4), and (13), the relationship between the theoretically detected RF power P_{det} and the power impinging on the dielectric

metasurface P_{rf}^{inc} is linear:

$$P_{det} = \frac{(RP_0)^2 R_D}{2}\left(\frac{9Fn_e^3 r_{33}L}{2\sqrt{3}\pi\lambda}\right)^2 \frac{\beta^2\varepsilon_{MT}^2\eta}{\varepsilon_{LN}^2 A_e} P_{rf}^{inc}. \quad (14)$$

The theoretical receiver sensitivity is defined as the power impinging on the dielectric metasurface when the detected RF power equals the noise floor, and it can be calculated using (14). For estimating the receiver sensitivity of our proposed system in practice, a coefficient C of 0.01 is multiplied and, consequently, the estimated receiver sensitivity is:

$$P'_{det} = CP_{det} = C\frac{(RP_0)^2 R_D}{2}\left(\frac{9Fn_e^3 r_{33}L}{2\sqrt{3}\pi\lambda}\right)^2 \frac{\beta^2\varepsilon_{MT}^2\eta}{\varepsilon_{LN}^2 A_e} P_{rf}^{inc}. \quad (15)$$

Although the receiver sensitivity calculated by (15) is worse than that calculated by (14), this conservative estimation of performance considers the complexity of the whole receiver system and the influence of the actual environment, which provides a practical design margin in practical application and enables the proposed system to detect weaker incident power.

With fixed large/small resonator ratio $k = 0.85$, 1.00, 1.15, the effective aperture area $A_{eff} = \pi(r_{small}^2 + r_{big}^2)$ is 0.957767, 1.325630, 1.753145 arb. unit, and the EO volume-averaged field is 2.6, 3.7, 4.8 (Fig. 13), numerically validating the monotonic aperture-sensitivity scaling.

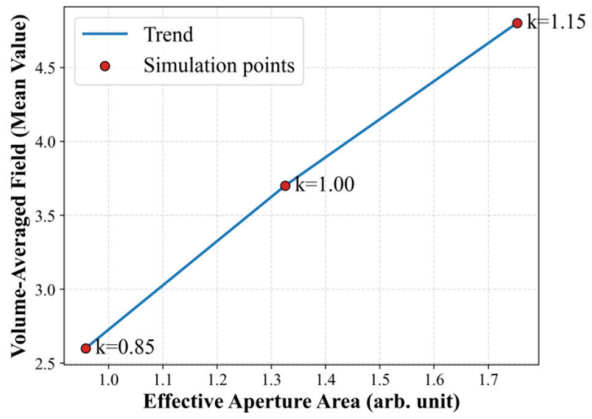

Fig. 13. EO volume-averaged field vs effective aperture area ($k = 0.85, 1.00, 1.15$).

It can be seen that the measured RF power after photodetection reported in other papers is about 20 dBm lower than the result calculated by (14), which verifies the rationality of setting the coefficient C to 0.01 [13–23].

To calculate the system's sensitivity, the effective permittivity ε_{MT} of the metasurface must be determined. The textbook method relies on the refractive index n and impedance z. Permittivity ε can be calculated by $\varepsilon = n/z$. Since the metasurface is composed of various dielectric materials and the refractive index is complex; a practical method is adopted to obtain the refractive index n and impedance z using the reflection coefficient (S_{11}) and transmission coefficient (S_{21}). The S parameters related to refractive index and impedance are given by [31–33]:

$$S_{11} = \frac{R_{01}(1 - e^{i2nk_0d})}{1 - {R_{01}}^2 e^{i2nk_0d}}, \quad (16)$$

$$S_{21} = \frac{(1 - R_{01})^2 e^{ink_0d}}{1 - {R_{01}}^2 e^{i2nk_0d}}, \quad (17)$$

where $R_{01} = (z-1)/(z+1)$, d means the thickness of the slab, and k_0 is the wave number of the incident wave in free space.

The refractive index n and impedance z can be calculated by:

$$z = \pm\sqrt{\frac{(1+S_{II})^2 - S_{21}^2}{(I - S_{I1})^2 - S_{21}^2}}, \quad (18)$$

$$n = \frac{1}{k_0 d} * \{Im[\ln(e^{ink_0d}) + 2m\pi] - i * Re[\ln(e^{ink_0d})]\}, \quad (19)$$

where m is an integer related to the branch index of n'.

The detection bandwidth is set to 10 kHz, and other parameters of the proposed receiver used in the sensitivity analysis are as follows: $FSR = 65$ GHz, $R_D = 50\ \Omega$, $\beta = 12$, $\varepsilon_{LN} = 35, \varepsilon_{MT} = 22, Q = 1.1 \times 10^6$, $R = 0.8$ A W^{-1}, $r_{33} = 30.8$ pm V^{-1}, $A_e = 5.929 \times 10^{-5}$ m^2, $n_e = 2.14, R_{EO} = 0.34$ mm, and $\lambda = 1.55$ μm. The linear relationship of the estimated receiver sensitivity and RF power after photodetection is shown in Fig. 14. According to detection of the free-space RF signal by the prototype receiver with and without the dielectric antenna, the observed noise floor generated by the RIN of the source laser is -96 dBm(-136 dBm$\cdot$Hz^{-1}) [13]. Therefore, the estimated receiver sensitivity of the proposed system, namely the incident RF power at which the RF power after photodetection equals the observed noise floor, is -52.1 dBm (-92.1 dBm$\cdot$Hz^{-1}).

From (12) and (15), it can be concluded that receiver sensitivity will deteriorate when the radius and circumference of the EO resonator decrease as the frequency of the incident signal increases. However, the proposed receiver still exhibits excellent performance, with sensitivity below -50 dBm at the millimeter-wave band.

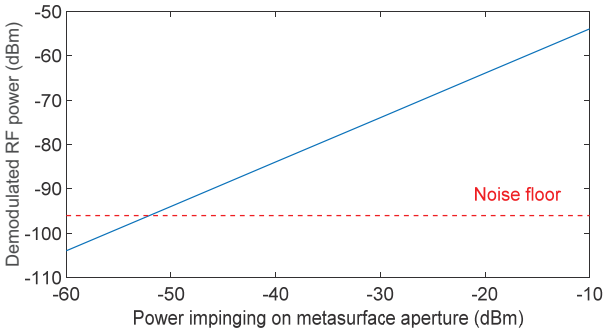

Fig. 14. Estimated receiver sensitivity of the proposed metasurface receiver.

VI. CONCLUSION

Metallic receiving antennas are inherently vulnerable to HEMP owing to their high electrical conductivity. All-dielectric antennas offer a promising alternative for radio front-end systems in HEMP-prone scenarios. In this paper, a new radio front-end receiver based on a metasurface operating in the millimeter-wave band is designed. By analyzing the influence of each structural parameter on Fano resonance, a metasurface antenna with a 3×3 cell array was proposed, where the electric field enhancement around the structure at 65 GHz is achieved. The electro-optic resonator disk was placed at the maximum electric field position, and the receiver sensitivity was improved to -52 dBm. With a compact size of 7.7×7.7 mm^2, the proposed metasurface enables 5G RF front-end systems to achieve HPMMW immunity. It should be noted that the current study is based on simulations and theoretical analyses, and the absence of experimental validation is a limitation that needs to be addressed. In future work, we plan to fabricate the prototype receiver and conduct experimental tests to verify its sensitivity, resonant characteristics, and HPMMW resistance, aiming to provide more solid support for practical applications.

ACKNOWLEDGMENT

This work was supported by the Beijing Municipal Natural Science Foundation (L233017), the National Key Laboratory of Intelligent Coal Mining and Strata Control (SKLIS202407), and the MIIT Key Laboratory of Radio Spectrum Monitoring Technology (SRTC-KFKT202501).

REFERENCES

[1] I. V. Mikhelson, S. Bakhtiari, T. W. Elmer, and A. V. Sahakian, "Remote sensing of heart rate and patterns of respiration on a stationary subject using 94-GHz millimeter-wave interferometry," *IEEE Transactions on Biomedical Engineering*, vol. 58, no. 6, pp. 1671–1677, 2011.

[2] R. Appleby and R. N. Anderton, "Millimeter-wave and submillimeter-wave imaging for security and surveillance," *Proceedings of the IEEE*, vol. 95, no. 8, pp. 1683–1690, 2007.

[3] S. Hantscher, M. Hagelen, S. Lang, H. Essen, M. Wieneke, W. Koch, and A. Tessmann, "Security assistant system combining millimeter wave radar sensors and chemical sensors," in *2011 IEEE International Symposium on Antennas and Propagation (APSURSI)*, IEEE, pp. 216–219, 2011.

[4] M. Field, T. Kimura, J. Atkinson, D. Gamzina, N. C. Luhmann, B. Stockwell, T. J. Grant, Z. Griffith, R. Borwick, C. Hillman, B. Brar, T. Reed, M. Rodwell, Y.-M. Shin, L. R. Barnett, A. Baig, B. Popovic, C. Domier, R. Barchfield, J. Zhao, J. A. Higgins, and Y. Goren, "Development of a 100-W 200-GHz high bandwidth millimeter-wave amplifier," *IEEE Transactions on Electron Devices*, vol. 65, no. 6, pp. 2122–2128, 2018.

[5] H. Yin, L. Zhang, J. Xie, K. Ronald, W. He, G. Shu, J. Zhao, Y. Yin, X. Chen, Y. Alfadhl, A. Cross, and A. Phelps, "Compact high-power millimeter wave sources driven by pseudospark-sourced electron beams," *IET Microwaves, Antennas & Propagation*, vol. 13, no. 11, pp. 1794–1798, 2019.

[6] J. Curtis, H. Zhou, and F. Aryanfar, "A fully integrated Ka-band front-end for 5G transceiver," in *2016 IEEE MTT-S International Microwave Symposium (IMS)*, IEEE, pp. 1–3, 2016.

[7] M. K. Hedayati, A. Abdipour, R. S. Shirazi, M. J. Ammann, M. John, C. Cetintepe, and R. B. Staszewski, "Challenges in on-chip antenna design and integration with RF receiver front-end circuitry in nanoscale CMOS for 5G communication systems," *IEEE Access*, vol. 7, pp. 43190–43204, 2019.

[8] W. Radasky, "Protection of commercial installations from the high-frequency electromagnetic threats of HEMP and IEMI using IEC standards," in *2010 Asia-Pacific International Symposium on Electromagnetic Compatibility*, IEEE, pp. 758–761, 2010.

[9] J.-H. Lee, J.-H. Cho, and E.-J. Kim, "Analysis of HEMP coupling signal for a coaxial cable with braided shields," *The Journal of Korean Institute of Electromagnetic Engineering and Science*, vol. 22, no. 8, pp. 790–796, 2011.

[10] E. Easton, K. Bryant, and W. Radasky, "Testing of a module for electrical substations to demonstrate HEMP and IEMI protection and GIC detection," in *2020 IEEE International Symposium on Electromagnetic Compatibility & Signal/Power Integrity (EMCSI)*, IEEE, pp. 442–447, 2020.

[11] R. Hao, X. Zhang, H. Gao, H. Wu, J. Cheng, and G.-P. Li, "A novel high-altitude electromagnetic pulse (HEMP) protection circuit for RF applications," *Microelectronics Journal*, vol. 84, pp. 1–8, 2019.

[12] H. Shin, N. Heo, J. Park, I. Seo, and J. Yoo, "All-dielectric structure development for electromagnetic wave shielding using a systematic design approach," *Applied Physics Letters*, vol. 110, no. 2, p. 021908, 2017.

[13] R. C. Hsu, A. Ayazi, B. Houshmand, and B. Jalali, "All-dielectric photonic-assisted radio front-end technology," *Nature Photonics*, vol. 1, no. 9, pp. 535–538, 2007.

[14] J. Nasir, M. H. Jamaluddin, M. Khalily, M. R. Kamarudin, and I. Ullah, "Design of a MIMO dielectric resonator antenna for 4G applications," *Wireless Personal Communications*, vol. 88, no. 3, pp. 525–536, 2016.

[15] H. Yang, Z. Guo, X. Li, Y. Zhang, X. Song, and S. Wang, "A compact circularly polarized crossed dipole antenna with wide bandwidth using split ring resonator and parasitic patches," *Applied Computational Electromagnetics Society (ACES) Journal*, vol. 39, no. 1, pp. 1–10, 2024.

[16] J.-X. Chen, H.-T. Xing, J.-M. Huang, M.-N. Wang, and Z.-H. Ma, "A three-dimensional compact propeller-shaped circularly polarized ceiling antenna," *Applied Computational Electromagnetics Society (ACES) Journal*, vol. 39, no. 1, pp. 1–10, 2024.

[17] D. L. Marks, O. Yurduseven, and D. R. Smith, "Cavity-backed meta-surface antennas and their application to frequency diversity imaging," *JOSA A*, vol. 34, no. 4, pp. 472–480, 2017.

[18] Z. Li, M.-H. Kim, C. Wang, Z. Han, S. Shrestha, A. C. Overvig, M. Lu, A. M. Agarwal, M. Loncar, D. R. Smith, and N. Yu, "Controlling propagation and coupling of waveguide modes using phase-gradient metasurfaces," *Nature Nanotechnology*, vol. 12, no. 7, p. 675, 2017.

[19] F. Lotti, A. Mirzaei, A. E. Miroshnichenko, and A. V. Zayats, "Nanoparticle-based metasurfaces for angular independent spectral filtering applications," *Journal of Applied Physics*, vol. 126, no. 21, p. 213101, 2019.

[20] L.-H. Gao, Q. Cheng, J. Yang, S.-J. Ma, J. Zhao, S. Liu, H.-B. Chen, Q. He, W.-X. Jiang, H.-F. Ma, Q.-Y. Wen, L.-J. Liang, B.-B. Jin, W.-W. Liu, L. Zhou, J.-Q. Yao, P.-H. Wu, and T.-J. Cui, "Broadband diffusion of terahertz waves by multi-bit coding metasurfaces," *Light: Science & Applications*, vol. 4, no. 9, pp. e324–e324, 2015.

[21] D. Cohen and A. Levi, "Microphotonic components for a millimeter-wave receiver," *Solid-State Electronics*, vol. 45, no. 3, pp. 495–505, 2001.

[22] B. Jalali, A. Ayazi, R. C. Hsu, A. Yick, W. H. Steier, and G. Betts, "A nonelectronic wireless receiver with immunity to damage by electromagnetic pulses," *Practical Applications of Microresonators in Optics and Photonics*, Boca Raton, FL: CRC Press, pp. 433–458, 2009.

[23] R. C. Hsu, A. Ayazi, B. Houshmand, and B. Jalali, "All-dielectric wireless receiver," in *2007 IEEE/MTT-S International Microwave Symposium*, IEEE, pp. 221–224, 2007.

[24] M. F. Limonov, M. V. Rybin, A. N. Poddubny, and Y. S. Kivshar, "Fano resonances in photonics," *Nature Photonics*, vol. 11, no. 9, pp. 543–554, 2017.

[25] W. Wang, L. Zheng, L. Xiong, J. Qi, and B. Li, "High Q-factor multiple Fano resonances for high-sensitivity sensing in all-dielectric metamaterials," *OSA Continuum*, vol. 2, no. 10, pp. 2818–2825, 2019.

[26] J. Leng, J. Peng, A. Jin, D. Cao, D. Liu, X. He, F. Lin, and F. Liu, "Investigation of terahertz high Q-factor of all-dielectric metamaterials," *Optics & Laser Technology*, vol. 146, p. 107570, 2022.

[27] H. Li, Y. Zhang, M. Qin, L. Wang, and Y. Chai, "High-quality Fano resonances and multispectral perfect absorption in mushroom-type dielectric metamaterials with a silver nanofilm," *EPL (Europhysics Letters)*, vol. 133, no. 6, p. 67002, 2021.

[28] Y. S. Joe, A. M. Satanin, and C. S. Kim, "Classical analogy of Fano resonances," *Physica Scripta*, vol. 74, no. 2, p. 259, 2006.

[29] Z. Chen, S. Zhang, Y. Chen, Y. Liu, P. Li, Z. Wang, X. Zhu, K. Bi, and H. Duan, "Double Fano resonances in hybrid disk/rod artificial plasmonic molecules based on dipole-quadrupole coupling," *Nanoscale*, vol. 12, no. 17, pp. 9776–9785, 2020.

[30] W. Wang, Y. Jin, W. Wang, B. Bonello, B. Djafari-Rouhani, and R. Fleury, "Robust Fano resonance in a topological mechanical beam," *Physical Review B*, vol. 101, no. 2, p. 024101, 2020.

[31] J. A. Kong, *Theory of Electromagnetic Waves*. New York: Wiley-Interscience, 1975.

[32] A. Nicolson and G. Ross, "Measurement of the intrinsic properties of materials by time-domain techniques," *IEEE Transactions on Instrumentation and Measurement*, vol. 19, no. 4, pp. 377–382, 1970.

[33] W.-C. Wang, *Electromagnetic Wave Theory*, ME557 Course Material, University of Washington, 1986.

Qiwei Liu received the master's degree in business administration from the Central University of Finance and Economics, Beijing, China, in 2019. He is currently working toward the Ph.D. degree in electronic engineering at the Beijing University of Posts and Telecommunications, Beijing, China. His research interests include electromagnetic compatibility, integrated circuits, ray tracing, and machine learning.

Dan Shi (Member, IEEE) received the Ph.D. degree in electronic engineering from the Beijing University of Posts & Telecommunications, Beijing, China, in 2008. She is a Professor with Beijing University of Posts & Telecommunications. Her interests include electromagnetic compatibility, electromagnetic environment, and electromagnetic computation.

Yanchi Liu received the bachelor's degree in e-commerce and law in 2023 from the Beijing University of Posts & Telecommunications, Beijing, China, where she is currently working toward the doctor's degree in electronic engineering. Her research interests include electromagnetic compatibility, intelligent design, and machine learning.

Jintao He received the bachelor's degree in communications engineering from Xi'an University of Posts & Telecommunications, Xi'an, China, in 2024. He is currently working toward the Doctor's degree in electronic engineering from the Beijing University of Posts & Telecommunications, Beijing, China. His research interests include electromagnetic compatibility and machine learning.

Hongbo Tao received the Ph.D. degree in electronic engineering from Beijing University of Posts and Telecommunications, Beijing, China, in 2003. Currently, he works at the National Radio Monitoring Center. His research interests include radio detection technology, electromagnetic compatibility analysis, and specialized radio measuring instruments.

Xiaoyong Liu received the bachelor's degree in radio technology and information system from Tsinghua University, Beijing, China, in 2002. He is currently working toward the doctoral degree in electronic science and technology with the Beijing University of Posts and Telecommunications, Beijing, China. His research interests include electromagnetic compatibility, testing and measurement, and radio frequency spectrum technology.

Zhonghua Xin received the master degree from Beijing Technology and Business University, Beijing, China, in 2002. She is a senior engineer with the Coal Science and Technology Research Institute. Her research interests include electromagnetic compatibility of Mining electrical equipment and wireless equipment, electromagnetic environment of underground coal mine.

Yuhao Jia received the bachelor's degree in information and computing science from Beihang University, Beijing, China, in 2020, and the master's degree in electronic information engineering from City University of Hong Kong, Hong Kong, China, in 2023. He is currently a researcher with China Coal Research Institute (CCRI), Beijing, China. His research interests include intelligent detection technology and electromagnetic compatibility.

Design of an Electronically Continuous Tunable Phased Array Antenna

Chang-Keng Lin[1], Ding-Bing Lin[1], and Chang-Ching Lin[2]

[1]Department of Electronic and Computer Engineering
National Taiwan University of Science and Technology, 43, Sec. 4, Keelung Rd., Taipei, Taiwan
d10902007@mail.ntust.edu.tw, dblin@mail.ntust.edu.tw

[2]Department of RF2
HONGBO Wireless Communication Technology Co. Ltd., 113, Sec. 1, Jiafeng 11th Rd., Hsinchu, Taiwan
timlin@hong-bo.com.tw

Abstract – In this paper, an electronically continuous tunable phased array antenna is proposed, which integrates a 1-port to 4-ports unequal power divider, four electronically continuous tunable phase shifters, and a 4×3 right hand circularly polarized patch array antenna. The unequal power divider is designed with a power ratio of 1:2.25:2.25:1 to achieve a side-lobe level suppression of 20 dB. The phase shifters provide electronically linear and continuously tunable phase control within $\pm 180^{\circ}$. Their phase difference can be easily controlled by adjusting the direct current voltage. The array antenna consists of 12 hexagon patches, providing right hand circular polarization within the operating bandwidth and achieving a high gain of 13.68 dB. Furthermore, the proposed phased array antenna is capable of continuously steering the main beam over a range of -50° to 55° in the Y-Z plane at 3 GHz. Finally, the measurement results show good agreement with the simulations, confirming that the proposed electronically continuous tunable phased array antenna exhibits excellent performance.

Index Terms – Circularly polarized, phased array antenna, right hand circular polarization (RHCP), side lobe level (SSL), unequal power divider.

I. INTRODUCTION

Phased array antennas have become indispensable in modern wireless communication and radar systems due to their capability of electronically steering beams without physically moving the antenna structure. Compared to conventional antennas, phased arrays provide advantages such as high gain, adaptive beam steering, and robustness against interference, making them suitable for applications ranging from satellite communications to 5G and beyond [1–3].

Beam steering in phased array antennas is typically achieved through phase shifters, which introduce relative phase differences between antenna elements [4]. Conventional phase shifters are often based on switched networks or digital step tuning, which limit their phase resolution and result in discrete steering angles [5]. A low-cost 4×4 Butler matrix-fed patch antenna array for millimeter wave applications was proposed in [6]. This phased array is suitable for 5G mmWave applications; however, its beam steering relies on a four-port Butler matrix network, which limits the steering capability to only four discrete angles. Such a restriction is insufficient for applications that require wide-angle or continuous beam steering. These limitations can degrade system performance, particularly in applications that require continuous beam tracking and fine angular resolution.

To overcome these challenges, researchers have investigated continuously tunable phase shifters using technologies such as ferroelectric materials [7]. However, these designs typically require high control voltages of up to 150 V, which may pose safety risks and increase the cost of associated equipment. Researchers have also proposed using RF microelectromechanical systems (MEMS) [8]. This approach enables smooth and precise control of the antenna main beam, providing enhanced flexibility and improved overall performance. However, the complex structure and fabrication process significantly increase cost. In [9], a similar MEMS-based phase shifter was designed for beam steering. However, it also required a relatively high control voltage of 125 V to produce phase differences, and the resulting beam steering range was limited to about 10°, which is insufficient for wide-angle applications.

In this work, we propose an electronically continuous tunable phased array antenna that integrates an unequal power divider, four continuously tunable phase shifters, and a 4×3 circularly polarized array antenna. The proposed design employs low control voltages for beam steering, ensuring safety and cost efficiency due to its simple structure. These features highlight its strong

Submitted On: January 20, 2026
Accepted On: May 06, 2026

https://doi.org/10.13052/2026.ACES.J.410405

potential for future microwave and wireless communication applications.

II. DESIGN, SIMULATION, AND MEASUREMENT OF THE 4 × 3 PHASED ARRAY ANTENNA

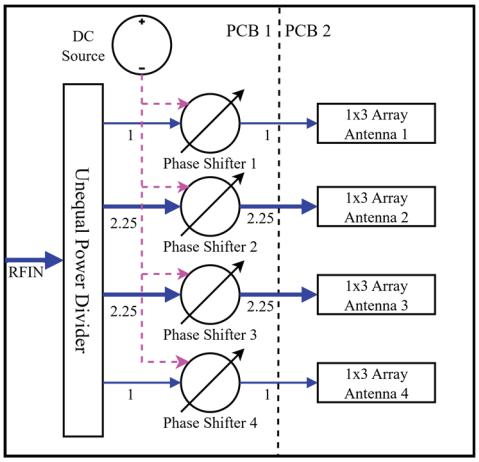

Fig. 1. Structure of the 4 × 3 phased array antenna.

Figure 1 shows the structure of the 4 × 3 phased array antenna, which consists of two PCBs. PCB1 is responsible for RF power distribution and phase control. When the RF signal enters the unequal power divider, it is divided into four output ports with a power ratio of 1:2.25:2.25:1, respectively. Each output port is connected to a phase shifter for RF phase control, where each phase shifter requires a DC bias voltage to achieve the desired phase adjustment. PCB2 is responsible for radiating the RF power, consisting of four sets of 1 × 3 array antennas that correspond to the four phase shifter outputs. The following sections present the design methodology at the operating frequency of 3 GHz, together with the simulation and measurement results of these components. The simulations were performed using Ansys HFSS and Keysight ADS, while the measurements were conducted with a Keysight P9371A VNA. All PCB simulations and fabrications were carried out on an FR4 substrate with a relative permittivity of 4.4, a loss tangent of 0.02, a thickness of 0.8 mm, and 1 oz copper cladding.

A. Design of the unequal power divider

In array antenna design, one important consideration is the suppression side lobe level [10, 11]. The most widely used approach is the optimum amplitude distribution, in which Dolph-Tschebyscheff distribution [12] is applied to calculate the input power of each array element. Since the proposed array antenna is a patch-type antenna with an inherent reflector, our experience shows that one of the standard Dolph-Tschebyscheff distribution equations must be modified accordingly, as shown in:

$$R = \frac{10^{\frac{SSL}{20}}}{\sqrt{2}}, \tag{1}$$

where R denotes the voltage ratio, SSL is expressed in dB, and $\sqrt{2}$ represents the modified term.

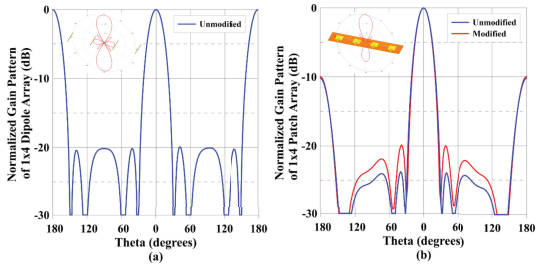

Fig. 2. Normalized gain pattern: (a) dipole array, (b) patch array.

Figure 2 shows the normalized gain patterns of a 1 × 4 dipole array antenna and a 1 × 4 patch array antenna. In Fig. 2 (a), the unmodified pattern of the 1 × 4 dipole array antenna is illustrated, where SSL is set to 20 dB with each port excited at a power ratio of 1:3:3:1. Figure 2 (b) compares the unmodified and modified patterns of the 1 × 4 patch array antenna. The modified design achieves the desired SSL of 20 dB with a power ratio of 1:2.25:2.25:1, while the unmodified pattern shows a significantly degraded SSL, reduced by approximately 8 dB. Because the reflected power is superimposed on the original directional power, a modified term of $\sqrt{2}$ must be included in (1) to modify the excitation power ratio, ensuring the designed SSL is accurate.

Based on the above analysis for achieving an SSL of 20 dB at patch array antenna, the output power ratio of the unequal power divider must be 1:2.25:2.25:1. This ratio is then applied to determine the impedance of each output port in the design of the unequal power divider. Furthermore, since each output port must maintain the same phase, a two-layer T-junction circuit structure is employed to design the unequal power divider, as shown in Fig. 3 (a).

The unequal power divider adopts a symmetric structure, so only half of the circuit needs to be designed and then mirrored to form the complete structure. The key design consideration is determining the impedances Z_1 and Z_2 to achieve the desired output power ratio of 2.25 : 1 at ports P3 and P2. Here, the calculation first employs the electric power formula in:

$$P = \frac{V^2}{Z}. \tag{2}$$

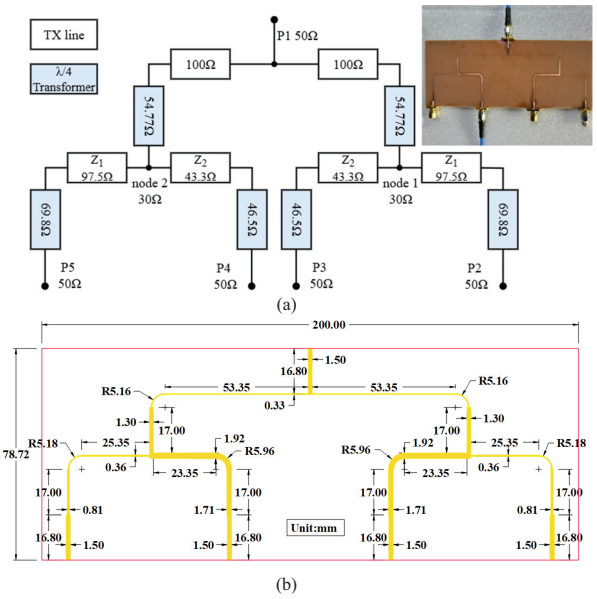

Fig. 3. (a) Circuit structure and prototype of the unequal power divider. (b) Detailed dimensions of the unequal power divider in mm.

Assume that node 1 has a voltage V and an impedance Z_n of 30Ω, while the other end of Z_1 and Z_2 are connected to ground. Accordingly, the power ratio of P2 and P1 can be formulated as:

$$\frac{V^2}{Z_2} : \frac{V^2}{Z_1} = 2.25 : 1. \tag{3}$$

Moreover, by applying the parallel resistance formula, another equation can be obtained as:

$$Z_n = \frac{Z_2 Z_1}{Z_2 + Z_1}. \tag{4}$$

Using (3) and (4), the impedances of Z_1 and Z_2 can be calculated. Z_n plays an important role in controlling Z_1; if Z_1 becomes too large, it may lead to manufacturing issues in the transmission line. All transmission line impedance values of the unequal power divider are designed and assigned as shown in Fig. 3 (a). Detailed dimensions are shown in Fig. 3 (b).

Figure 4 (a) presents the simulated and measured S-parameters of the unequal power divider. The measured S_{11} exhibits a frequency offset of 50 MHz, shifting the resonance to 2.95 GHz; however, this deviation does not significantly affect the overall performance.

Furthermore, S_{11} remains below -10 dB within the observed bandwidth of 600 MHz. Theoretically, the power ratio of 1:2.25:2.25:1 corresponds to -8.13 dB, -4.6 dB, -4.6 dB, and -8.13 dB, respectively. At 3 GHz, both the measured and simulated results are lower than the theoretical values. Specifically, S_{31} and

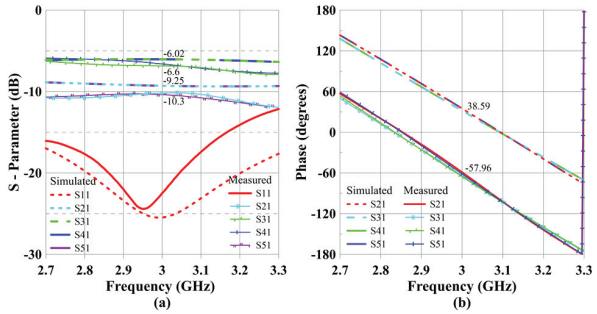

Fig. 4. Simulated and measured results of the unequal power divider: (a) S-parameters and (b) phase response.

S_{41} are approximately -6.6 dB and -6.02 dB, while S_{21} and S_{51} are approximately -10.3 dB and -9.25 dB. Although the measured results exhibit higher loss, the output power ratio still remains approximately 2.25:1. Figure 4 (b) shows the simulated and measured phase of the unequal power divider. The results remain in phase across the observed bandwidth; however, the measured data exhibits an additional phase delay of approximately 96° at 3 GHz, which is attributed to the SMA connectors and does not impact the overall performance. From the above discussion, the unequal power divider is successfully designed to meet the requirements, achieving an output power ratio of 1:2.25:2.25:1 with all ports in phase.

B. The phase shifter

The phase shifter is a critical component in phased array antennas as it directly controls the main beam steering. The phase shifter employed in this work has been designed and analyzed in detail with the results in [13]. It provides a linear, continuous, and tunable phase response within ±180°. Furthermore, the tunable phase response includes both leading and lagging phases, which can be easily controlled by adjusting the DC bias voltage.

Figure 5 presents the equivalent circuit model of the phase shifter, whose structure enables the above description properties. In addition, the proposed phase shifter includes a design guideline that allows arbitrary design of its operating frequency and phase shifting bandwidth (PSBW). These phase shifters are designed for an operating frequency of 3 GHz with a PSBW of 400 MHz in this paper.

Figure 6 shows the prototype of PCB1, which includes the unequal power divider, four phase shifters, and four DC sources. The DC source (lumped components) consists of a 10 kΩ variable resistor in series with a 2 kΩ resistor to form a voltage divider circuit, which outputs a DC bias voltage to control the phase of the phase shifter. The measurement results of the prototype

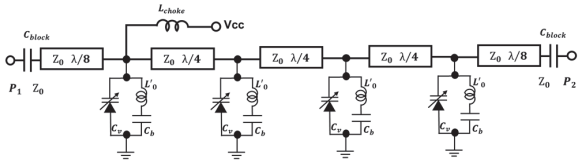

Fig. 5. Equivalent circuit model of the phase shifter.

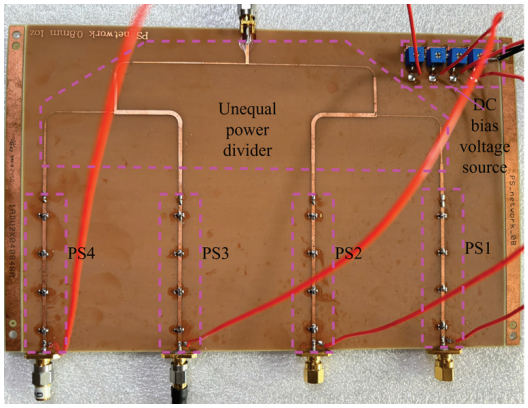

Fig. 6. PCB1 prototype including the unequal power divider, four phase shifters, and four DC sources.

are presented in Fig. 7. Figure 7 (a) shows a resonance at 3 GHz with a minimum reflection coefficient of −20 dB, remaining below −6 dB within the observed bandwidth. It also exhibits two sets of transmission coefficients at approximately −14 dB and −20 dB, respectively. These losses are consistent with expectations, as the additional transmission loss introduced by the phase shifter is approximately −8 dB, compared to −6 dB and −10 dB for the case with only the power divider.

Figure 7 (b) shows the phase responses of the four output ports of the PCB1 prototype. At 3 GHz, the responses are clearly in phase, corresponding to 0°. Furthermore, the responses exhibit an approximately linear phase variation within ±180° over the frequency range from 2.8 GHz to 3.16 GHz. This frequency range is important, as it also represents the tunable phase range of each phase shifter.

Figure 8 shows the measured phase response of each phase shifter with respect to the applied DC bias voltage at 3 GHz. All curves exhibit a similar trend, where adjusting the DC bias voltage from 3.5 V to 12 V results in a corresponding phase shift from −180° to 180°.

The curve of PS4 reaches a 180° phase shift at a bias voltage of 8.5 V, indicating that varactor diodes in this phase shifter exhibit slightly different characteristics as shown in Fig. 5. It should be noted that because the DC bias voltage is continuously adjustable, the phase shift also changes continuously. Consequently, the main beam steering of the phased array antenna is naturally continuous as well.

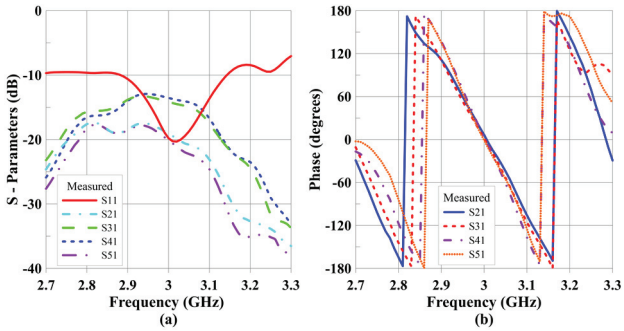

Fig. 7. Measurement results of the PCB1 prototype: (a) S-parameters and (b) phase response.

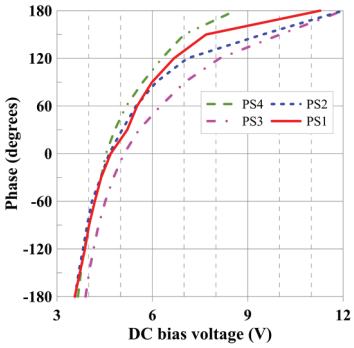

Fig. 8. Measured phase response of each phase shifter corresponding to the control voltage.

C. Design of the 4 × 3 array antenna

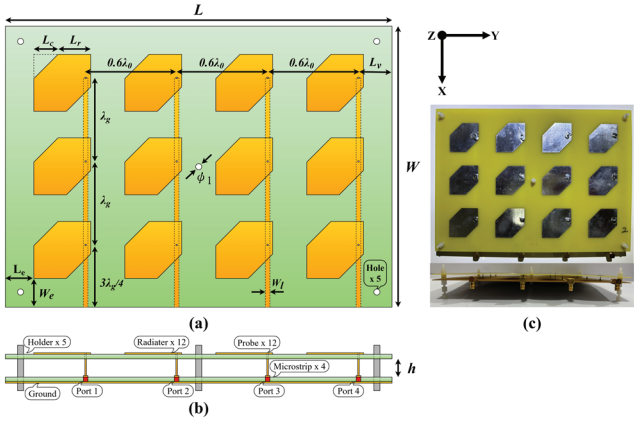

Fig. 9. Structure of the 4 × 3 array antenna: (a) top view, (b) front view, and (c) prototype.

Figure 9 illustrates the structure and prototype of the 4 × 3 array antenna, comprising two FR4 PCBs. The upper PCB consists of 12 hexagon radiators arranged in a 4 × 3 configuration, with an element spacing of $0.6\lambda_0$ along the Y-axis and λ_g along the X-axis. The lower PCB consists of four feeding lines and a ground

Table 1: Design parameters of the array antenna

L	L_c	L_r	L_e	L_v	h	Unit
255	16	21.5	18.75	22.5	6	
W	W_e	W_l	λ_0	λ_g	ϕ_1	mm
185	18.75	3	100	55	4	

plane. The two PCBs are assembled using five holders with a separation distance of h. The distance h is designed to enhance the radiation efficiency of the patch antenna [14]. The 12 radiators are connected to their corresponding feeding lines through 12 copper wires. Each copper wire has a diameter of 1 mm. Table 1 lists all design parameters of the array antenna.

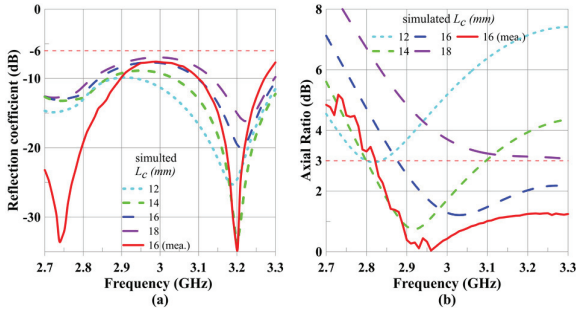

Fig. 10. Simulated and measured results of the 4×3 array antenna: (a) reflection coefficient and (b) axial ratio.

Figure 10 (a) shows the simulated and measured reflection coefficients of a single port of the array antenna, along with the results obtained for different corner-cut lengths L_C of the rectangular patch. The corner-cut L_c is introduced to improve the circular polarization radiation characteristics of the array antenna. The axial ratio (AR) is a key indicator for evaluating whether an antenna exhibits circular polarization, with a threshold of 3 dB commonly used to assess circular polarization performance. However, a L_C of 16 mm was selected, as it provides the best AR bandwidth, as shown in Fig. 10 (b), with only a slight degradation in the reflection coefficient. Therefore, in this case, the reflection coefficient and AR exhibit a trade-off. To achieve a better AR, we slightly sacrifice the reflection coefficient, which degrades to -8 dB at 3 GHz. Figure 10 illustrates the measured results (red lines) are better overall than the simulated results. In general, a reflection coefficient below -6 dB is considered acceptable in industry standards. If this criterion is adopted, the bandwidth of the antenna array exceeds 600 MHz, as shown in Fig. 10 (a).

Figure 11 shows the current distribution of the RHCP at 3 GHz, with four identical current directions at $0°, 90°, 180°$, and $270°$, respectively. In addition, the

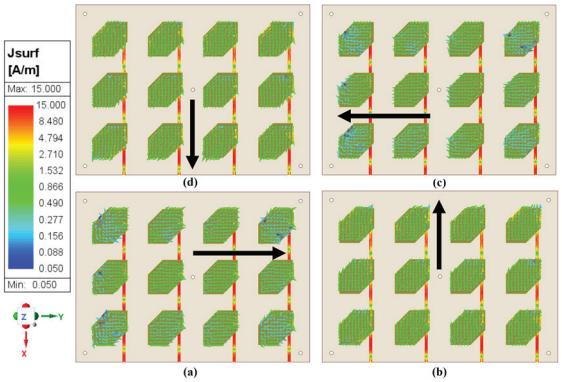

Fig. 11. Current distribution of the RHCP at 3 GHz: (a) $0°$, (b) $90°$, (c) $180°$, (d) $270°$.

feeding spacing of λ_g ensures that the currents of all 12 radiators and feeding lines remain in phase. A uniform current distribution is observed on each radiator along the four directions.

The isolation is an important evaluation index for reducing interference in array antennas. In general, the isolation should be lower than -20 dB, which indicates that the mutual coupling power between elements is less than 1/100. As shown in Fig. 12, both the simulated and measured isolation values are all below -23 dB, meaning that the coupling power between each port of the 4×3 array antenna is less than $1/200$, thereby achieving good isolation performance.

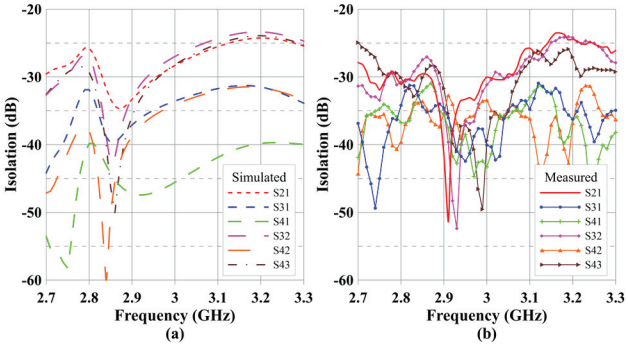

Fig. 12. Isolation of the 4×3 array antenna: (a) simulated and (b) measured.

Figure 13 shows a 3D gain pattern and measurement setup of the 4×3 array antenna with an unequal power divider. The 3D gain pattern demonstrates a maximum gain of 15.11 dB, with suppressed side-lobes in the Y-Z plane, when the four ports are excited with a power ratio of 1:2.25:2.25:1.

Figure 14 compares the simulated and measured 2D gain patterns in the X-Z and Y-Z planes. Both results exhibit similar trends; however, the angular resolution differs, being $5°$ in simulation and $15°$ in measurement.

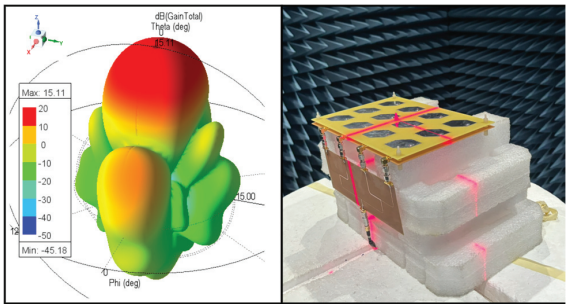

Fig. 13. 3D gain pattern and measurement setup of the 4×3 array antenna with an unequal power divider.

The 15° resolution in the measurements also leads to a more symmetric radiation pattern. The measured maximum gain is 13.68 dB, which is lower than the simulated value due to approximately 1.43 dB of insertion loss introduced by the five SMA connectors. Moreover, the measured side-lobe levels are below -20 dB on both sides, confirming the effective side-lobe suppression achieved by the unequal power divider, as shown in Fig. 14 (b). In addition, the measured half-power beamwidth is approximately 20°, which is consistent with the simulated result.

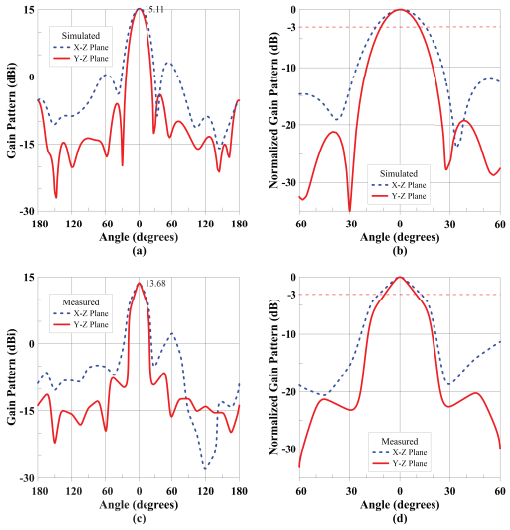

Fig. 14. Comparison of 2D gain patterns in the X-Z and Y-Z planes: (a,b) simulated and (c,d) measured.

III. PHASED ARRAY ANTENNA

Figure 15 shows the measurement setup of the 4×3 phased array antenna, where PCB1 and PCB2 are connected using four L-shaped SMA connectors. The measurement setup employs the ETS-Lindgren's AMS 8923-14-G Antenna Measurement System.

Figure 16 shows the measured and simulated gain patterns of the 4×3 phased array antenna at different

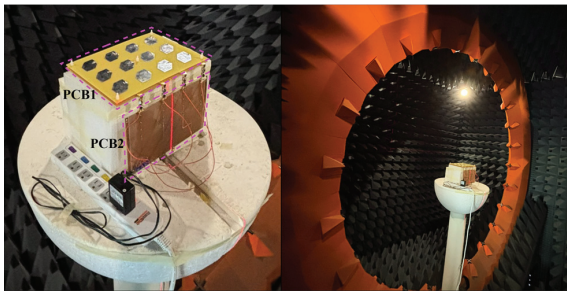

Fig. 15. Measurement setup of the 4×3 phased array antenna.

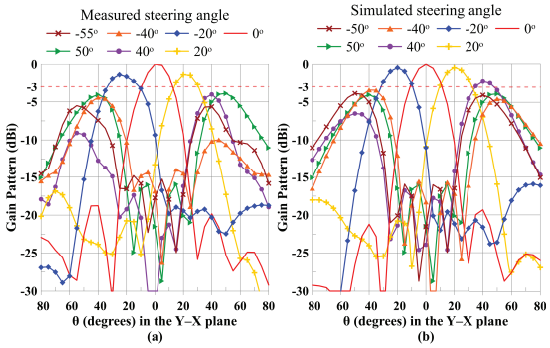

Fig. 16. (a) Measured and (b) simulated steering angle of the 4×3 phased array antenna.

steering angles. Since the measured gain was compensated for the 10 dB loss introduced by the phase shifters, the patterns are nearly identical in shape. Even after compensation, the measured gain is still about 3 dB lower than the simulated gain, which can be attributed to losses from the connectors and substrates. Figure 16 (b) shows the simulated maximum steering angle from $-50°$ to $50°$ in the Y-Z plane. This indicates that when the main beam is steered to its maximum angle, a secondary main beam appears at the opposite angle. A similar situation can also be observed in the measurements, where a secondary main beam appears, though smaller than the primary beam. The measured steering angle ranges from $-55°$ to $50°$ in the Y-Z plane, which is 5° wider than the simulated result. This discrepancy may be attributed to measurement errors according to:

$$\Psi = \beta \mathrm{d} \sin\theta + \delta, \tag{5}$$

where $\Psi = 0, \beta$ is the wave number, d is the element spacing, θ is the azimuth angle, δ is the phase difference. In other words, the azimuth angle θ corresponding to the required phase difference can be easily calculated. Furthermore, each phase difference can be mapped to a control voltage for each phase shifter, as illustrated in Fig. 8. Table 2 summarizes the steering angles of the 4×3 phased array antenna along with the corresponding

Table 2: Steering angle of the 4×3 phased array antenna corresponds to the phase difference and control voltage of each phase shifter

Steering	$\mathbf{-55^\circ}$		$\mathbf{-40^\circ}$		$\mathbf{-20^\circ}$		$\mathbf{0^\circ}$		$\mathbf{20^\circ}$		$\mathbf{40^\circ}$		$\mathbf{50^\circ}$	
angle	$\boldsymbol{\delta}$	**V**	$\boldsymbol{\delta}$	**V**	$\boldsymbol{\delta}$	**V**	$\boldsymbol{\delta}$	**V**	$\boldsymbol{\delta}$	**V**	$\boldsymbol{\delta}$	**V**	$\boldsymbol{\delta}$	**V**
PS1	-180°	3.5	-150°	3.7	-74°	4	0°	4.7	148°	7	150°	7.5	0°	4.7
PS2	0°	4.6	0°	4.6	0°	4.6	0°	4.6	74°	5.6	0°	4.6	180°	3.4
PS3	180°	12	150°	10	74°	6.5	0°	5.1	0°	5.1	-150°	3.7	0°	5.1
PS4	360° (0°)	4.5	300° (-60°)	4.2	148°	7	0°	4.5	-74°	4	-300° (60°)	5.1	-180°	3.5

Table 3: Comparison of the proposed 4×3 phased array antenna with other designs

Ref.	**Technology**	**Control Voltage**	**Steering Type**	**Steering Range**	**Complexity/Cost**
[6]	Passive 4×4 Butler matrix	N/A	Discrete	4 fixed angles	Low
[7]	Ferroelectric	$0 \sim 150$ V	Continuous	$-50^\circ \sim 50^\circ$	Medium
[9]	RF MEMS	$0 \sim 125$ V	Continuous	$0^\circ \sim 10^\circ$	High
This Work	Varactor based phase shifters	$3.5 - 12$ V	Continuous	$-55^\circ \sim 50^\circ$	Low

phase differences and control voltages. It is worth noting from Table 2 that the phase differences are relative, incorporating both leading and lagging phases. In contrast, most other phase shifters employ only lagging phases and achieve phase shifting in discrete steps. Furthermore, since the control voltage is continuously adjustable, the corresponding phase variation is also continuous. These two features represent the major contributions of the proposed electronically continuous tunable phased array antenna.

IV. COMPARISON WITH OTHER DESIGNS

Table 3 compares the proposed 4×3 phased array antenna with other reported phased array systems. The Butler matrix-fed design in [6] is low cost and suitable for mmWave 5G applications, but its discrete phase states restrict beam steering to only four directions.

Ferroelectric-based phase shifters [7] allow continuous tuning, but the high control voltage ($\sim$150 V) raises safety and integration concerns. MEMS-based phase shifters [9] provide precise phase control; however, their complex fabrication increases cost, and the achieved steering angle is typically narrow $\sim 10^\circ$.

In contrast, the proposed 4×3 phased array antenna achieves wide-angle steering ($-55^\circ \sim 50^\circ$), robust circular polarization, and continuous tunability with a safe and low control voltage ($3.5 - 12$ V). Additionally, its structure is relatively simple, leading to lower cost and higher manufacturability. These advantages make it an attractive candidate for practical microwave and wireless communication applications.

V. CONCLUSION

In this work, an electronically continuous tunable phased array antenna operating at 3 GHz has been proposed and demonstrated. The design integrates an unequal power divider, four electronically continuous tunable phase shifters, and a 4×3 RHCP patch array antenna. The unequal power divider achieves the optimized power ratio of 1:2.25:2.25:1, effectively suppressing the SSL by 20 dB.

The proposed phase shifter provides linear, continuous, and wide-range phase control within $\pm 180^\circ$, which can be easily adjusted via a DC bias voltage. Unlike conventional phase shifters that typically offer only lagging phase (phase delay), the proposed design enables both leading and lagging phases. This capability significantly enhances beam-steering flexibility. Consequently, a wide steering range from -55° to 50° is achieved without the need for complex phase-wrapping algorithms commonly required in conventional designs.

The array antenna, consisting of 12 hexagon shaped patches, achieves RHCP across the operating bandwidth, a high gain of 13.68 dB, and excellent isolation performance with all port coupling below -23 dB. Beam steering from -55° to 50° in the Y-Z plane has been experimentally verified, with measured results showing good agreement with simulations. Overall, the proposed phased array antenna demonstrates high gain, robust RHCP, low SSL, low isolation, wide-angle beam steering, and continuous phase control, which are key features required for future microwave and wireless communication applications.

ACKNOWLEDGMENT

This work was supported by the National Science and Technology Council, Taiwan, under Contract NSTC 113-2221-E-011-110-MY2. The authors would like to thank HONGBO Wireless Communication Technology

Co. Ltd. for providing access to the radio wave anechoic chamber for the phased array antenna measurements.

REFERENCES

[1] T. Chaloun, L. Boccia, E. Arnieri, M. Fischer, V. Valenta, and N. J. G. Fonseca, "Electronically steerable antennas for future heterogeneous communication networks: Review and perspectives," *IEEE Journal of Microwaves*, vol. 2, no. 4, pp. 545–581, 2022.

[2] H. Lee, S. Kim, and J. Choi, "A 28 GHz 5G phased array antenna with air-hole slots for beam width enhancement," *Applied Sciences*, vol. 9, no. 20, 2019.

[3] O. Barrou, A. El Amri, and A. Reha, "Microstrip patch antenna array and its applications: A survey," *IOSR Journal of Electrical and Electronics Engineering*, vol. 15, no. 1, pp. 26–38, 2020.

[4] M. Li, S.-L. Chen, Y. Liu, and Y. J. Guo, "Wide-angle beam scanning phased array antennas: A review," *IEEE Open Journal of Antennas and Propagation*, vol. 4, pp. 695–712, 2023.

[5] M. Kebe, M. C. E. Yagoub, and R. E. Amaya, "A survey of phase shifters for microwave phased array systems," *International Journal of Circuit Theory and Applications*, vol. 53, no. 6, pp. 3719–3739, 2024.

[6] C. K. Lin, D. B. Lin, and M. L. Chang, "A low-cost 4×4 Butler matrix-fed patch antenna array for millimeter wave applications," *Microwave and Optical Technology Letters*, vol. 67, no. 1, 2025.

[7] M. Sazegar, Y. Zheng, H. Maune, C. Damm, X. Zhou, and J. Binder, "Low-cost phased-array antenna using compact tunable phase shifters based on ferroelectric ceramics," *IEEE Trans. Microw. Theory Techn.*, vol. 59, no. 5, pp. 1265–1273, 2011.

[8] E. Liu, G. Li, Y. Zhao, and Y. Zhao, "Design of an X-band 4-channel circulator phase shifter based on silicon MEMS technology," in *2025 5th International Conference on Electronics, Circuits and Information Engineering (ECIE)*, pp. 610–615, 2025.

[9] P. Goel and K. Vinoy, "A low-cost phased array antenna integrated with phase shifters cofabricated on the laminate," *Progress in Electromagnetics Research B*, vol. 30, pp. 255–277, 2011.

[10] M. Arun and M. R. Ebenezar Jebarani, "Design of phased array antenna with low side lobes," *Materials Today: Proceedings*, vol. 80, pp. 2150–2154, 2023.

[11] F. Y. Zulkifli, T. Hidayat, and E. T. Rahardjo, "Side-lobe level suppression using unequal four-way power divider for proximity coupled microstrip antenna," in *2013 Asia-Pacific Microwave Conference Proceedings (APMC)*, pp. 1166–1168, 2013.

[12] C. A. Balanis, *Antenna Theory: Analysis and Design*. Hoboken, NJ: John Wiley & Sons, 2016.

[13] C.-K. Lin and D.-B. Lin, "Design and analysis of an electronically continuous tunable phase shifter for phased array antennas," *IEICE Transactions on Fundamentals of Electronics, Communications and Computer Sciences*, pp. 873–883, 2025.

[14] D.-B. Lin, C.-K. Yu, C.-K. Lin, and Y.-H. Lee, "Dual band rectenna with one rectifier," in *2017 International Symposium on Electronics and Smart Devices (ISESD)*, pp. 268–272, 2017.

Chang-Keng Lin was born in New Taipei City, Taiwan. He received his M.S. degree in Electronic Engineering from the National Taipei University of Technology, Taipei, in 2016. He received his Ph.D. degree in the Department of Electronic and Computer Engineering at the National Taiwan University of Science and Technology, Taipei, in 2026. His research interests include phase shifters, phased-array antennas, microwave components, antennas, wireless power transfer, RF circuits, and electronic circuit integration.

Ding-Bing Lin (S'89–M'93–SM'14) received the M.S. and Ph.D. degrees in electrical engineering from National Taiwan University, Taipei, Taiwan, in 1989 and 1993, respectively. From August 1993 to July 2016, Lin was on the faculty of the Electronic Engineering Department, National Taipei University of Technology, Taipei, where he was an Associate Professor, a Professor, and a Distinguished Professor in 1993, 2005, and 2014 respectively. Since August 2016, he had been with National Taiwan University of Science and Technology, Taipei, where he is currently a Professor of the Electronic and Computer Engineering Department. His research interests include wireless communication, antennas, high-speed digital transmission, and microwave engineering. From 2015 to 2018, he served as the Taipei Chapter Chair, IEEE EMC society. Since 2022, he serves as Taipei Chapter Chair, IEEE AP Society. Since 2019, he serves as Associate Editor of *IEEE Transactions of Electromagnetic Compatibility* and since 2014 as Editorial Board member of *International Journal of Antennas and Propagation*. He has published more than 250 papers in international journals and conferences. Lin was the recipient of the Annual Research Outstanding Award of the College of Electrical Engineering and Computer Science in 2004, 2006, and 2008. After he had received these three awards, the College of Electrical Engineering and Computer Science

awarded him the College Research Outstanding Award to highlight his research achievements. He was also the recipient of the Taipei Tech Annual Outstanding Research Award in 2008. Lin is the recipient of the Annual Research Outstanding Award of the National Taiwan University of Science and Technology in 2024.

Chang-Ching Lin was born in Yun Lin County, Taiwan. He received his M.S degree in Electrical and Communication Engineering from Yuan Ze University in 2010. From 2004 to 2008, he worked at Amphenol Antenna Taiwan Center. From 2008 to 2017, he worked at Foxconn FIT Antenna Team. Since 2017, he has been working at Hong-Bo Wireless Technology, mainly focusing on the design of commercial embedded antennas.

A Substrate-Loaded Gain-Enhanced Vivaldi Antenna Design for the SolidState High-Power Microwave Module

Zichong Chen, Fangsheng Cai, Peng Bai, Taijing Shi, Xiaojun Mao, and Yun Jiang*

Department of Microwave Research
Hunan Vanguard Group Co. Ltd., Changsha 410137, China
czc0720@hnu.edu.cn, cfsnuaa@163.com, 2641630277@qq.com,
shitaijing@yeah.net, 804367142@qq.com, 867581306@qq.com
*Corresponding Author

Abstract **–** This paper presents an evolutionary design process, fabrication, and verification of a substrateloaded Vivaldi antenna (VA) design for the pulse-type high-power microwave (HPM) solid-state T/R module. The antenna design utilizes a substrate with high permittivity to improve its power handling capacity (PHC), a snowflake-like metasurface (SFL-MS) lens on the front of the VA to enhance the directivity and impedance characteristics in the middle and high frequency bands, and rectangular slits on the radiating brims of the VA for further broadening its bandwidth and realized gain at low frequencies. After HPM measurement, these functional methods are proven to be effective for jointly contributing to optimizing antenna performances. The proposed prototype shows an operating band of 2.28–6.54 GHz (voltage standing wave ratio [VSWR] < 2) and the PHC values are over 8000 W in this band. The measured realized gain and the maximum gain enhancement can reach 6.56–8.15 dBi and 5.96 dBi. The measured results are reasonable and agree well with simulations.

Index Terms **–** High-power microwave, metasurface lens, realize gain enhancement, Vivaldi antenna.

I. INTRODUCTION

High-power microwave (HPM) technology plays an important role in terms of the electronic component and system, its protective technology, weapon and equipment, and biological effect. Different from the vacuum-state HPM source, the solid-state HPM output module, made of gallium nitride (GaN) material, has advantages of light weight, parameterized flexibility, and using a coaxial port to feed instead of a waveguide port. Currently, the maximum stable power output from one port on the solid-state HPM module is not more than 8000 W in the S- and C-band in practical engineering uses, so that hundreds of such solid-state HPM modules can realize an equivalent effect like the vacuum-state HPM system. As the element of the phased array, they are tested for high directivity in a wide band in order to realize wide-beam scanning.

For the virtues of stable realized gain in broadband and compact structures, efforts have been made into Vivaldi antennas (VAs) since it was proposed in the 1970s [1, 2]. However, VA loaded on the common substrate ($\varepsilon_r = 2 - 5$) is seldom adopted in the HPM system for its low power handling capacity (PHC), usually 1000–3000 W in the air. One way to improve the PHC of the VA is making the antenna all-metallic. Researchers devote energy into all-metallic VA elements [3, 4] and arrays [5–8]. Even though the allmetal antenna satisfies the PHC demand of the HPM system, it is obviously overweight compared to the substrate-loaded antenna, especially when arranging arrays, which will no doubt restrict the flexibility and mobility of the solid-state HPM system on moving platforms.

Another solution is to adopt VAs on the dielectric substrate with high permittivity, which evidently decreases the value of maximum E-field distribution in the operating band [9–11], and successfully enhances the PHC of the antenna. The VA on the high permittivity substrate will introduce a high radiation loss, however, which will lead to lowering the radiation efficiency and directivity of the VA. It is an important scientific research direction to improve the realized gain and directivity of the VA on the substrate.

A single-layered array consisting of two fourelement VA is fabricated and verified for gain enhancement in the microwave band [12]. Adding metasurface (MS) to antennas is considered effective for gain enhancement in the VA design. Designing an MS element with various shapes and arrangements on the front of the substrate between two radiating brims, an improving gain can be obtained in the IoT/WLAN band [13], 5G

Submitted On: July 18, 2025
Accepted On: April 08, 2026

https://doi.org/10.13052/2026.ACES.J.410406

mmWave application [14, 15], frequency point [16], and UWB [17–20] in the microwave band. Based on the MS design, introducing novel structures to the VA can further help gain enhancement. Expanding the front part of the substrate to rectangle [21], ellipse [22, 23] or cone [24] can at most increase 4.8 dBi, 5.5 dBi, 2 dBi, and 6.35 dBi, respectively. Besides, elliptical director [25, 26], spoof surface plasmon polariton structure [27], and cascaded cavity-based substrate cutout technique [28] are also greatly helpful for gain-enhancement of the VA.

In this paper, we present the design, iteration, fabrication, and experimental verification of an HPM VA using a PCB substrate with high permittivity. The proposed antenna design can cover a voltage standing wave ratio (VSWR) below 2 in a band of 2.28–6.54 GHz, where PHC values are over 8000 W and a gain enhancement of 0.66–5.96 dBi is obtained, showing its practical potential in the pulse-type HPM system. The evolution process of the proposed antenna can be concluded as follows:

Step 1. The conventional VA is loaded on the substrate with high permittivity to improve the PHC so that the antenna can be applied in the HPM system.

Step 2. In order to further offset the gain loss, a snowflake-like (SFL) unit cell is proposed, and an expansion of the substrate is added on the opening of the exponential curve. Proposed unit cells are designed in numbers and arrangement as a snowflake-like metasurface (SFL-MS) lens embedded on the expanded substrate as an MS lens, which focalizes the electromagnetics to improve the directivity and radiation efficiency.

Step 3. Adding rectangular slits on two brims of the VA, which mitigates the diffracted current, thus broadening the operating band of the VA and further compensating its realized gain in the low-frequency band.

II. ANTENNA DESIGN

A. *Ant I* and *Ant II*

The evolution process of the proposed design in this paper is shown in Fig. 1, where the original antenna, *Ant I*, is a VA on an FR-4 substrate ($\varepsilon_r = 4.3$, $\tan\sigma = 0.025$). The exponential function of the VA is $y = ae^{(r*x)} + b$. A gradient microstrip line and a sector balun are employed to improve the impedance match. According to the calculating method of PHC at a certain frequency point:

$$PHC = P_{in} * \left(\frac{E_{air}}{E_{max}}\right)^2, \quad (1)$$

where input power P_{in} is 0.5 W, breakdown E-field intensity E_{air} in the air is 3^*10^6 V/m, and E_{max} is the maximum E-field distribution of the target antenna. From equation (1), it is evident that lowering the value of E_{max} is helpful to increase PHC. The polarization ability of electric charge in the E-field is proportional to the permittivity. In other words, the higher the permittivity, the lower the intensity of the E-field distribution. Though the PHC of the antenna on a substrate with high permittivity is greatly improved, the radiation efficiency will be much limited, which leads to a discount effect in the HPM application. After comprehensive consideration among the PHC, realized gain, and fabricated cost, in this design, a substrate named TP-1020 ($\varepsilon_r = 10.2, \tan\sigma = 0.0015$) of thickness 1.35 mm is employed to substitute the previous one as *Ant II*. Not only is the PHC promotion of the *Ant II* taken into consideration, but acceptable realized gain and fabricated cost are obtained at the same time.

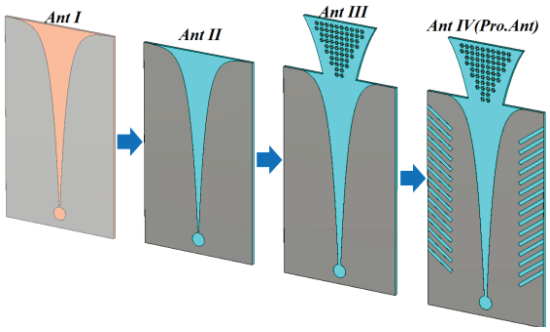

Fig. 1. Evolution process of the antenna design.

It is presented as simulated PHC between the VA on the FR-4 and TP-1020 substrate in Fig. 2 (a). The PHC of the VA on the FR-4 substrate is 20–50% of that on the TP-1020 substrate. Enhancing the PHC of the VA, the substrate with high permittivity also brings loss to the antenna radiation. Simulated VSWR and realized gain are shown in Figs. 2 (b) and (c), where a deterioration of impedance match and a decrease of 0.6–1.6 dBi realized gain are observed.

B. Snowflake-like unit

MS lens constraints electromagnetics and extends its path on the aperture of the VA design. The extension of the propagating path in the MS lens change the electromagnetic phase of the VA, making full use of energy, so that the beam radiates more concentratedly in the end-fire direction. The aim is to realize a transition from a spherical wave compensated by units on different positions (x_u, y_u, z_u) in MS lens to the plane wave:

$$\Delta\phi(x,y) = k_0\left(\sqrt{(x-x_u)^2+(y-y_u)^2+z_u} + d_F\right), \quad (2)$$

where k_0 is wave number in free space and d_F is focal distance.

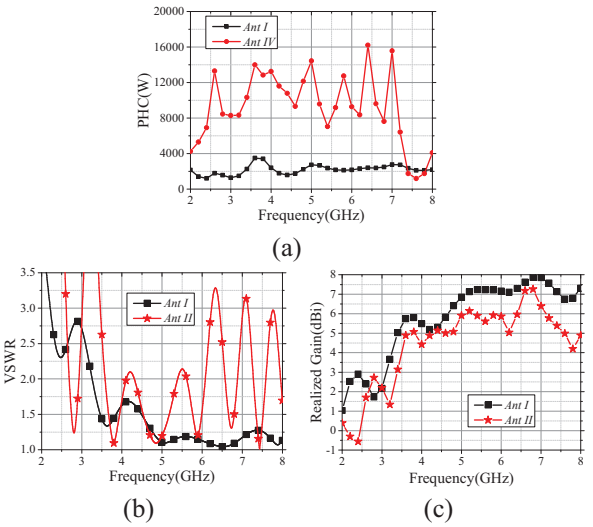

Fig. 2. Comparison of simulated results between *Ant I* and *Ant II* (a) PHC, (b) VSWR, and (c) realized gain.

The core idea of the equivalent medium theory is to simplify MS into a plate of uniform material and isotropic properties. What we ultimately aim to find are the equivalent constitutive parameters that describe this virtual thin plate. According to the transmission theory, equivalent impedance z, refractive index n, dielectric constant, and permeability can be calculated with S_{11} and S_{21}:

$$z = \pm\sqrt{\frac{(1+S_{11})^2 - S_{21}^2}{(1-S_{11})^2 - S_{21}^2}}, \tag{3}$$

$$n = \frac{1}{k_0 d}[\mathrm{Im}(\ln(e^{ink_0 d})) + 2m\pi - i\,\mathrm{Re}(\ln(e^{ink_0 d}))], \tag{4}$$

$$\varepsilon = \frac{n}{z}, \tag{5}$$

$$\mu = n \cdot z. \tag{6}$$

According to the theory of MS lens described in Fig. 3, the principle of the EM wave propagating through two interfaces can be expressed as:

$$\eta_{VA} \cdot \sin(\theta_{VA}) = \eta_{MS} \cdot \sin(\theta_{MS}), \tag{7}$$

where η and θ represent refractive index and angle, respectively. According to equation (7), η_{VA} and θ_{VA} are constant values. To enhance the realized gain for the antenna, the radiated beam should be as accumulated as possible, which means θ_{MS} is bigger than θ_{VA}, and thus η_{MS} of the MS lens design should be minimized as much as possible. It is very suitable to add an MS lens into the *Ant II* model, for there is huge potential in creating a huge refractive difference between the TP-1020 substrate and the MS lens. Therefore, an MS lens with a low refractive index is expected to be constructed to enhance the realized gain of the VA. First of all, a MS lens consisting of SFL unit cells is proposed with a combination of a rectangular strip and its two copies rotating $\pm 60^\circ$ by its geometric center, respectively. Next, the proposed SFL unit cell is set with boundary conditions to extract the electromagnetic parameters of the MHL unit. According to the overall proposed antenna model, the electromagnetic wave propagates along the y axis, which is set to an open boundary. The perfect electrical boundary and the perfect magnetic boundary are set perpendicular to the x and z directions, respectively.

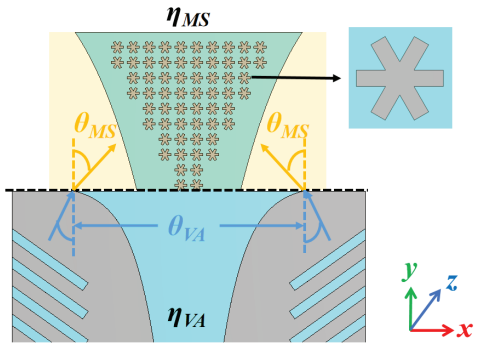

Fig. 3. Schematic diagram of electromagnetic wave propagation at the interface between the air and SFL-MS lens.

According to the relevant theory, the cell size should be no more than $1/10\lambda$. As is simulated in Figs. 4 (a) and (b), there are absent sharp resonances for S-parameter and extracted parameter curves existing over the target frequency range, which reveals that the proposed SFLMS is not resonant in this frequency range. The transmission coefficient is close to 0, which indicates that radiation losses caused by the proposed SFL-MS can be ignored. The equivalent impedance z, refractive index n, *epsilon_r*, and *mu_r* are 0.7, 2.46, 3.48, and 1.65 over the non-resonant frequency band, which is much smaller than that of the imprinted substrate. Such a difference in relative permittivity between the substrate and MS lens is expected to enhance the realized gain of the antenna over a wide band.

C. *Ant III*

The MS lens proposed in this paper is inverted trapezoidal including 10 rows of SFL units, where equal units in quantity are arranged in two adjacent rows: 10 units are put in the top two rows, and there are two units cut when every two rows descend. In the bottom two rows, there are four SFL units on the extra substrate. The substrate is expanded on the opening of two exponential curves, and the MS is added on it. Considering the influence of the position of the lens on the antenna size

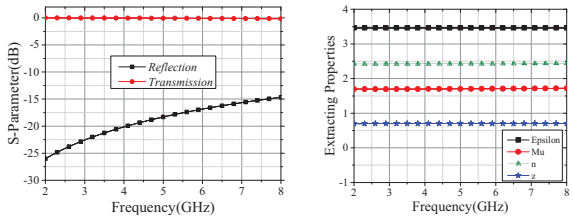

(a) (b)

Fig. 4. Simulated results of SFL-MS unit (a) reflection and transmission and (b) extracted properties.

and radiation characteristic, the model with optimum results is regarded as *Ant III*. In order to reduce the size and weight of the expanded substrate, two curves of its brim are exponential. In Fig. 5 (a), the impedance match of *Ant III* is improved, and its VSWR below 2 covers 3.5–6.68 GHz. Comparisons of realized gain between *Ant II* and *Ant III* are shown in Figs. 5 (a) and (b). Loading the SFL-MS lens, an increase of realized gain of 0.67–3.78 dBi is obtained, which demonstrates its satisfying directional effect.

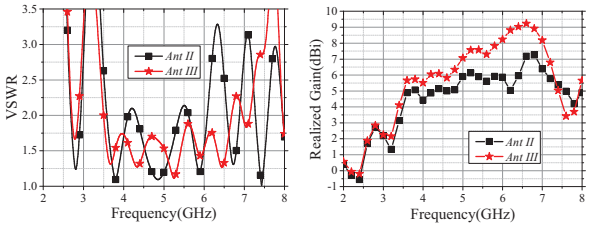

(a) (b)

Fig. 5. Comparison of simulated results between *Ant II* and *Ant III* (a) VSWR and (b) realized gain.

D. *Ant IV*

The surface currents on the VA brims satisfy the following equation:

$$I[s(l)] = I_0 e^{-[qs(l)/p]} \sin\{b_0[s(l) - s(h)]\}, \qquad (8)$$

where q and p represent the curvature and amplitude correction factor, and $e^{-[qs(l)/p]}$ denotes the attenuation term proportional to the frequency. Symbols $s(l)$ and $s(h)$ are the length and height of the tapered slot, respectively. When the frequency decreases, unwanted currents on the VA leave more on the exponential tapered end, which will diffract along the outer brim of the VA and thus decrease the realized gain in the lower frequency. *Ant IV*, the proposed antenna, is based on *Ant III*, where rectangular slits are loaded slantwise on the outer brim of the VA to mitigate the excrescent currents and influence the radiation of the antenna. The configuration of the final antenna design and its detailed parameters are presented in Fig. 6.

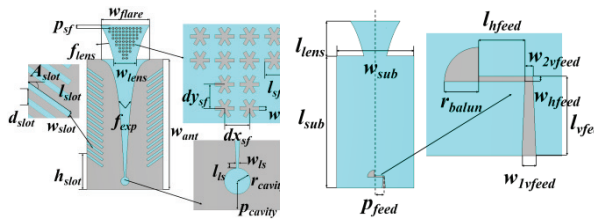

(a) (b)

Fig. 6. Configuration of the proposed antenna (a) front view (b) back view. $w_{flare} = 34$ mm, $p_{sf} = 2$ mm, $w_{lens} = 15.5$mm, $l_{sf} = 2.32$ mm, $w_{sf} = 0.41$ mm, $dx_{sf} = 2.4$ mm, $dy_{sf} = 2.3$ mm, $A_{slot} = 36^\circ$, $l_{slot} = 13.6$ mm, $w_{slot} = 1.4$ mm, $d_{slot} = 4.3$ mm, $h_{slot} = 24.7$ mm, $w_{ls} = 0.8$ mm, $l_{ls} = 1.3$ mm, $r_{cavity} = 2.9$ mm, $p_{cavity} = 5.7$ mm, $w_{sub} = 53$ mm, $l_{sub} = 101.6$ mm, $p_{feed} = 5.9$ mm, $r_{balun} = 4.9$ mm, $l_{hfeed} = 6$ mm, $l_{vfeed} = 8.3$ mm, $w_{hfeed} = 0.9$ mm, $w_{1vfeed} = 2.2$ mm, $w_{2vfeed} = 0.8$ mm, $a_{flare} = -97$, $b_{flare} = 91 r_{flare} = 0.27$, $a_{lens} = -86$, $b_{lens} = -38$, $r_{lens} = 0.1$.

With rectangular slits, simulated E-field distributions of *Ant IV* at 3 GHz are presented in Fig. 7 (a), which are accumulated on rectangular slits and the top of the substrate. Introducing slits on the brims, surface currents on the brims are excited, and paths that currents pass are extended so that the effective size of the antenna design is enlarged and a bandwidth increase is realized in low frequencies. The worthiness of rectangular slits could be visualized by comparison of simulated VSWR and realized gain between *Ant III* and *Ant IV* presented in Figs. 7 (b) and (c), where impedance match and radiation of *Ant IV* are much improved in the low operating band. Simulated VSWR below 2 covers 2.57–6.72 GHz, and an expansion of 0.93 GHz of *Ant IV* is obtained in the low frequency band, which shows the ideal miniaturized effect of rectangular slits. Simulated realized gain reaches 6.61–8.84 dBi in this band. At 3 GHz, the simulated realized gain of *Ant IV* increases 6.4 dBi and 7 dBi compared to that of *Ant III* and *Ant I*, respectively. In the high band, however, the realized gain of *Ant IV* decreases a little due to the coupling between the snowlike MS and rectangular slits. Figure 7 (d) shows simulated PHC between *Ant I* and *Ant IV*. The minimum simulated PHC in the operating band of *Ant IV* is 8.3 MW, which is much bigger than simulated value of *Ant I*, demonstrating its value in applying to the HPM system.

Simulated radiation patterns of evolutionary VA at different frequency points are listed in Figs. 8 (a)–(d). Owing to the loading of rectangular slits and MS, it can be seen that the E-plane obtains a more significant

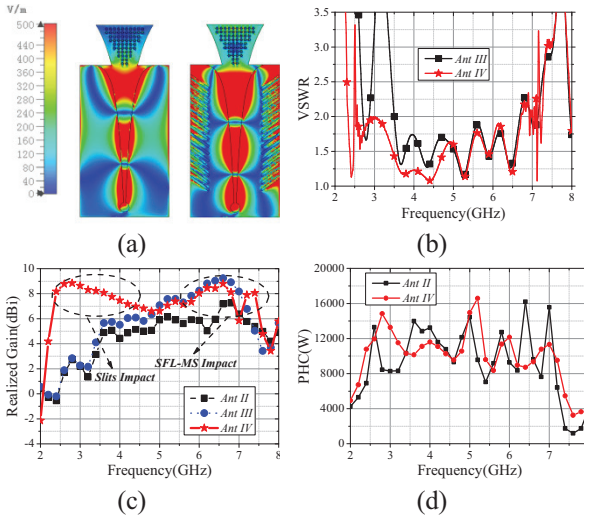

Fig. 7. Comparison of simulated results between *Ant III* and *Ant IV* (a) E-field distribution at 3 GHz, (b) VSWR, (c) realized gain, and (d) PHC.

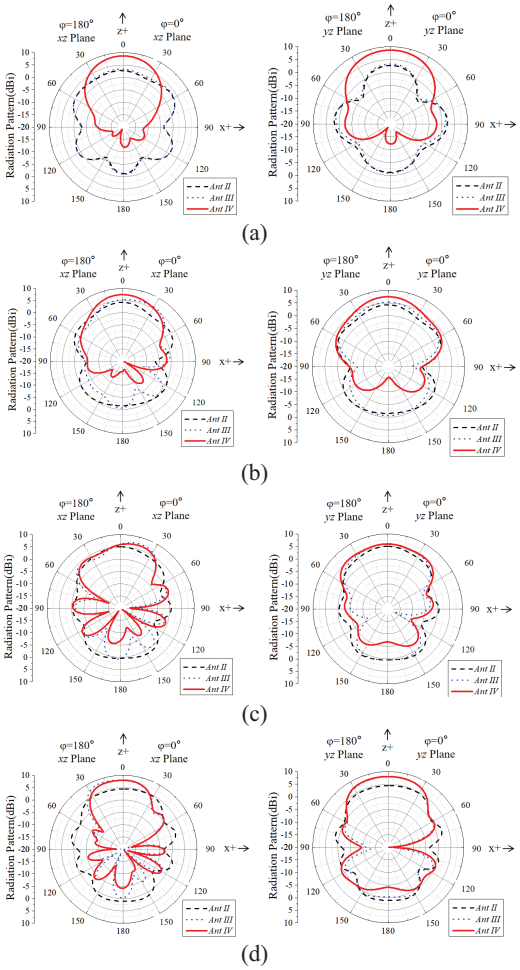

Fig. 8. Comparison of *E*-plane (left) and *H*-plane (right) radiation patterns among *Ant II*, *Ant III*, and *Ant IV* (a) 3 GHz, (b) 4 GHz, (c) 5 GHz, and (d) 6 GHz.

effect of beam narrowing than the *H*-plane. In the low-frequency band, the realized gain of *Ant IV* is obviously bigger than that of *Ant II* and *Ant III*, and its main lobe radiates along the axis. For the asymmetry of antenna feeding, a slight deviation of the main lobe will occur at middle and high frequencies. With frequencies increasing, there is a significant growth in the magnitude of the back lobe. In the E-plane, the 3 dB beamwidth of *Ant II*, *Ant III*, and *Ant IV* covers 56.6°, 148.6°, and 61.5° at 3 GHz; the 3 dB beamwidth of *Ant II*, *Ant III*, and *Ant IV* covers 143°, 76.6°, and 66.6° at 4 GHz; the 3 dB beamwidth of *Ant II*, *Ant III*, and *Ant IV* covers 104.8°, 48°, and 81.4° at 5 GHz; the 3 dB beamwidth of *Ant II*, *Ant III*, and *Ant IV* covers 98.5°, 57.7°, and 56.8° at 6 GHz. Considering the *H*-plane, the 3 dB beamwidth of *Ant II*, *Ant III*, and *Ant IV* covers 150.8°, 148.6°, and 75.5° at 3 GHz; the 3 dB beamwidth of *Ant II*, *Ant III*, and *Ant IV* covers 86.2°, 77.6°, and 81° at 4 GHz; the 3 dB beamwidth of *Ant II*, *Ant III*, and *Ant IV* covers 76.3°, 57.7°, and 78.1° at 5 GHz; the 3 dB beamwidth of *Ant II*, *Ant III*, and *Ant IV* cover 66.6° at 6 GHz. As for sidelobe characteristic, considering the symmetry and relative stability in the *H*-plane, only sidelobes in the *E*-plane are discussed. The sidelobe levels of *Ant II*, *Ant III*, and *Ant IV* reach −0.6 dB, −2.3 dB, and −19.3 dB at 3 GHz; sidelobe levels of *Ant II*, *Ant III*, and *Ant IV* reach −3.3 dB, −5.3 dB, and −9.3 dB at 4 GHz; sidelobe levels of *Ant II*, *Ant III*, and *Ant IV* reach −3.4 dB, −3.2 dB, and −5.9 dB at 5 GHz; sidelobe levels of *Ant II*, *Ant III*, and *Ant IV* reach −2.5 dB, −7 dB, and −7 dB at 6 GHz.

A comparison among *Ant II*, *Ant III*, and *Ant IV* with respect to bandwidth, realized gain, 3 dB beamwidth, sidelobe, and PHC are listed in Table 1. The observed frequency points are 3 GHz, 4 GHz, 5 GHz, and 6 GHz.

Table 1: Comparison among four evolution phases

Ant Phase	Bandwidth (GHz)	Realized Gain (dBi)	PHC (kW)
Ant I	3.26–8+	2.2/5.5/6.8/7.2	1.3/2.4/2.7/2.2
Ant II	4.31–5.39	2.2/4.4/5.9/5.8	8.3/13.2/14.4/9.3
Ant III	3.5–6.68	2.3/5.52/7.1/8.2	8.5/15.2/14.2/11.9
Ant IV	2.57–6.72	8.7/7.5/6.6/8.1	12.1/10.5/13.5/11

III. FABRICATION AND VERIFICATION

To validate simulated results of the proposed antenna, a prototype of the antenna model is fabricated as shown in Figs. 9 (a)–(c). An SMA-KE probe is employed for feeding, whose inner conductor and two pillars are connected with the microstrip balun on the back and the metal part on the front, respectively. The substrate and the feeding probe are clamped well

due to the space between the inner conductor and two pillars. Compared to the all-metal HPM antenna, it takes advantage of the lightweight characteristic of the subloaded antenna. Weighed on the electronic scale, the proposed antenna is 19.4 g, which will greatly promote the movability of the HPM system. The antenna design is measured and verified in the anechoic chamber.

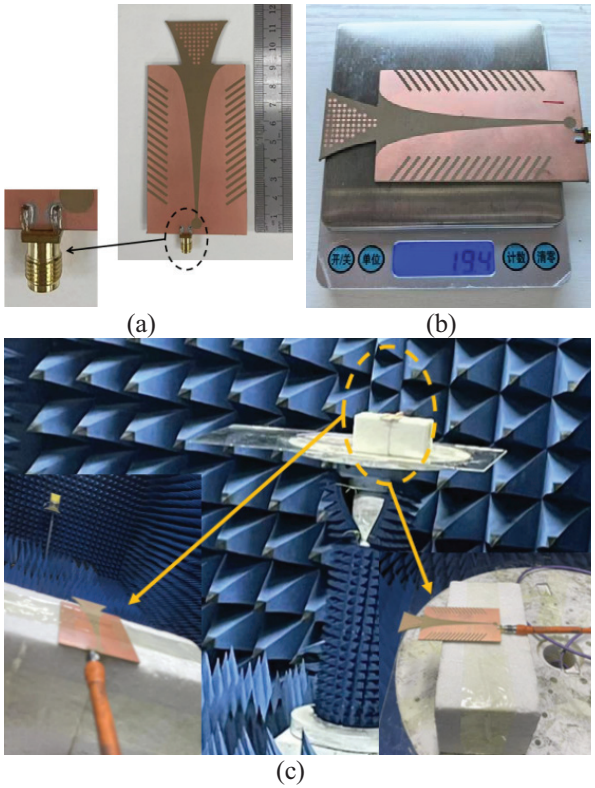

Fig. 9. Fabrication of the proposed antenna: (a) prototype, (b) on the electronic scale, and (c) experimental verification in the anechoic chamber.

Simulated and measured VSWR results of the proposed antenna are exhibited in Fig. 10 (a). The measured VSWR below 2 and 2.5 covers 2.28–6.54 GHz and 2.21–7.17 GHz. In the band of 6.54–6.75 GHz, however, measured VSWR values are over 2. Simulated and measured realized gain results of the proposed antenna are shown in Fig. 10 (b), which are in accordance with each other. The measured realized gain can reach 6.56–8.15 dBi in the operating band. At middle frequencies, measured realized gain results are greater than simulated results. The black dotted line represents the simulated realized gain of *Ant II* and serves as a reference value for gain-enhancement calculation. Simulated and measured gain-enhancements are the blue dashed sequential line and blue discrete stars, which are attained by the deviation calculation between the proposed and the reference

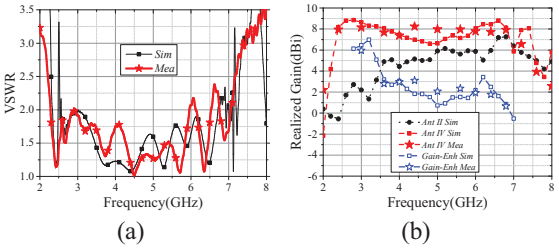

Fig. 10. Simulated and measured results of the proposed antenna (a) VSWR and (b) realized gain.

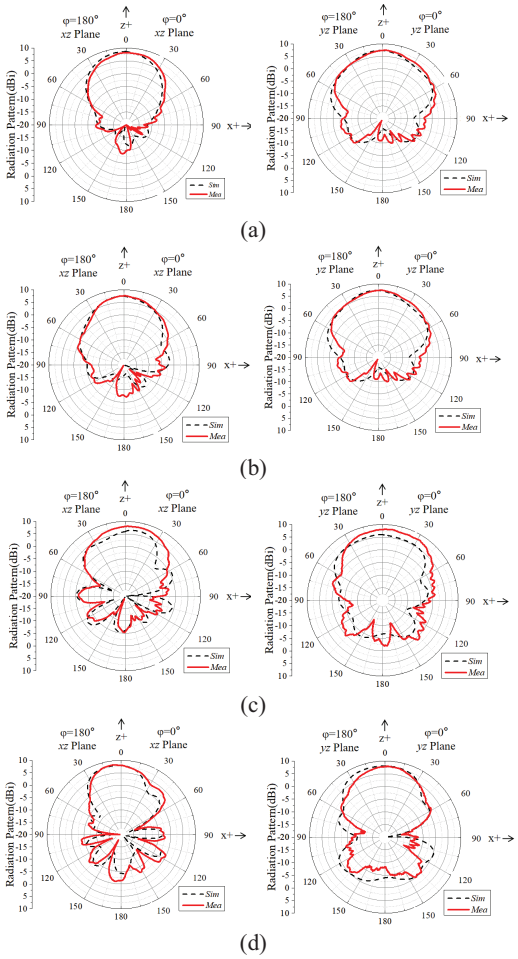

Fig. 11. Simulated and measured *E*-plane and *H*-plane radiation patterns of the proposed antenna: (a) 3 GHz, (b) 4 GHz, (c) 5 GHz, and (d) 6 GHz.

antenna, among which a 0.66–5.96 dBi realized gain-enhancement is obtained in the operating band, and the maximum value is at 3 GHz.

Simulated and measured *E*-plane and *H*-plane radiation patterns of the proposed antenna at different frequency points match well, as shown in Figs. 11 (a)–(d). It is observed that, due to the loading of the SFL-MS, the *E*-plane obtains an evident effect of beam narrowing

than the H-plane both on the simulation and measurement. In the E-plane, the measured 3 dB beamwidth of the proposed antenna cover 61°, 59.6°, 75°, and 51.9° at 3 GHz, 4 GHz, 5 GHz, and 6 GHz, respectively. In the H-plane, the measured 3 dB beamwidth of the proposed antenna cover 68.4°, 99.7°, 87.5°, and 62° at 3 GHz, 4 GHz, 5 GHz, and 6 GHz, respectively. The measured sidelobe levels in the E-plane of proposed antenna reach −10.7 dB at 3 GHz, −11.7 dB at 4 GHz, −8.4 dB at 5 GHz, and −7.6 dB at 6 GHz. In the H-plane, the simulated and measured sidelobe levels reach −10.5 dB at 3 GHz, −10.1 dB at 4 GHz, −0.4 dB at 5 GHz, and −6.7 dB at 6 GHz. Considering the dielectric loss and impedance mismatch brought by the substrate and weld craft, as well as machining and assembly tolerance, the deviation between the simulation and measurement is reasonable and the results are convincing enough to prove the performance of the proposed antenna.

As shown in Figs. 12 (a)–(c), an experiment was conducted to verify the ability in the HPM application of the proposed antenna. Specifically, a pulse-type HPM source, which outputs a pulse of 5000 W at 6 GHz, is included in the experience. Two proposed designs are of the proposed antenna. Specifically, a pulse-type HPM source, which outputs a pulse of 5000 W at 6 GHz, is included in the experiment. A proposed design and a horn antenna are involved as transmitting and receiving antennas, respectively. In the receiving terminal, a power meter is employed to monitor waveform variation. The average and peak power are 18.34 dBm and 19.92 dBm

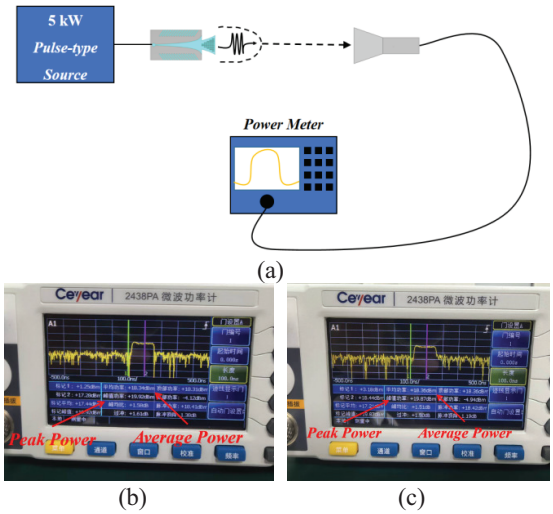

Fig. 12. Proposed antenna under high-power pulse-type: (a) diagram of the experiment, (b) 0 min, and (c) 5 min.

in 0 min. In 5 min they are 18.36 dBm and 19.87 dBm, respectively. There were no unexpected sounds, sparks, or smoke during the test. After the experiment, the outlook of the proposed antenna remained basically unchanged except for a high temperature on the surface, which may lead to metal falling off and further influence the lifetime of the proposed antenna.

IV. COMPARISON AND DISCUSSION

To better understand the proposed work in this paper, an investigation into relative public

Table 2: Investigation of VA designs for gainenhancement techniques

Ref.	ε_r	Oper. Band (GHz)	Gain-Enh Method	Max Enh-Gain (dBi)
[11]	2.2	3.5–7/26.5–40	Dual-Function Taper Slot	2
[12]	2.5	2.4/5.2/5.8	MS	2.4
[13]	2.2	24.25–29.5	MS	3.16
[14]	2.2	5.4–18	MS	3.2
[17]	2.2	1–6	MS Lens	4.8
[18]	4.4	1.27–9.4	MS	2
[19]	2.2	0.45–10	MS Layer	6
[21]	3.55	1.5–55	MS Lens	5.5
[22]	3.48	22.5–45	MS Lens	6
[23]	3.55	10.2–41.75	MS Lens	4
[24]	10.2	3–9	MS/SSPP	3.75
[25]	3	1–28	Director/MS	4.5
[26]	3.55	15–27	MS/SSPP	2
[27]	2.2	0.45–10	MS/CCSC	3
This Work	**10.2**	**2.28–6.54**	**Slits/MS**	**5.96**

The values of **Max Enh-Gain** (Maximum Enhanced-Gain) are approximate according to the data given by listed Refs.

gain-enhanced VA design referring to operating band, sub, and gainenhanced method is listed in Table 2. Depending on the application, each antenna design has its positive and negative aspects. The proposed antenna obtains a satisfying maximum enhanced-gain 5.96 dBi benefit from the SFL-MS and slits with a relatively narrow operating band compared to the ultra-wideband characteristic of other VA designs for its PHC demand.

V. CONCLUSION

An HPM VA based on the substrate is proposed and verified in this paper. A substrate with high permittivity is employed to improve PHC so that the proposed antenna can sustain the energy released by the HPM source. An SFL-MS lens and rectangular slits are studied and added to the antenna design, which compensates for the radiation loss caused by the loading of the substrate and improves the directivity and impedance match. The prototype is fabricated and measured in a microwave anechoic chamber, whose results are acceptable and in reasonable agreement with simulated results, demonstrating its satisfying prospects in the solid-state HPM system.

ACKNOWLEDGMENT

This work is supported by National Key Laboratory of Science and Technology on Electromagnetic Environment Effects program (Grant No. JCKYS2025DC01) and the Science and Technology Innovation Program of Hunan Province under Grant 2023RC3265.

REFERENCES

[1] B. Wu, X.-Y. Sun, H.-R. Zu, and H.-H. Zhang, "Transparent ultrawideband halved coplanar Vivaldi antenna with metal mesh film," *IEEE Antennas Wireless Propag. Lett.*, vol. 21, no. 12, pp. 2532–2536, 2022.

[2] K. Zhang, R. Tan, Z. H. Jiang, Y. Huang, and L. Tang, "A compact, ultrawideband dual-polarized Vivaldi antenna with radar cross section reduction," *IEEE Antennas Wireless Propag. Lett.*, vol. 21, no. 7, pp. 1323–1327, 2022.

[3] C. Zhao, Y. Bai, and Q. Wei, "A 2 to 50 GHz all-metal Vivaldi antenna for ultra-wideband (UWB) application," *Int. J. Electron. Commun.*, vol. 148, no. 9, p. 154162, 2022.

[4] Z. Chen, R. Yin, Y. Jiang, and X. Mao, "An all-metal antipodal Vivaldi antenna design for high-power microwave application," *Applied Computational Electromagnetics Society (ACES) Journal*, vol. 39, no. 12, 2024.

[5] T. H. Lim, S. Park, C. S. Lee, and J.-R. Park, "A broadband dual-slant polarized metal Vivaldi antenna for a high-power jammer," in *2020 International Symposium in Antennas and Propagation (ISAP)*, Osaka, Japan, pp. 485–486, Jan. 2021.

[6] S. Ohm, E. Kang, T. H. Lim, and H. Choo, "Design of a dual-polarization all-metal Vivaldi array antenna using a metal 3D printing method for high-power jamming systems," *IEEE Access*, vol. 11, pp. 35175–35181, 2023.

[7] Y. Chuo, L. Ziting, L. Qiang, and D. Haosheng, "Design of a metal Vivaldi antenna with wide band and dual polarization," in *2021 IEEE International Workshop on Electromagnetics: Applications and Student Innovation Competition (iWEM)*, Guangzhou, China, pp. 1–3, Nov. 2021.

[8] X. Ma, S. Chai, K. Xiao, L. Ding, K. Xiao, and L. Ding, "Design of all-metal Vivaldi phased array antenna," in *2018 IEEE 3rd International Conference on Signal and Image Processing (ICSIP)*, Shenzhen, China, pp. 547–551, Jul. 2018.

[9] M. Wang, L. Crocco, and M. Cavagnaro, "Antipodal Vivaldi antenna with ceramic cone lens for biomedical microwave imaging systems," in *2021 15th European Conference on Antennas and Propagation (EuCAP)*, Dusseldorf, Germany, pp. 1–5, Mar. 2021.

[10] C. Rusch, J. Schäfer, T. Kleiny, S. Beer, and T. Zwick, "W-band Vivaldi antenna in LTCC for CW-radar nearfield distance measurements," in *Proceedings of the 5th European Conference on Antennas and Propagation (EUCAP)*, Rome, Italy, pp. 2124–2128, Apr. 2011.

[11] M. Wang, L. Crocco, S. Costanzo, and R. Scapaticci, "A compact slot-loaded antipodal Vivaldi antenna for a microwave imaging system to monitor liver microwave thermal ablation," *IEEE Open Journal of Antennas and Propagation*, vol. 3, pp. 700–708, 2022.

[12] J. Ren, M. Zuo, B. Zhang, and X. Du, "Large frequency ratio Vivaldi antenna system with low-frequency gain enhancement utilizing dual-function taper slot," *IEEE Trans. Antennas Propag.*, vol. 70, no. 6, pp. 4854–4859, 2022.

[13] F. Gunes, I. O. Evranos, M. A. Belen, and P. Mahouti, "A compact triband antipodal Vivaldi antenna with frequency selective surface inspired director for IoT/WLAN applications," *Wireless Networks*, vol. 27, pp. 3195–3205, 2021.

[14] A. S. Dixit and S. Kumar, "Gain enhancement of antipodal Vivaldi antenna for 5G applications using metamaterial," *Wireless Personal Communications*, vol. 121, pp. 2667–2679, 2021.

[15] P. Das, S. Kundu, and R. Kumar, "A near zero refractive indexed non-uniform metasurface for broadband RCS reduction of an antipodal Vivaldi antenna," *Sci. Rep.*, vol. 8563, 2026.

[16] D. E. Bensafieddine, M. T. Taihi, H. Merah, S. M. Chaker, F. Babaghayou, F. Djerfaf, L. Merah, M. Bouzouad, and T. Seghier, "A metafractal cell-based reconfigurable Vivaldi antenna for non-invasive detection of malignant skin tissues,"

AEU-International Journal of Electronics and Communications, vol. 210, p. 156298, 2026.

[17] S. Pan, W. Shen, Y. Feng, and Z. Liu, "Miniaturization and performance enhancement of Vivaldi antenna based on ultra-wideband metasurface lens," *Int. J. Electron. Commun.*, vol. 134, no. 6, p. 153703, 2021.

[18] K. Li, Z. Li, X. Liu, S. Li, X. Qu, Z. Yang, and W.-H. Zong, "A high-gain Vivaldi antenna loaded with metasurface for broadband applications," *Applied Computational Electromagnetics Society (ACES) Journal*, vol. 39, no. 10, pp. 876–884, 2024.

[19] A. Hossain, S. Pancrazio, T. Kelley, and A.-V. Pham, "A compact and low-profile high-gain multilayer Vivaldi antenna based on gradient metasurface superstrates," *IEEE Antennas Wireless Propagation Letters*, vol. 24, no. 6, pp. 1537–1541, 2025.

[20] P. Zhou, M. Li, Q. Chen, P.-F. Gu, and D.-Z. Ding, "Metasurface-loaded ultrawideband differential Vivaldi antenna with reflectionless notched band," *IEEE Antennas and Wireless Propagation Letters*, vol. 25, no. 2, pp. 516–520, 2026.

[21] O. Yesilyurt and G. Turhan-Sayan, "Metasurface lens for ultra-wideband planar antenna," *IEEE Trans. Antennas Propag.*, vol. 68, no. 2, p. 726, 2020.

[22] P. K. Jaiswal, R. Bhattachary, and A. Kumar, "A UWB antipodal Vivaldi antenna with high gain using metasurface and notches," *Int. J. Electron. Commun.*, vol. 159, no. 4, p. 154473, 2023.

[23] A. Azari, A. Skrivervik, H. Aliakbarian, and R. A. Sadeghzadeh, "A super wideband dual-polarized Vivaldi antenna for 5G mmWave applications," *IEEE Access*, vol. 11, pp. 80761–80768, 2023.

[24] J. Liang, C. Chiu, T. Lin, and C. Lee, "An ultrawideband circularly-polarized Vivaldi antenna with high gain," *IEEE Access*, vol. 10, pp. 100446–100455, 2022.

[25] H. Qi and H. Liu, "Wideband high gain differential Vivaldi antenna design based on exponential spoof surface plasmon polaritons metamaterial," *Int. J. Electron. Commun.*, vol. 163, p. 154603, 2023.

[26] X. Shi, Y. Cao, Y. Hu, and X. Luo, "A high-gain antipodal Vivaldi antenna with director and metamaterial at 1–28 GHz," *IEEE Antennas Wireless Propag. Lett.*, vol. 20, no. 12, pp. 2432–2436, 2021.

[27] H. Qi and H. Liu, "Wideband high-gain filtering Vivaldi antenna design based on MS and herringbone SSPP structure," *IEEE Antennas Wireless Propag. Lett.*, vol. 22, no. 8, pp. 1798–1802, 2023.

[28] A. Hossain and A.-V. Pham, "A novel gain-enhanced miniaturized and lightweight Vivaldi antenna," *IEEE Trans. Antennas Propag.*, vol. 71, no. 12, pp. 9431–9439, 2023.

Zichong Chen received the M.E. degree from Hunan University, China, in 2023. He is an engineer for Hunan Vanguard Group Co. Ltd. His research interests include HPM antenna design and solidstate high-power microwave systems with active phased array architecture.

Fangsheng Cai received the M.E. degree from Nanjing University of Aeronautics and Astronautics, China, in 2021. He works full-time as a microwave engineer at Hunan Vanguard Group Co. Ltd. His current research interests include HPM systems based on electric vacuum sources.

Peng Bai received the M.E. degree from Yunnan University, China, in communication engineering in 2023. He works full-time as a microwave engineer at Hunan Vanguard Group Co. Ltd. His current research interests include HPM antenna systems.

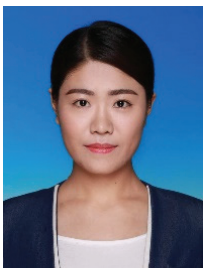

Taijing Shi received the M.S. degree from Beijing University of Chemical Technology, China, in 2019. She works full-time as a senior microwave engineer at Hunan Vanguard Group Co. Ltd. Her current research interests include the HPM effect and assessment.

Xiaojun Mao received the Ph.D. degree from Harbin Engineering University, China, in 2017. He works full-time as a senior microwave engineer at Hunan Vanguard Group Co. Ltd. His current research interests include the HPM overall system design and radar technology.

Yun Jiang received the Ph.D. degree from National University of Defense Technology, China, in 2022. He works full-time as a senior microwave engineer at Hunan Vanguard Group Co. Ltd. His current research interests include HPM overall system design, microwave RF circuits, and radar technology.

A Miniaturized Four-Port MIMO Slotted Microstrip Patch Array Antenna Design With Reduced Mutual Coupling for 5G Wireless Applications

Venkatrao Kolli[1] and Merlin Sheeba G[2]

[1]Research Scholar, School of Electrical and Electronics Engineering
Sathyabama Institute of Science and Technology, Chennai,
Assistant Professor Department of ECE, SRKR Engineering College, Bhimavaram, Andhrapradesh
kolli.venkat436@gmail.com

[2]Department of ECE, Jerusalem College of Engineering, Chennai, India
drmerlinsheebag@gmail.com

Abstract – In this paper, a four-port Multiple-Input Multiple-Output (MIMO) antenna array is designed and analyzed for millimeter-wave (mm-wave) 5G applications. The configuration comprises a slotted microstrip patch array antenna excited through a T-junction power divider/combiner-based feed network. The set of truncated square slots are arranged on a rectangular patch to act as radiating surfaces. Similarly, the ground plane is a combination of rectangular and square-shaped slots used in a ground plane to enhance impedance bandwidth and radiation characteristics. The proposed fourport antenna is fabricated and the prototype is experimentally characterized for the S -parameters ($S_{11}, S_{21}, S_{31}, S_{41}, S_{32}, S_{42}, S_{43}$), radiation pattern, and gain. Typical dimensions of the antenna are $28 \times 28 \times 0.254$ mm^3. Measured results are in excellent agreement with simulated results. The four-port MIMO antenna operates effectively over the 27.45–28.55 GHz frequency range and is suitable for emerging 5G applications with a gain of 10.02 dBi. To introduce the isolation between the adjacent elements in the array, the technique of polarization diversity has been employed. The corresponding enveloper correlation coefficient (ECC) suppression has been noticed. Based on the results, the proposed antenna confirms excellent diversity performance, and hence the design can be a promising solution for mm -wave and 5G applications.

Index Terms – CCL, DG, MEG, MIMO, mm-wave and 5G.

I. INTRODUCTION

Following recent advancements in communication technology, there is exponential growth in wireless devices. As a result, competition for available bandwidth leads to limited channel capacity. This has driven the demand for more advanced and efficient communication technologies. These challenges have accelerated the evolution toward fifth-generation (5G) wireless systems, particularly within the millimeter-wave (mmwave) spectrum, which offers significantly greater bandwidth and channel capacity than conventional microwave bands [1, 2]. The 5G paradigm aims to deliver high-speed data, enhanced reliability, low-latency, and reduced power consumption to accommodate the growing number of interconnected devices while supporting emerging technologies such as autonomous vehicles, the Internet of Things (IoT), and smart cities [3, 4].

Despite these advantages, mm-wave communication systems face substantial challenges including propagation loss, atmospheric attenuation, and signal fading, which become increasingly critical when employing single antenna systems [5, 6]. To address these limitations, a Multiple-Input Multiple-Output (MIMO) has been introduced in modern and next-generation wireless communication systems. MIMO architectures exploit diversity gain and spatial multiplexing for significant improvement. Channel capacity, reliability, and efficiency achieve data throughput in the gigabits per second (GBPS) range [7–9]. For 5G mm-wave operation, antenna systems must exhibit wide bandwidth, high gain, and compact size while limiting mutual-coupling and ensuring consistent performance in dense and multipath conditions.

Recent research has explored various antenna designs for mm-wave 5G systems [10–21, 31]. Early studies proposed low-gain antennas [10, 11] could not compensate for the substantial propagation and atmospheric losses encountered in the mm-wave spectrum. Consequently, high-gain beam-steering array configurations were introduced to achieve strong directional radiation and improved spatial coverage [12–14]. However, conventional multi-element arrays,

Submitted On: November 03, 2025
Accepted On: April 22, 2026

https://doi.org/10.13052/2026.ACES.J.410407

typically excited by a single feed port, fail to achieve true MIMO functionality, thus limiting their capacity enhancement. MIMO antennas composed of multiple independently fed radiators for multipath propagation and spatial diversity result in higher data rates, increased link robustness, and improved spectral efficiency characteristics essential for 5G mm-wave applications. Several designs were proposed with different electromagnetic structures for 5G applications [10–16]. Correspondingly, an electromagnetic band gap (EBG) MIMO antenna provided 0.8 GHz bandwidth [15]. Substrate-integrated waveguide (SIW)-fed MIMO structures with moderate gain and bandwidth performance suitable for 5G terminals are demonstrated in [13]. Compact multi-element geometry, such as T-shaped MIMO antennas [17], 8×8 large-scale MIMO arrays [18, 30], and metamaterial-integrated designs [19], achieve gains ranging from 7 to 14 dBi across the 25–37 GHz bands. These designs demonstrate promising results, however many are limited by complex geometries and narrow bandwidths. The proposed antenna exhibits compact, high gain, significant radiation characteristics, bandwidth, and excellent MIMO characteristics. Hence, the design is suitable for applications such as smartphones, wearable electronics, and mobile hotspots.

II. SLOTTED MICROSTRIP PATCH ARRAY DESIGN

The initial design has a simple rectangular patch of dimensions defined by 'Wp' and 'Lp' as a substrate of 'Ws' width and 'Ls' length. The substrate has a thickness of 0.254 mm. This patch antenna is excited by a simple transformer based microstrip line. The structure is shown in Fig. 1 (a). A single element with four symmetrically arranged slots is presented in Fig. 1 (b). The corresponding ground has been modified into a defective ground structure (DGS) as shown in Fig. 1 (c). This has been extended by arranging two more sets of four slots symmetrically on either side of the center slots. This achieves a final radiating surface with 12 slots equally spaced, which are assumed as eight sets of slots as shown in Fig. 1 (d). The corresponding ground distribution is based on three sets of DGS, one for each set of radiating slots, as shown in Fig. 1 (e). The design has been extended further to a two-element array configuration, each excited by a power divider as presented in Fig. 1 (f). The corresponding DGS is shown in Fig. 1 (g).

A. Proposed single element slotted array antenna design

Initially, a proposed single element slotted array microstrip patch antenna is designed to operate at 28 GHz and is devised following the standard design equations provided in Equations (1)–(4). The design starts with the basic impedance-matching microstrip feed to the rectangular patch. The single-element configuration serves as the fundamental building block for subsequent array and MIMO designs. The basic design/single element rectangular microstrip patch antenna is designed using the mathematical equations

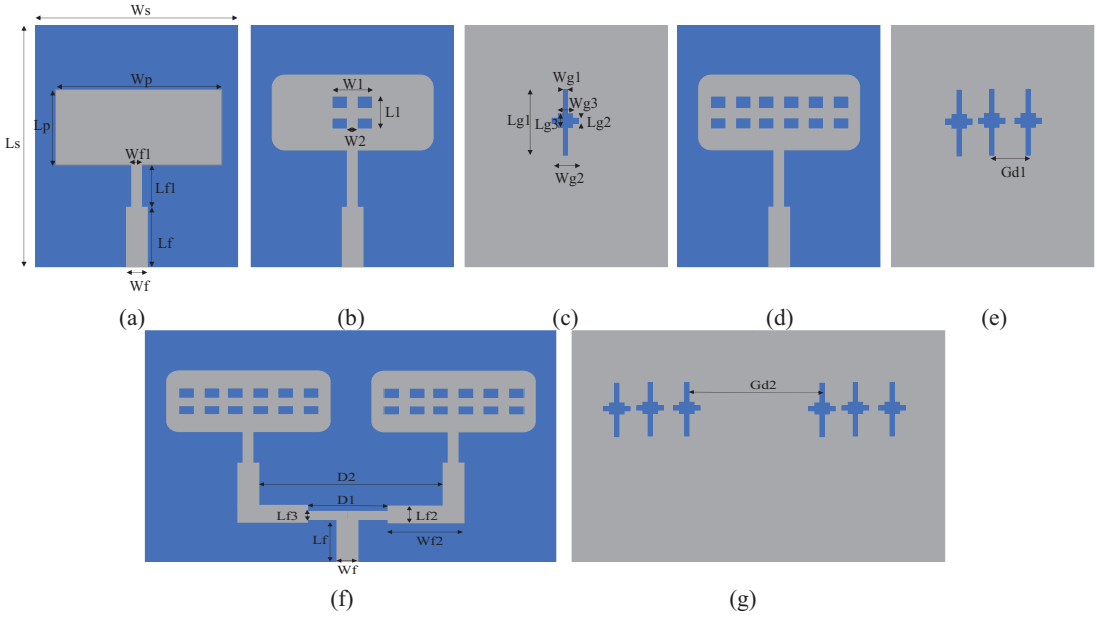

Fig. 1. (a) Design 1, (b) design 2, (c) DGS ground, (d) proposed slotted array antenna, (e) symmetrical DGS ground structure, (f) proposed antenna with power divider, and (g) ground plane.

provided in [20]. From the geometry, Lp and Wp are patch length and width.

The optimized geometrical parameters of the design are given in Table 1.

Table 1: Optimized four-port MIMO slotted array antenna design parameters

S. No	Parameters	Value (mm)	S. No	Parameters (mm)	(mm)
1	Ls	9	2	Ws	9
3	H	0.254	4	Lp	3.2
5	Wp	5.5	6	Wf	0.75
7	Wf1	0.25	8	Lf	1.5
9	Lf1	1.8	10	W1	1
11	L1	1	12	W2	0.2
13	Wg1	0.25	14	Lg1	3
15	Wg2	0.7	16	Lg2	0.2
17	Wg3	0.5	18	Lg3	0.5
19	Gd1	1.25	20	Gd2	6
21	Wf2	3	22	Lf2	0.75
23	Lf3	0.22	24	L2	16
25	W3	0.6	26	D1	3.6
27	D2	8.5	28	D3	1.5
29	D4	1.5			

B. Two-element antenna array with power divider

The two-element array configuration is excited using a parallel feed network incorporating a T-junction power divider. The feed is matched with a 50 Ω line, while the branched sections are matched to 100 Ω. The inter-element spacing is maintained at approximately 0.85 λ (≈8.5 mm) to ensure low mutual coupling and a compact geometry. The optimized two-element array demonstrates enhanced bandwidth and improved gain compared to the single element configuration. From initial design to final design, the corresponding simulated reflection coefficient plots are presented in Fig. 2.

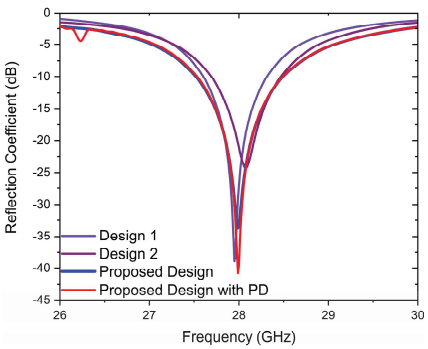

Fig. 2. Simulation results for the reflection coefficient of the antenna Design 1, Design 2, slotted array design, and proposed design with PD.

Simulation results of Design 1, Design 2, slotted array design, and two element slotted array design with PD are presented in Fig. 2. Bandwidth increases from 0.7 GHz to 1.1 GHz due to incorporation of the DGS. Simulations are carried out in CST software with very fine mesh used for improving the accuracy of the simulation results.

III. FOUR-PORT MIMO SLOTTED MICROSTRIP PATCH ANTENNA DESIGN AND ANALYSIS

MIMO configuration of the proposed slotted array has been realized using four port excitations. The geometry includes four elements, where each element corresponds to the array geometry given in Fig. 1 (f). These four elements are arranged to form a four-port excitation suitable for MIMO operations as illustrated in Fig. 3 (a). The corresponding ground plane incorporates the DGS and is arranged as shown in Fig. 3 (b). The inclusion of slots significantly improves the MIMO characteristics, resulting in higher gain and stable radiation performance in the resonating frequency band. The size of the proposed MIMO configuration is $28 \times 28 \times 0.254$ mm^3. Photographs of the fabricated prototype, showing top and back views, are presented in Figs. 3 (c) and (d).

Scattering (S) parameters are experimentally characterized using a Keysight N5224B PNA. Simulated and measured S-parameters are presented in Figs. 4 and 5. The obtained bandwidth from these results spans 27.45–28.55 GHz which falls within the 5G spectrum. The remaining MIMO elements demonstrate comparable reflection profiles, with only minor frequency shifts attributed to fabrication tolerances and mutual coupling effects. The measured impedance bandwidth is approximately 1.1 GHz. The transmission coefficient (S_{21}) characteristics, illustrated in the Fig. 5, confirm that the antenna system maintains sufficient isolation between ports. Isolation between ports is ~ -27 dB between Antenna 3 and Antenna 4. This validates the effective decoupling performance of the proposed MIMO configuration.

The simulated and measured results demonstrate strong agreement, confirming the performance characteristics of MIMO antenna. Minor discrepancies observed are primarily attributed to fabrication tolerances, connector losses, and the influence of coaxial cables during measurements. The measured performance validates the suitability and practical feasibility of the proposed MIMO antenna, particularly for 5G communication applications.

Figure 5 presents the simulated transmission characteristics of the configuration. From the measured

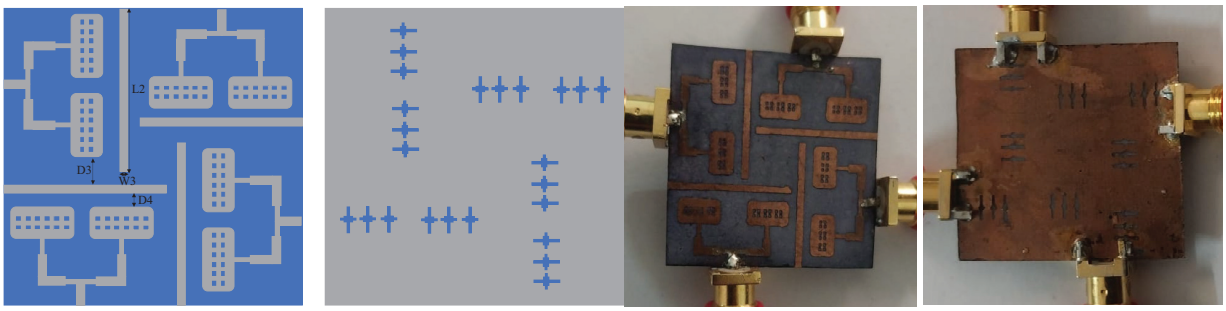

Fig. 3. (a) Proposed four-port MIMO structure, (b) DGS based ground plane, (c) fabricated prototype of four-port MIMO antenna, and (d) fabricated prototype MIMO antenna DGS ground plane.

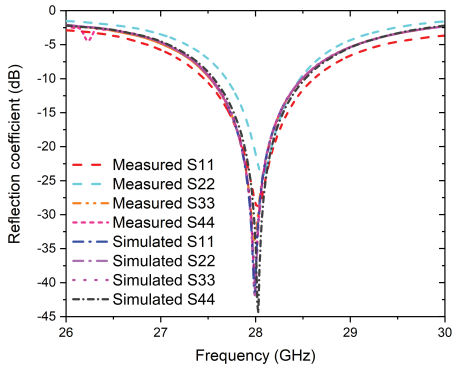

Fig. 4. Simulated vs measured reflection coefficient of the proposed four-port MIMO antenna.

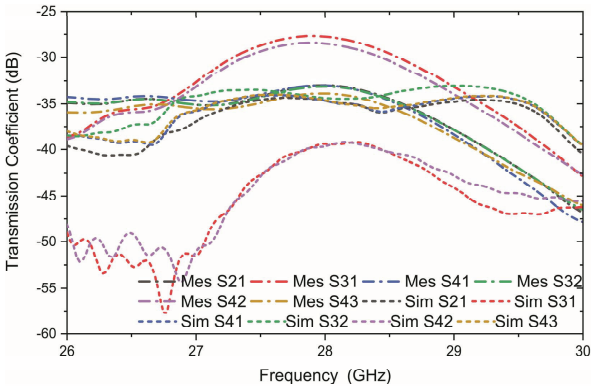

Fig. 5. Simulated vs measured transmission coefficient of the proposed four-port MIMO antenna.

results, the isolation between port 1 and port 2 is relatively low, with a similar trend observed between port 3 and port 4, owing to their close physical proximity and parallel orientation. Conversely, a notable improvement in isolation is achieved among the antenna pairs (1–3), (1–4), (2–3), and (2–4), indicating reduced mutual coupling between diagonally positioned elements. To further mitigate coupling effects, slots are incorporated into the structure. As shown in Fig. 5, the inclusion of these slots significantly enhances isolation between the radiating elements, achieving a minimum isolation better than -25 dB across the operational frequency band. For the measurements, 2.92 mm K-connectors are used, as these connectors are suitable for high frequency applications.

IV. ANALYSIS OF THE MIMO ANTENNA WITH PRACTICAL REALIZATION AND EXPERIMENTAL RESULTS

It is essential to evaluate the performance in terms of the corresponding radiation characteristics. Accordingly, the polar radiation pattern plots for $\phi = 0^\circ$ and 90° are simulated in both E- and H-planes. Similarly, these patterns are measured using an experimental setup comprising an anechoic chamber. The measurement setup includes a horn antenna operating in the transmitting mode, while the designed antenna under test acts as the receiving antenna. The corresponding main lobe is positioned at -2° in both the pattern plots presented in Figs. 6 (a) and (b) at 27.5 GHz and 28 GHz, respectively. Furthermore, the results indicate good agreement between the simulated and measured patterns. It is noteworthy that far-field measurement systems are typically less accurate for compact antennas of 5G frequencies where alignment sensitivity and chamber reflections can introduce additional measurement discrepancies.

The proposed four-port MIMO slotted array antenna reported a simulated peak gain of 10.1 dBi while the measured peak gain is 10.02 dBi for port 1. However, the antenna exhibits a stable 3 dB gain variation from 27.45–28.55 GHz.

V. MIMO PARAMETERS AND COMPARATIVE ANALYSIS OF THE PROPOSED ANTENNA

It is essential to evaluate the performance of MIMO antennas in terms of diversity parameters. Certain threshold levels for these parameters are well established

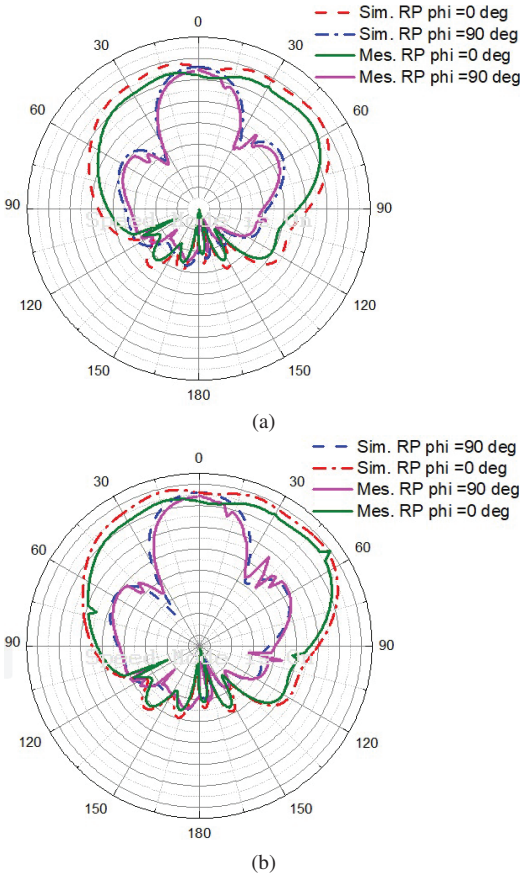

Fig. 6. Simulation vs measured 2D radiation patterns of the proposed four-port MIMO antenna at (a) 27.5 and (b) 28 GHz.

in the literature and our current task is to compute and compare the proposed MIMO structure. The most relevant metrics are enveloper correlation coefficient (ECC), Mean Effective Gain (MEG), Channel Capacity Loss (CCL) and Directive Gain (DG), each having its own functional implication of the performance of the MIMO. For instance, ECC is responsible for quantifying the received signals with respect to the ports. Higher ECC indicates lower isolation. The larger values of ECC can degrade the performance of MIMO inducing mutual coupling. It is also possible to evaluate the spatial diversity through the computed ECC in MIMO antennas [21]. The computation is based on the received signal envelope, S-parameters, and the corresponding radiation pattern characteristics. The mathematical expression as a function of S-parameters is:

$$ECC = \frac{|S_{ii} * S_{ij} + S_{ji} * S_{jj}|^2}{(1 - |S_{ii}|^2 - |S_{ij}|^2)(1 - |S_{jj}|^2 - |S_{ji}|^2)}. \quad (1)$$

Figure 7 represents the simulated versus computed ECC of the proposed four-port MIMO antenna over the 26–30 GHz frequency band. ECC values for all port combinations remain extremely low, well below the critical threshold of 0.5 and, in most cases, below 0.005. That confirms the excellent isolation as well as minimal correlation between antenna elements. Such low ECC ensures that the antenna ports operate independently, enabling effective spatial and polarization diversity which are essential for enhancing MIMO channel capacity and overall link reliability.

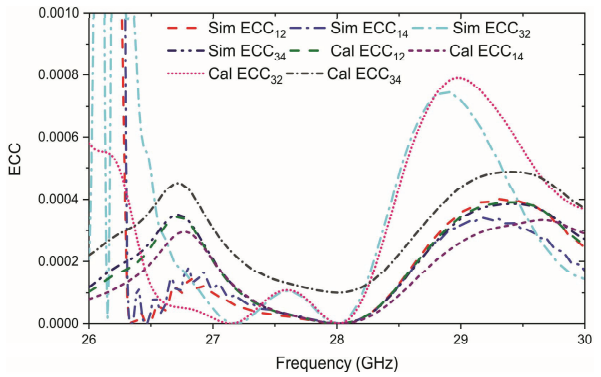

Fig. 7. Simulated vs calculated ECC of the proposed four-port MIMO antenna across all ports.

The ECC limit for practical antennas is <0.5, which is considered suitable for uncorrelated MIMO antennas [24]. DG is another crucial parameter of the MIMO antenna, as it is used for reliability and effectiveness of the received signal in multipath environments. Higher DG values indicate better isolation between the radiating elements in MIMO configuration. An improved DG enhances communication robustness, and higher DG values correspond to greater isolation between the antenna elements [29]. DG for multiple ports of the antenna is:

$$DG = 10\sqrt{1 - (ECC)^2}. \quad (2)$$

Figure 8 shows DG performance of the proposed four-port MIMO antenna in the 26–30 GHz frequency range. DG values remain consistently close to the ideal 10 dB throughout the band, demonstrating the array's high diversity efficiency. Only minor variations are observed below 27 GHz and above 29 GHz, which are negligible and have no significant impact on system performance. The combination of near-ideal DG and very low ECC confirms the proposed four-port MIMO antenna is well suited for high-capacity and reliable 28 GHz MIMO communications.

CCL is one of the MIMO performance parameters which represents the channels capacity of the system during the correlation effect. CCL is:

$$CCL = -\log_2 \det(a), \quad (3)$$

Table 2: Comparison of the four-port MIMO antenna with previous work

Ref.	Frequency (GHz)	Size of the Antenna (mm^3)	Number of MIMO Ports	Gain (dBi)	ECC, DG (dB)
[20]	28, 38	$25 \times 20 \times 0.79$	4	10.4	0.02, Not Provided
[23]	3.6	$150 \times 75 \times 1.6$	8	2.5	<0.01
[24]	28	$41.3 \times 46 \times 0.508$	4	13.1	Not Provided
[25]	24	$15 \times 19 \times 0.254$	2	7.41	0.24, 9.7
[26]	5.2 & 24	$40 \times 25 \times 0.254$	2	5 & 7.37	Not Provided
[27]	30	$48 \times 21 \times 0.13$	2	>7	<0.4, Not Provided
[28]	28	$20 \times 20 \times 0.254$	2	8	0.13, 9.9
[29]	28	$30 \times 35 \times 0.76$	4	8.3	0.01, Not Provided
This Work	28	$28 \times 28 \times 0.254$	4	10.02	<0.0002, >9.9

$$\text{where } a = \begin{bmatrix} \sigma_{11} & \sigma_{12} \\ \sigma_{21} & \sigma_{22} \end{bmatrix}, \tag{4}$$

$$\sigma_{ii} = 1 - (|S_{ii}|^2 - |S_{ij}|^2), \tag{5}$$

$$\sigma_{ij} = -(S_{ii}^* S_{ij} + S_{ji} S_{jj}^*). \tag{6}$$

The calculated CCL of <0.4 bits/Hz is less than the practical standards for the operating frequency range and represents high throughput.

MEG represents the received power in the fading environment:

$$MEG_i = 0.5\mu_{irad} = 0.5\left(1 - \sum_{j=1}^{K} |S_{ij}|\right), \tag{7}$$

where μ_{irad} represents the radiation efficiency, i is the antenna port number and K is the number of antenna elements. The practical standard for MEG is -3 to -12 dB. Calculated MEG for the proposed four-port MIMO antenna is ∼6.5 for all four ports.

Comparative parameters like operating frequency, size of the antenna, number of MIMO ports, gain in dBi, ECC, and DG (dB) are evaluated against the proposed four-port MIMO antenna. Results indicate that the proposed design demonstrates superior performance across various parameters compared to existing works, as summarized in Table 2. The simulated ECC and DG values are 0.0002 and >9.9 dB which represent the proposed four-port MIMO antenna is best candidate for MIMO mm-wave/5G applications.

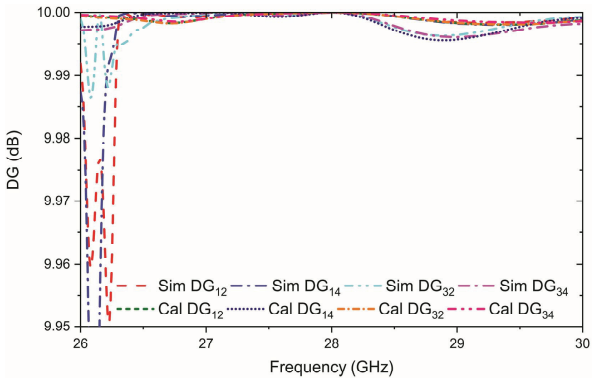

Fig. 8. Simulated vs calculated DG of the proposed four-port MIMO antenna across the ports.

VI. CONCLUSION

This work presents a four-port MIMO slotted array microstrip patch antenna system designed for 5G mm-wave communication applications. Each port of the proposed MIMO configuration consists of a twoelement antenna with PD optimized to achieve enhanced gain, radiation efficiency, and compactness. The antenna operates effectively across the 27.45–28.55 GHz frequency range, offering a measured impedance BW of 1.1 GHz. The prototype demonstrates a peak measured gain of 10.02 dBi, validating its suitability for high throughput communication systems. To comprehensively evaluate MIMO performance, the key diversity parameters such as DG, ECC, CCL, and MEG were evaluated and all exhibit values within practically acceptable limits for reliable 5G operation. The obtained results confirm that the proposed four-port MIMO antenna possesses excellent radiation and diversity characteristics. Therefore, it is a promising design to operate in the 5G spectrum.

REFERENCES

[1] A. Kumar, P. Pattanayak, R. K. Verma, D. Sabat, and G. Prasad, "Two element MIMO antenna system for multiband millimeter-wave, 5G mobile communication, Ka-band, and future 6G applications with SAR analysis," *AEU Int. J. Electron. Commun.*, vol. 171, 2023.

[2] A. A. Althuwayb, M. Alibakhshikenari, B. S. Virdee, N. Rashid, K. Kaaniche, A. B. Atitallah,

A. Armghan, O. I. Elhamrawy, C. H. See, and F. Falcone, "Metasurface-inspired flexible wearable MIMO antenna array for wireless body area network applications and biomedical telemetry devices," *IEEE Access*, vol. 11, pp. 1039–1056, 2023.

[3] A. E. Farahat and K. F. A. Hussein, "Dual-band (28/38 GHz) wideband MIMO antenna for 5G mobile applications," *IEEE Access*, vol. 10, pp. 32213–32223, 2022.

[4] T. S. Rappaport, S. Sun, R. Mayzus, H. Zhao, Y. Azar, K. Wang, G. N. Wong, J. K. Schulz, M. Samimi, and F. Gutierrez, "Millimeter wave mobile communications for 5G cellular: It will work!," *IEEE Access*, vol. 1, pp. 335–349, 2013.

[5] J. L. Wang, T. Liu, X. Wang, M. Wei, and Y. H. Lu, "Four-port low-profile broadband antenna with fan-leaf slits and shorting pins for 5G mobile applications," *Journal of Electromagnetic Waves and Applications*, vol. 38, no. 7, pp. 802–812, 2024.

[6] P. S. B. Shariff, P. R. Mane, P. Kumar, T. Ali, and M. G. N. Alsath, "Planar MIMO antenna for mmWave applications: Evolution, present status & future scope," *Heliyon*, vol. 9, no. 2, Feb. 2023.

[7] P. Sharma, R. N. Tiwari, P. Singh, P. Kumar, and B. K. Kanaujia, "MIMO antennas: Design approaches, techniques and applications," *Sensors*, vol. 22, no. 20, p. 7813, 2022.

[8] A. Ahmad, D.-Y. Choi, and S. Ullah, "A compact two elements MIMO antenna for 5G communication," *Sci. Rep.*, vol. 12, no. 1, Mar. 2022.

[9] M. E. Munir, S. H. Kiani, H. S. Savci, M. Marey, J. Khan, H. Mostafa, and N. O. Parchin, "A four element mm-wave MIMO antenna system with wide-band and high isolation characteristics for 5G applications," *Micromachines*, vol. 14, no. 4, p. 776, 2023.

[10] N. Sghaier, A. Belkadi, I. B. Hassine, L. Latrach, and A. Gharsallah, "Millimeter-wave dual-band MIMO antennas for 5G wireless applications," *J. Infr. Millim. THz Waves*, vol. 44, nos. 3–4, pp. 297–312, Apr. 2023.

[11] B. A. F. Esmail and S. Koziel, "Design and optimization of metamaterial based dual-band 28/38 GHz 5G MIMO antenna with modified ground for isolation and bandwidth improvement," *IEEE Antennas Wireless Propag. Lett.*, vol. 22, pp. 1069–1073, 2023.

[12] A. K. Singh and S. Pal, "Compact self-isolated extremely low ECC folded-SIW-based slot MIMO antenna for 5G application," *IEEE Antennas Wireless Propag. Lett.*, vol. 23, pp. 194–198, 2024.

[13] M. Aboualalaa and I. Mansour, "Dual-band end-fire four-element MIMO antenna array using split-ring structure for mm-wave 5G applications," *IEEE Access*, vol. 11, pp. 57383–57390, 2023.

[14] K. P. Ray, M. D. Pandey, and S. Krishnan, "Determination of resonance frequency of hexagonal and half hexagonal microstrip antennas," *Microw. Opt. Technol. Lett.*, vol. 49, no. 11, pp. 2876–2879, Nov. 2007.

[15] D. Khan, A. Ahmad, and D.-Y. Choi, "Dual-band 5G MIMO antenna with enhanced coupling reduction using metamaterials," *Sci. Rep.*, vol. 14, no. 1, p. 96, Jan. 2024.

[16] A. K. Biswas, S. Biswas, S. Haldar, and A. Nandi, "A highly decoupled flexible 4-element MIMO antenna with band notched characteristics for ultra wide-band wearable applications," *AEU Int. J. Electron. Commun.*, vol. 173, no. 154985, Jan. 2024.

[17] S. F. Jilani and A. Alomainy, "Millimetre-wave T-shaped MIMO antenna with defected ground structures for 5G cellular networks," *IET Microw. Antennas Propag.*, vol. 12, pp. 672–677, 2018.

[18] N. Shoaib, S. Shoaib, R. Y. Khattak, I. Shoaib, X. Chen, and A. Perwaiz, "MIMO antennas for smart 5G devices," *IEEE Access*, no. 6, pp. 77014–77021, 2018.

[19] H. Jiang, L. Si, W. Hu, and X. Lv, "A symmetrical dual-beam bowtie antenna with gain enhancement using metamaterial for 5G MIMO applications," *IEEE Photonics J.*, no. 11, pp. 1–9, 2019.

[20] M. M. Basha, P. Pradeep, G. Srinivasulu, and J. Syed, "Design of compact and high gain dual-band four-port MIMO antenna array for mm-wave 5G communications," *Results in Engineering*, vol. 25, pp. 104–153, 2025.

[21] L. Liu, Y. F. Weng, S. W. Cheung, T. I. Yuk, and L. J. Foged, "Modeling of cable for measurements of small monopole antennas," in *Proceedings of the Loughborough Antennas Propagation Conference (LAPC)*, Loughborough, UK, pp. 1–4, 14–15 Nov. 2011.

[22] I. L. Savarianantham, G. A. A. Mary, A. S. Mazhar, S. Mishra, and G. Jothi, "SIW cavity-backed gain-enhanced circularly polarized metamaterial-loaded dual-band MIMO antenna for WLAN and 5G applications," *Applied Computational Electromagnetics Society (ACES) Journal*, vol. 40, no. 4, pp. 363–372, Apr. 2025.

[23] Y. Yashchyshyn, K. Derzakowski, G. Bogdan, K. Nyzovets, D. Godziszewski, C. H. Kim, and B. Park, "28 GHz switched-beam antenna based on S-PIN diodes for 5G mobile communications," *IEEE Antennas Wirel. Propag. Lett.*, vol. 17, p. 225, 2018.

[24] S. X. Ta, H. Choo, and I. Park, "Broadband printed-dipole antenna and its arrays for 5G applications," *IEEE Antennas Wirel. Propag. Lett.*, vol. 16, pp. 2183–2186, 2017.

[25] A. Iqbal, A. Basir, A. Smida, N. K. Mallat, I. Elfergani, J. Rodriguez, and S. Kim, "Electromagnetic bandgap backed millimeter-wave MIMO antenna for wearable applications," *IEEE Access*, vol. 7, pp. 111135–111144, 2019.

[26] Y. Sun and K. W. Leung, "Substrate-integrated two-port dual-frequency antenna," *IEEE Trans. Antennas Propag.*, vol. 64, pp. 3692–3697, 2016.

[27] M. S. Sharawi, S. K. Podilchak, M. T. Hussain, and Y. M. M. Antar, "Dielectric resonator-based MIMO antenna system enabling millimetre-wave mobile devices," *IET Microw. Antennas Propag.*, vol. 11, pp. 287–293, 2017.

[28] H. Jiang, L. Si, W. Hu, and X. Lv, "A symmetrical dual-beam bowtie antenna with gain enhancement using metamaterial for 5G MIMO applications," *IEEE Photonics J.*, vol. 11, pp. 1–9, 2019.

[29] M. Khalid, S. Iffat Naqvi, N. Hussain, M. Rahman, Fawad, S. S. Mirjavadi, M. J. Khan, and Y. Amin, "4-port MIMO antenna with defected ground structure for 5G millimeter wave applications," *Electronics*, vol. 9, p. 71, 2020.

[30] R. Anandan, V. V. Kumar, M. P. Maharajan, and G. Jothi, "Dual-beam series-fed MIMO antenna with metasurface loading for 5G sub-6 GHz access point applications," *Applied Computational Electromagnetics Society (ACES) Journal*, vol. 40, no. 10, pp. 1045–1054, Oct. 2025.

[31] Z. Khan, C. Zhang, S. U. Rahman, X.-C. Wang, L. Wen, and W.-Z. Lu, "A low cost, wideband, microstrip patch antenna array with improved gain for millimeter-wave applications," *Applied Computational Electromagnetics Society (ACES) Journal*, vol. 40, no. 10, pp. 1037–1044, Oct. 2025.

Venkatrao Kolli is currently pursuing his Ph.D. in Electronics at Sathyabama Institute of Science and Technology, Chennai, India. His research interests include antenna array design, 5G communication, and wireless communication systems. He has published several research papers in peer-reviewed international journals and conferences in these areas. He is presently working as an Assistant Professor in the Department of Electronics and Communication Engineering at S R K R Engineering College, Bhimavaram. He has guided numerous undergraduate projects related to RF engineering and smart communication systems.

Merlin Sheeba G received her B.E. (Electronics and Communication) degree in 2003 from National Engineering College, Kovilpatti under MS University, India, and M.E. degree in 2005 from Karunya Institute of Science and Technology, Coimbatore under Anna University. She obtained her Ph.D. degree from Sathyabama University, Chennai, in 2017. She has 18 years of teaching and research experience. She is currently working as Professor in the Department of ECE, Jerusalem College of Engineering Chennai. She has published around 45 publications in national and international journals, conferences, and book chapters. Among them, 33 are Scopus indexed, five SCI indexed, and six Web of Science indexed. Her research interests are wireless networks, antennas, IOT and embedded systems. She has published four patents and a sanctioned Government project. She is an invited reviewer in reputable international conferences and journals.

Gain-Focusing Performance Evaluation of Nonlinear Frequency Diverse Arrays

Xin Wang[1], Tao Jiang[1*], Chengkai He[1], and Gengzuo Liu[2]

[1]College of Information and Communication Engineering
Harbin Engineering University, Harbin, 150001, China
wangxin98@hrbeu.edu.cn, jiangtao@hrbeu.edu.cn,
hechengkai@hrbeu.edu.cn
*Corresponding Author

[2]College of Nuclear Science and Technology
Harbin Engineering University, Harbin, 150001, China
liugengzuo@hrbeu.edu.cn

Abstract **–** Nonlinear frequency diverse arrays have attracted increasing attention because of their unique point-like focusing characteristics in the joint angle-range domain. However, the quantitative relationship between the focusing pattern and key design parameters, as well as systematic performance evaluation tools, have not been fully established. In this paper, we propose the gain-focusing area as a quantitative metric for assessing the focusing efficiency of nonlinear frequency diverse arrays (NFDA). Unlike conventional one-dimensional beamwidth measures, the gain-focusing area captures the joint angle-range behavior of the array and provides a basis for performance evaluation and design optimization. Using this metric, we systematically study single- and dual-region focusing, and quantify the influence of focusing location (angle, range) and array design parameters (number of elements, frequency-offset coefficient) on the gain-focusing performance. Numerical simulations demonstrate that the proposed gain-focusing-area based evaluation method provides a more reliable performance metric; compared with existing approaches, it nearly doubles the valid angular range while maintaining accurate characterization of the focusing behavior. This enables NFDA spatial focusing capability and parameter sensitivity to be robustly quantified over a wider field of view, offering a more dependable tool for shaping the electromagnetic environment in and around the target region.

Index Terms **–** Gain-focusing area, nonlinear frequency diverse array, single-point focusing, two-point focusing.

I. INTRODUCTION

In array signal processing, nonlinear frequency diverse arrays (NFDA) achieve two-dimensional beam steering over angle and range, concentrating gain at the prescribed target while decreasing gain as the angular or range offset increases. This behavior enables flexible and highly controllable gain focusing at the target location [1, 2], which is valuable for radar detection and wireless communications because it reduces electromagnetic impact around the target area [3, 4]. By incorporating nonlinear frequency offset coefficients, NFDA mitigates the intrinsic "S-shaped" coupling between angle and range observed in linear frequency diverse arrays, thereby forming focal regions at specific spatial locations [5–8]. A variety of optimization approaches, genetic, artificial bee colony, and mayfly algorithms, have been employed to tune these coefficients and obtain narrower beam widths with reduced peak sidelobe ratios [9–15].

Among the existing studies, [16] provides a representative analysis related to NFDA focusing behavior. However, its analytical derivation is established under the approximation conditions specified in that work and is mainly oriented to a THz near-field scenario. In contrast, the present work considers a beampattern-based geometric evaluation framework for far-field NFDA gain focusing.

To address this gap, this paper introduces the gain-focusing area as a quantitative metric for far-field NFDA focusing in the joint angle-range domain, and further establishes a corresponding geometric calculation framework for its extraction and evaluation.

Submitted On: December 03, 2025
Accepted On: May 04, 2026

https://doi.org/10.13052/2026.ACES.J.410408

Based on -3 dB boundary extraction and equivalent tilted-ellipse characterization, the proposed framework enables reproducible computation of S_{focus}, BW_{theta} and BW_{range}. Using this framework, we study both single-point and two-point gain focusing and systematically quantify the effects of target location and array design parameters.

II. GAIN-FOCUSING AREA DEFINITION AND CALCULATION FRAMEWORK

In contrast to traditional phased arrays, NFDAs can focus the gain not only in the angular dimension but also in the range dimension, thereby exhibiting inherently two-dimensional gain-focusing behavior. To characterize this behavior in a quantitative and reproducible manner, this work not only defines the gain-focusing area as a performance metric, but also establishes a geometric calculation framework for its extraction in the angle-range plane. Specifically, the proposed framework identifies the -3 dB focusing boundary from the far-field NFDA beampattern, constructs an equivalent tilted elliptical focusing region, and computes its area as S_{focus}.

In this work, the two-dimensional gain-focusing area is calculated directly from the NFDA far-field beampattern in the joint angle-range domain. The proposed approach is based on -3 dB boundary extraction and geometric characterization of the focusing region, and therefore does not rely on a specific closed-form analytical approximation. For reference, [16] considers a different derivation route under its own approximation conditions.

Let $B(r,\theta;f(m))$ denote the normalized NFDA beampattern in the selected angle-range observation plane, where r and θ represent the range and angular coordinates in that plane, respectively, $f(m)$ denotes the transmit frequency corresponding to the m-th array element, and m is the element index. Since the present work focuses on a two-dimensional gain-focusing analysis for a linear NFDA in the chosen observation plane, the out-of-plane angular variable ϕ is not introduced in the current formulation. Its maximum at the target location (r_0,θ_0) is

$$B_{max} = B(r_0,\theta_0;f(m)), \tag{1}$$

where $f(m) = f_0 + \Delta f_m, m = 0,1,\ldots M-1$, f_0 is the reference carrier frequency and Δf_m is the nonlinear frequency offset of the m-th element.

The gain-focusing region is then defined as

$$\Omega_{focus} = \{(r,\theta)|B(r,\theta;f(m)) \geq B_{\max}/2\}, \tag{2}$$

and the gain-focusing area is defined as the geometric area of this region,

$$S_{focus} = Area(\Omega_{focus}). \tag{3}$$

In computation, $B(r,\theta;f(m))$ is evaluated on a discrete angle-range grid, and all points satisfying (2) are extracted as the -3 dB gain-focusing region. S_{focus} is then estimated from this region using the geometric procedure in Fig. 2. Under the considered settings, S_{focus} is mainly influenced by the target position, frequency-offset coefficient, and array size.

Equations (1)–(3) define the gain-focusing area metric, whereas the practical computation of S_{focus} is carried out through the calculation framework summarized in Fig. 1 and detailed in Steps (1)–(6). Under the NFDA configuration considered in this paper, the size of S_{focus} is primarily governed by the target position, the frequency-offset coefficient, and the number of array elements.

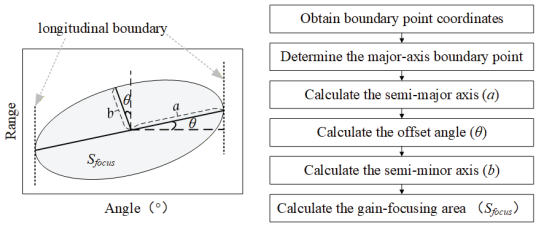

Fig. 1. Flowchart of the proposed gain-focusing area calculation framework and the specific calculation steps.

For the configurations considered here, the -3 dB region is well approximated by a tilted ellipse [16]. Therefore, S_{focus} is obtained by determining the semi-major axis, semi-minor axis, and offset angle of the equivalent ellipse from the boundary points, following Steps (1)–(6) in Fig. 1.

(1) Extract the -3 dB boundary points from the simulated beampattern in the angle-range plane.

(2) Determine the major-axis boundary point by finding the boundary point with the largest angular extent and its range coordinate.

(3) Calculate the semi-major axis a and the offset angle θ from the target point and the major-axis boundary point.

(4) Determine the short-axis boundary point from the target coordinates and the offset angle θ.

(5) Calculate the semi-minor axis b from the target point and the short-axis boundary point.

(6) Compute S_{focus} from the semi-major axis a and semi-minor axis b.

Based on this definition, S_{focus} is computed from the extracted -3 dB gain-focusing region and then used as a quantitative metric in the subsequent single-point and two-point performance evaluations.

III. SINGLE POINT GAIN-FOCUSING PERFORMANCE ANALYSIS

To investigate the focusing performance of NFDAs, we examine the factors influencing S_{focus} from two perspectives.

A. The influence of target position on gain-focusing area

The changes in gain-focusing area are examined by independently varying the target position along the angle and range dimensions. To assess the impact of these parameters, we simulate NFDA patterns for targets at a fixed range with different angles and at a fixed angle with different ranges. Figure 2 depicts, for both cases, the NFDA focusing points together with each point's S_{focus} and 3 dB widths—BW_{theta} (horizontal) and BW_{range} (vertical). Note that Fig. 2 does not display the numerical values of the angular offsets; it only visualizes the focusing points and widths. The corresponding quantitative data, including BW_{theta}, BW_{range}, and S_{focus} for each target position, are provided in Table 1.

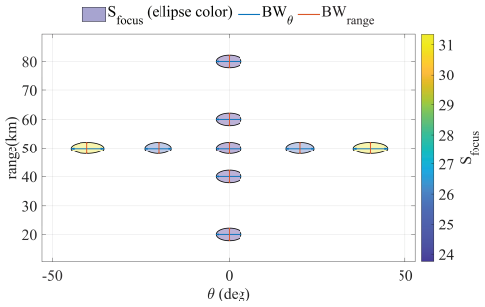

Fig. 2. Impact of target position on gain-focusing area.

As shown in Fig. 2 and Table 1, varying the target range while keeping the angle fixed leaves S_{focus}, BW_{theta}, and BW_{range} almost unchanged, indicating that, in our simulations, the target range has little influence on the gain-focusing performance. In contrast, as observed in Fig. 2 and the corresponding data in Table 1, varying the target position at a fixed range but different angles results in a minimum S_{focus} when the target is aligned with the array's normal direction. Similarly, from a one-dimensional perspective, BW_{range} remains constant, while BW_{theta} is minimized when there is no angular offset between the target and the array, indicating that gain-focusing width in the angle dimension is minimized at this position.

The numerical variation trends of S_{focus}, BW_{theta} and BW_{range} with respect to target angle are consistent with the expected focusing behavior, which also supports the validity of the proposed evaluation framework. As a representative reference, [16] reports similar variation tendencies under its own assumptions. However, since the present method is based on direct geometric extraction from the obtained beampattern, it can be applied in the far-field NFDA configurations considered here over a wider angular range.

B. Impact of array parameters on gain-focusing area

From equations (1)–(3), S_{focus} depends on the underlying beampattern $B(r,\theta;f(m))$, which in turn is determined by the array size and the frequency-offset coefficient. We therefore numerically examine in this

Table 1: BW_{theta}, BW_{range} and S_{focus} for different target positions

Focus Target Positions	BW_{theta}	BW_{range}	S_{focus} of Ours	S_{focus} of [14]
(0°, 80 km)	7.3	4.3	23.7596	316.4782
(0°, 20 km)	7.3	4.3	23.7596	316.4782
(0°, 50 km)	7.3	4.3	23.7596	316.4782
(−10°, 50 km)	7.5	4.3	24.4191	377.1766
(10°, 50 km)	7.5	4.3	24.4191	377.1766
(−20°, 50 km)	7.8	4.3	25.4083	775.5258
(20°, 50 km)	7.8	4.3	25.4083	775.5258
(−30°, 50 km)	8.5	4.3	27.7167	2.0517e3
(30°, 50 km)	8.5	4.3	27.7167	2.0517e3
(−40°, 50 km)	9.6	4.3	31.3413	474.5241
(40°, 50 km)	9.6	4.3	31.3413	474.5241
(−50°, 50 km)	11.6	4.3	37.9405	327.9682
(50°, 50 km)	11.6	4.3	37.9405	327.9682
(−60°, 50 km)	15.1	4.3	49.4845	332.2909
(60°, 50 km)	15.1	4.3	49.4845	332.2909

section, we vary these parameters and examine the changes in gain-focusing width in the angle and range dimensions. Figure 3 shows how NFDA S_{focus}, BW_{theta}, and BW_{range} vary under different array sizes and frequency offset coefficients, and provides the corresponding values of S_{focus}, BW_{theta}, and BW_{range}.

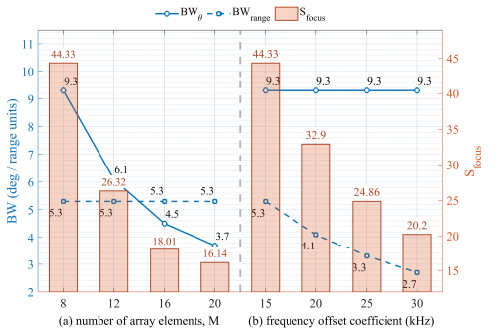

Fig. 3. Impact of array parameters on gain-focusing area.

As shown in Fig. 3 (according to the data therein), S_{focus} decreases as the number of array elements increases, indicating that more elements yield a smaller gain-focusing area. In parallel, the angular gain-focusing width BW_{theta} exhibits a substantial reduction, whereas the range-dimension width BW_{range} remains nearly invariant, suggesting that the element number primarily affects the angular width. According to Fig. 3, S_{focus} also decreases as the frequency-offset coefficient increases. At the target position, BW_{theta} remains essentially constant, while BW_{range} decreases significantly, implying that a larger frequency-offset coefficient produces a narrower range-dimension focusing width and a more concentrated focus.

In conclusion, for the far-field configurations considered here, the target range has a negligible influence on S_{focus}. In contrast, the target angle and the array design parameters (number of elements and frequency-offset coefficient) strongly affect the gain-focusing area and its one-dimensional widths. The angle parameters of the target position affect the gain-focusing area, with the minimum gain-focusing area occurring when the target is aligned with the normal direction of the array. Additionally, for NFDA, an increase in the number of array elements or the frequency offset coefficient results in a reduction in the gain-focusing area. From a one-dimensional perspective, the range parameters do not affect either BW_{theta} or BW_{range}. In contrast, the angle of the target and the number of elements primarily affect BW_{theta}, with negligible influence on BW_{range} in the considered configurations, whereas the frequency-offset coefficient mainly affects BW_{range}, with BW_{theta} remaining nearly unchanged. Thus, the gain-focusing area is primarily governed by the angular position and array design parameters, while the effect of target range on S_{focus} is negligible in the far-field configurations examined.

Furthermore, simulation results show that NFDA forms a focused gain-focusing area solely at the target position, with a controllable gain-focusing area. The array gain outside this area remains low, suggesting that, in the considered scenarios, NFDA-based focusing may help reduce the electromagnetic impact around the target region compared with conventional beamforming.

IV. TWO POINT GAIN-FOCUSING PERFORMANCE ANALYSIS

Assuming the target positions are set at (−40°, 60 km) and (50°, 30 km), the simulation results indicate that NFDA can generate two distinct gain-focusing areas with controllable positions, as shown in Fig. 4.

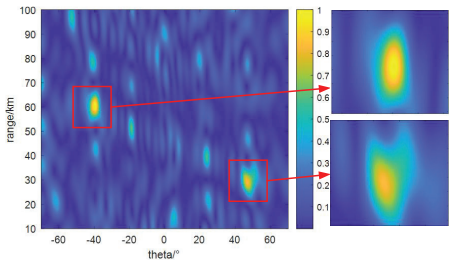

Fig. 4. NFDA beam pattern.

To further analyze the two-point gain-focusing performance of NFDA, simulations were conducted to examine the changes in S_{focus} within each focusing area under varying conditions, such as changes in target positions and modifications to array parameters.

A. Impact of changes in target position on gain-focusing area

Alterations in the gain-focusing area of the two focusing regions are examined by varying the range and angle of the target positions. Table 2 reports simulations for both cases, targets with identical angles but different ranges, and targets with identical ranges but different angles.

Table 2: S_{focus} for two-target configurations

	Target Location	S_{focus}	Target Location	S_{focus}
A	(20°, 15 km)	3.57	(20°, 60 km)	10.94
B	(20°, 20 km)	8.22	(20°, 70 km)	8.24
C	(−30°, 15 km)	3.83	(−30°, 60 km)	12.02
D	(−30°, 20 km)	8.80	(−30°, 70 km)	9.12

Four representative two-target configurations (A–D) are considered, as summarized in Table 2.

In either case the simulated gain-focusing areas successfully encompass both target positions. Cases A/B and cases C/D correspond to two targets sharing the same angle but different ranges, whereas cases A/C and cases B/D correspond to two targets sharing the same range but different angles. According to the data in Table 2, changing either the angle or the range modifies each focusing area. For the limited configurations examined, these variations do not follow a simple monotonic trend, suggesting that the two-point focusing behavior is jointly shaped by the relative positions of the two targets and the NFDA design parameters.

B. Impact of variations in array parameters on gain-focusing area

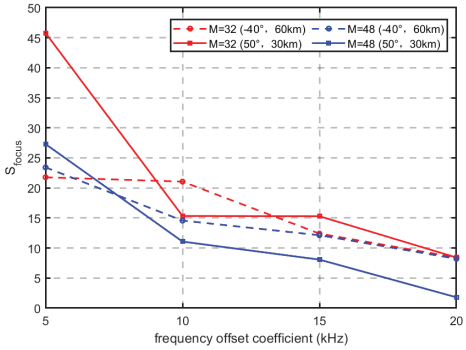

Fig. 5. S_{focus} of each focusing region.

As shown in Fig. 5, the gain-focusing area in each region decreases as the number of array elements increases, consistent with single-point focusing. Notably, although both regions shrink, the focusing area at $(-40°, 60\text{ km})$ remains consistently smaller than that at $(50°, 30\text{ km})$. Likewise, Fig. 5 shows that as the frequency offset coefficient increases, the gain-focusing area of each focusing region gradually decreases, again aligning with single-point NFDA behavior; however, the two areas remain unequal.

These findings indicate that the nonlinear frequency diverse array can realize two-point gain-focusing for targets at different positions. By increasing the number of array elements or adjusting the frequency offset coefficient, the gain-focusing area can be reduced so that array gain concentrates on the targets while the electromagnetic influence outside the focus is strongly attenuated.

V. CONCLUSION

This paper addresses the characterization of NFDA gain-focusing by introducing the gain-focusing area as an effective quantitative metric for point-like focusing. Using this metric, we analyze one- and two-region gain-focusing and quantify the effects of focusing location (angle, range) and design parameters (number of array elements, frequency offset coefficient). Numerical simulations confirm the spatial localization capability, parameter sensitivity, and the improved reliability of the proposed metric; compared with existing approaches, it nearly doubles the valid angular range while maintaining accurate characterization of the focusing behavior. Guided by this metric, NFDAs can be tuned to meet specific requirements, allowing gain-focusing regions to cover target locations accurately over a wider field of view. This adaptability is promising for applications such as fixed-point communications and the mitigation of electromagnetic radiation hazards.

ACKNOWLEDGMENT

This work is supported by the Key Laboratory of Advanced Marine Communication and Information Technology, Ministry of Industry and Information Technology, Harbin Engineering University, Harbin, China.

REFERENCES

[1] P. Antonik, M. Wicks, H. Griffiths, and C. J. Baker, "Frequency diverse array radars," *2006 IEEE Conference on Radar*, p. 3, 2006.

[2] G. H. Zeng, Y. Liao, J. Wang, and Y. C. Liang, "Design of a chaotic index modulation aided frequency diverse array scheme for directional modulation," *IEEE Transactions on Vehicular Technology*, vol. 72, no. 8, pp. 10965–10970, 2023.

[3] Y. Mo, X. J. Xi, L. Chen, W. J. Wu, and D. D. Wang, "Analysis of influence of FSS radome on array antenna scanning," *Chinese Journal of Ship Research*, vol. 15, no. 2, pp. 31–35, 2020.

[4] M. Xiao, T. Hu, X. Shao, L. Wu, and Z. Xiao, "A single-snapshot robust beamforming for FDA-MIMO radar based on AID3," *IEEE Transactions on Vehicular Technology*, vol. 74, no. 1, pp. 38–49, 2025.

[5] W. Khan, I. M. Qureshi, A. Basit, and B. Shoaib, "Transmit/received beamforming for MIMO log-frequency diverse array radar," in *2016 13th International Bhurban Conference on Applied Sciences and Technology (IBCAST)*, pp. 689–693, 2016.

[6] X. Wang and T. Jiang, "Research on nonlinear UAV airborne frequency diverse array radar," in *2023 International Conference on Microwave and Millimeter Wave Technology (ICMMT)*, pp. 1–3, 2023.

[7] H. Shao, J. Dai, J. Xiong, H. Chen, and W. Q. Wang, "Dot-shaped range-angle beampattern synthesis for frequency diverse array," *IEEE Antennas and Wireless Propagation Letters*, vol. 15, pp. 1703–1706, 2016.

[8] Y. Ma, P. Wei, H. Zhang, and H. Liao, "A novel non-optimized method to synthesize dot-shaped

range-angle beampattern for FDA," in *2018 IEEE Radar Conference (RadarConf18)*, pp. 0781–0785, 2018.

[9] C. Cui, X. Ye, W. Li, and X. Shi, "Decoupled range-angle beampattern synthesis of frequency diverse array using genetic algorithm," in *2017 Sixth Asia-Pacific Conference on Antennas and Propagation (APCAP)*, pp. 1–3, 2017.

[10] I. Aryanian, A. Abdipour, and G. Moradi, "Nonlinear analysis and performance improvement of amplifying aperture coupled reflectarray antenna," *Applied Computational Electromagnetics Society (ACES) Journal*, vol. 31, no. 10, pp. 1164–1169, 2021.

[11] H. S. J. Xiong, W. Q. Wang, and H. Chen, "Frequency diverse array transmit beampattern optimization with genetic algorithm," *IEEE Antennas and Wireless Propagation Letter*, vol. 16, pp. 469–472, 2017.

[12] Z. N. Jiang, Y. Zheng, X. F. Xuan, and N. Y. Nie, "A novel ultra-wideband wide-angle scanning sparse array antenna using genetic algorithm," *Applied Computational Electromagnetics Society (ACES) Journal*, vol. 38, no. 2, pp. 100–108, 2023.

[13] A.M. Yao, W. Wu, and D.G. Fang, "Frequency diverse array antenna using time-modulated optimized frequency offset to obtain time-invariant spatial fine focusing beampattern," *IEEE Transactions on Antennas and Propagation*, vol. 64, no. 10, pp. 4434–4446, 2016.

[14] E. Kurt, S. Basbug, and K. Guney, "Linear antenna array synthesis by modified seagull optimization algorithm," *Applied Computational Electromagnetics Society (ACES) Journal*, vol. 36, no. 22, pp. 1552–1562, 2022.

[15] M. X. Xiao, T. Y. Hu, L. Li, X. L. Shao, J. Y. Zhang, and W. Xue, "Frequency diverse array beampattern synthesis with joint optimization of frequency offset and carrier," in *2022 International Conference on Microwave and Millimeter Wave Technology (ICMMT)*, pp. 1–3, 2022.

[16] L. Li, H. Li, Z. Chen, W. Chen, and S. Li, "An analytical range-angle dependent beam focusing model for terahertz linear antenna array," *IEEE Wireless Communications Letters*, vol. 11, no. 9, pp. 1870–1874, 2022.

Xin Wang was born in 1998. She obtained the B.S. degree from Northeast Electric Power University, Jilin, China, in 2020. She is currently pursuing the Ph.D. degree in information and communication engineering at Harbin Engineering University. Her main research interests include array signal processing.

Tao Jiang (Member, IEEE) received the Ph.D. degree from Harbin Engineering University, Harbin, China, in 2002. Since 1994, he has been a Faculty Member of the College of Information and Communication, Harbin Engineering University, where he is currently a Professor. He was a Postdoctoral Researcher with the Research Institute of Telecommunication, Harbin Institute of Technology, Harbin, from 2002 to 2003, and a Visiting Scholar with the Radar Signal Processing Laboratory, the National University of Singapore, from 2003 to 2004. His current research interests include radio wave propagation, electromagnetic modeling and prediction, and electromagnetic environment.

Chengkai He was born in 2000. He obtained the B.S. degree from Harbin Engineering University, Harbin, China, in 2022. He is currently pursuing a master's degree in Information and Communication Engineering at Harbin Engineering University, with a primary research focus on antennas.

Gengzuo Liu is a second-year Ph.D. student in Nuclear Science and Technology at Harbin Engineering University, China. His research spans radiation detection and protection, nuclear medical physics (FLASH-RT, BNCT), and accelerator beam/beamline design, employing machine learning and multiobjective optimization for fast gamma-ray buildup factor prediction and space-reactor design.

Synthesis and Design of a Wideband Filtering Impedance Transformer and its Application as a Power Divider

Haili Zhang[1,2], Zhenzhong Chen[1], and Taijun Liu[1*]

[1]Faculty of Electrical Engineering and Computer Science
Ningbo University, Ningbo 315210, China
158936225@qq.com, liutaijun@nbu.edu.cn

[2]Institute of IOT Application Technology
Zhejiang Fashion Institute of Technology, Ningbo 315211, China
158936225@qq.com
*Corresponding Author

Abstract – In this paper, two classes of impedance transformers with wide operating bandwidth are presented. The impedance parameters can be directly determined based on the specified impedance transformation ratio, fractional bandwidth (FBW), and in-band return loss (*RL*) requirements. To validate the proposed method, an impedance transformer is designed at the center frequency (f_0) of 2.4 GHz and an impedance-transforming ratio (r) of 0.5. The filtering impedance transformer with FBW $= 90\%$ and $RL = 20$ dB is fabricated and measured, validating the theoretical prediction. Furthermore, to demonstrate its application potential, the second impedance transformer is employed to realize a filtering power divider with wide operating bandwidth and enhanced isolation bandwidth.

Index Terms – Filtering transformer, impedance transformer, isolation bandwidth, synthesis method, wideband power divider.

I. INTRODUCTION

An impedance transformer is a fundamental component in the design of radio frequency (RF) and microwave systems, critical to ensuring maximum power transfer and minimizing signal reflection between components with different characteristic impedances. Conventional impedance matching networks, such as $\lambda/4$ transformers, are widely used because of their simplicity and effectiveness at a single frequency. However, their inherent narrowband characteristics limit their application in modern wideband communication systems, such as 5G and ultra-wideband, where broad bandwidth and a wide range of impedance transformer ratios are increasingly demanded [1–3].

To overcome the bandwidth limitation, multi-section impedance transformers have been proposed [4, 5]. These approaches can achieve wider bandwidth, but these designs typically lack frequency selectivity. Consequently, the integration of filtering response into impedance transformers has emerged as a promising direction, enabling circuits that perform simultaneous impedance transformation and bandpass filtering. For instance, in [6], a broadband impedance transforming network composed of cascaded $\lambda/4$ transmission lines and short-circuited $\lambda/4$ stubs is proposed, achieving an impedance transformation from 50 Ω to 110 Ω with a fractional bandwidth (FBW) of 77.8%. Compared to conventional $\lambda/4$ transmission lines, coupled lines offer additional degrees of freedom for design control, including even-/odd-mode characteristic impedances and loading effects at both the through and coupled ports. This offers greater flexibility in the design of wideband impedance transformers [7, 8]. In summary, although the aforementioned methods significantly expand the bandwidth of impedance transformation networks, the achievable impedance ratio remains constrained by the physical limitations of $\lambda/4$ transmission lines and coupling lines. This results in a relatively low impedance ratio range for practical applications.

To enhance the impedance transformation ratio, various innovative circuit topologies have been proposed. In [9], by controlling the coupling coefficients of the cascaded open-terminated coupled lines, a transformation ratio with two transmission poles is achieved within the passband. This design realizes 5–50 Ω impedance transformation with a bandwidth of 8.27%. In [10], a class of bandpass impedance transformer with an extremely high transformation ratio is proposed using a Π-type tapped feed structure. This transformer achieves an impedance transformation from 5 Ω to 520 Ω with a bandwidth

Submitted On: December 29, 2025
Accepted On: March 18, 2026

https://doi.org/10.13052/2026.ACES.J.410409

of 10%. Furthermore, a class of filtering impedance transformers offering an enhanced transformation ratio is presented in [11], where the core structure comprises two cascaded coupled lines and stubs. The fabricated circuit achieves a $50-500\ \Omega$ impedance transformation with a bandwidth of 22%. In conclusion, the coupled structures can improve the impedance transformation ratio to some extent, but the bandwidth of high-ratio filtering transformers remains limited.

A power divider is another important microwave device, which plays an important role in the antenna feeding network, power amplifier, and RF harvesting system [12–14]. The core design elements are impedance transformers. The performance of an impedance transformation structure design directly impacts the matching property of power dividers. Common types of power dividers include T-type power divider, Wilkinson power divider, and Gysel power divider. The conventional T-type power divider [15], Wilkinson power divider [16–18], and Gysel power divider [19–21] consistently suffer from narrow bandwidth. For example, in [16], a Wilkinson power divider is proposed based on $\lambda/4$ impedance transformer, but its operating bandwidth is only 20%. To increase the bandwidth of the Wilkinson power divider, multisection power dividers based on multiple $\lambda/4$ transmission lines are proposed. Although the operating bandwidth is greatly enhanced, these designs lack filtering performance. To integrate wideband power dividers with filtering functions, researchers focused on multimode resonators [22], quadruple-mode folded substrate integrated waveguides [23], embedded transversal signal-interference sections [24], and anti-parallel coupled line structures [25]. However, these works are unable to provide a synthesis method. In other words, the FBW and return loss (RL) cannot be customized as required.

Recently, a self-packaged wideband bandpass filtering power divider with a constant power division ratio was achieved in [26]. By introducing a synthesis design method based on transmission zero locations and closed-form equations for isolation resistors, the design exhibits excellent wideband performance and high isolation. However, design complexity is relatively high and requires high fabrication precision. In [27], a compact all-port-reflectionless wideband filtering power divider is proposed based on a five-line coupled structure. However, the design relies heavily on optimization due to the lack of closed-form synthesis equations. Therefore, the design of wideband power dividers using synthesis methods based on easy-fabrication impedance transformers remains a challenge.

In this work, we propose two novel classes of impedance transformers based on a synthesis method and utilize it to construct the filtering branches of a wideband power divider. The proposed circuits exhibit designable operating bandwidth and enhanced impedance transformer ratio. The proposed structures generate three and four transmission poles within the passband, resulting in extended bandwidth. Moreover, the circuit parameters can be directly determined from specified design requirements, including impedance transformation ratio, FBW, and in-band RL, significantly simplifying the design process. A wideband impedance transformer based on the first structure is fabricated with FBW of 90%. A second structure is adopted to implement a filtering power divider with wide operating bandwidth and enhanced isolation bandwidth. Simulation and measurement results exhibit excellent agreement.

II. DESIGN OF A WIDEBAND FILTERING IMPEDANCE TRANSFORMER

Figures 1 (a) and (b) show the two topologies of the proposed wideband filtering transformer with two short-circuited stubs. They are three- and four-pole impedance transformers, respectively. To demonstrate the synthesis method, the detailed synthesis procedures of the filtering transformer in Fig. 1 (a) are summarized. The overall $ABCD$ matrix of the filtering transformer is expressed as:

$$\begin{bmatrix} A_1 & B_1 \\ C_1 & D_1 \end{bmatrix} = [M_1][M_{s1}][M_2][M_{s2}], \tag{1}$$

where $[M_1]$ and $[M_2]$ are the $ABCD$ matrix of $\lambda/4$ lines and $[M_{s1}]$ and $[M_{s2}]$ are the $ABCD$ matrix of $\lambda/4$ shunt shortcircuited stubs. Based on the synthesis theory in [28–30], the squared magnitude of the transmission coefficient $|S_{21}|^2$ with port impedances Z_s and Z_L can be derived:

$$|S_{21}|^2 = \frac{1}{1+\left|\frac{2\sqrt{Z_S Z_L}}{A_1 Z_L + B_1 + C_1 Z_S Z_L + D_1 Z_S}\right|^2}. \tag{2}$$

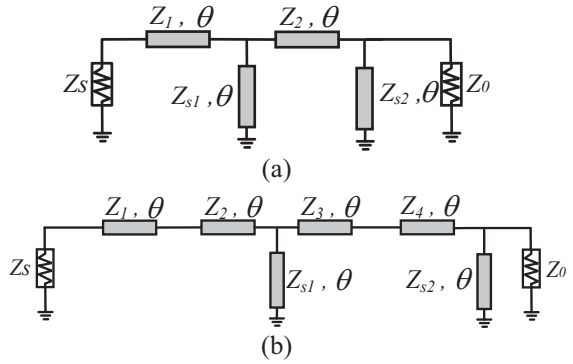

Fig. 1. Topologies of proposed wideband filtering transformers with two $\lambda/4$ short-circuited stubs: (a) three-pole impedance transformer and (b) four-pole impedance transformer.

It is assumed herein that the impedance transforming ratio of the proposed filtering transformer is $r = Z_L/Z_S$. All impedance parameters are normalized by the load impedance Z_L. Thus, the characteristic impedance parameters can be achieved as $z_1 = Z_1/Z_L, z_2 = Z_2/Z_L, y_{s1} = Z_L/Z_{S1}$, and $y_{s2} = Z_L/Z_{S2}$. Equation (2) can be transformed as:

$$|S_{21}|^2 = \frac{1}{1+|F|^2} = \frac{1}{1+\left|\frac{2\sqrt{r}}{A_1+B_1+C_1 r+D_1 r}\right|^2}. \quad (3)$$

Here, the function F can be derived as:

$$F = \frac{j}{2\sqrt{r}z_1 z_2 \sin\theta}\left[k_1\cos^3\theta + k_2\cos\theta\right] + k_3\cos^2\theta + k_4, \quad (4)$$

where:

$$k_1 = (z_0 + z_1 + y_{s1}z_0z_1)(k - z_0z_1 + ry_{s2}z_1), \quad (5a)$$

$$k_2 = (y_{s1}z_0^2z_1^2 + z_0^2z_1 + z_0z_1^2 - rz_0 - ry_{s2}z_1^2 - rz_1), \quad (5b)$$

$$k_3 = (z_0 + z_1 + y_{s1}z_0z_1)(rz_0 - z_1 + ry_{s2}z_0z_1)/2\sqrt{r}z_0z_1, \quad (5c)$$

$$k_4 = (z_1^2 - rz_0^2)/2\sqrt{r}z_0z_1. \quad (5d)$$

The squared magnitude of transmission coefficient $|S_{21}|^2$ can also be mathematically expressed by Chebyshev polynomials as:

$$|S_{21}|^2 = \frac{1}{1+\varepsilon^2\cos^2(n\phi + q\xi)}, \quad (6)$$

and

$$x = \cos\phi = \alpha\cos\theta \quad (7a)$$

$$y = \cos\xi = x\sqrt{\frac{\alpha^2-1}{\alpha^2-x^2}}. \quad (7b)$$

Here ε is the specified equal-ripple constant in the passband and θc is the phase at lower cutoff frequency. Because of the frequency-distribution characteristic of transmission lines, the upper cutoff frequency of this bandpass filter appears at $(180^\circ - \theta c)$. Based on the $RL = 15$ dB relationship among those variables in (7a) and (7b), the cosine function in (6) can be expanded as:

$$\cos(n\varphi + q\xi) = T_n(x)T_q(y) - U_n(x)U_q(y), \quad (8)$$

where $T_n(x)$ and $U_n(x)$ are the Chebyshev polynomial functions of the first and second kinds of degree n. Using the identity for $T_n(x)$ and $U_n(x)$:

$$T_{n+1}(x) - xT_n(x) = -\sqrt{1-x^2}U_n(x). \quad (9)$$

The targeted transfer function in (3) can be analytically expressed in terms of the two kinds of Chebyshev functions. To make (3) have the same response as (6), n and q in equation (6) must be selected as 3 and 1, such that:

$$\varepsilon\cos(3\phi + \xi) = K_1\frac{\cos^3\theta}{\sin\theta} + K_2\frac{\cos\theta}{\sin\theta}, \quad (10)$$

where:

$$K_1 = -\varepsilon(2\sec(\alpha) + \tan(\alpha)), \quad (11a)$$

$$K_2 = 2\varepsilon\sec(\alpha)^2(\sec(\alpha) + \tan(\alpha)). \quad (11b)$$

In (10), ε is the equal-ripple constant in relevance to the specified RL within an operating band and α is the quantity related to the specified FBW such that:

$$\varepsilon = \sqrt{\frac{10^{-RL/10}}{1-10^{-RL/10}}}, \quad (12a)$$

$$\alpha = \frac{1}{\cos(\theta_c)}, \quad (12b)$$

$$\text{FBW} = \frac{\pi - 2\theta_c}{\pi/2}. \quad (12c)$$

By solving $k_1 = K_1, k_2 = K_2$, and $k_3 = k_4 = 0$, the four normalized impedance parameters z_1, z_2, y_{s1}, and y_{s2} are all determined by the specified FBW, RL, and r.

The detailed design procedure is described as follows.

- Determine all the characteristic impedances involved in ideal models of wideband transformer in Fig. 1 (a) with specified FBW and RL using the above-described synthesis method;
- Map the above-derived characteristic impedances and electrical length into their respective initial physical dimensions;
- Execute slight adjustment of the physical dimensions in order to compensate for some unexpected spurious effects in the microstrip-line structure, e.g., frequency dispersion, bend/step discontinuities, and so on.

To demonstrate the feasibility of the bandwidth, Fig. 2 presents the $50-25\ \Omega$ impedance transformers with FBW $= 80-100\%$ and RL of 20 dB. The simulated results show good agreement with the prescribed specifications, validating the synthesis theory. Table 1 presents the impedance parameters of the filtering transformers with FBW of 62%, 70%, 80%, and 106%, impedance transformer ratio r of $6.5, 6, 5.5$, and 2.3, under the condition of $RL = 15$ dB. All the impedance parameters are within the achievable range of microstrip technology.

By using the synthesis method, the structure in Fig. 1 (b) can also be synthesized following the similar

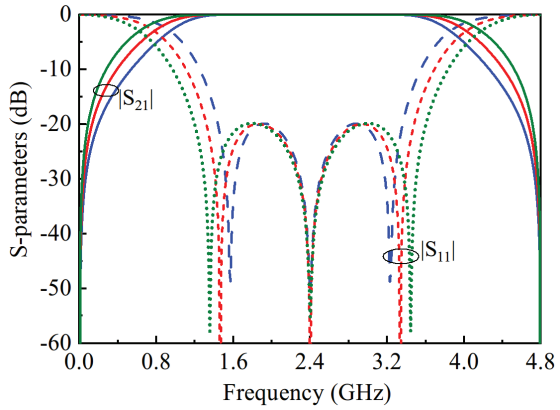

Fig. 2. $50-25\ \Omega$ impedance transformers with FBW $=$ $80-100\%$ and $RL = 20$ dB.

Table 1: Impedance parameters of filtering transformers with FBW of 62%, 70%, 80%, and 106%, impedance transformer ratio r of 6.5, 6, 5.5, and 2.3, under condition of $RL = 15$ dB

r	FBW	Impedance Parameters (Ω)			
		Z_1	Z_2	Z_{S1}	Z_{S2}
6.5	62%	52.2	133.2	33.7	45.4
6	70%	55.5	136.1	38.3	71.1
5.5	80%	59.3	139.2	44.1	133.7
2.3	106%	47.4	72.0	91.9	140.8

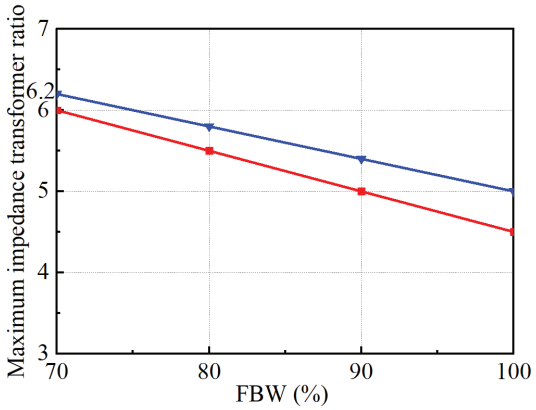

Fig. 3. Maximum available impedance transformer ratio of proposed structure in Figs. 1 (a) and (b), under condition of RL of 15 dB.

design procedures in [31, 32]. Figure 3 presents the maximum available filtering impedance transformer ratio of the proposed structure in Figs. 1 (a) and (b), under the condition of $RL = 15$ dB. It can be observed that as the FBW increases, the maximum achievable impedance transformation ratio decreases. Regarding the structure in Fig. 1 (a), when the FBWs are selected as 70%, 80%, 90%, and 100%, the maximum achievable impedance

Table 2: Impedance parameters of filtering transformers with FBW of 100%, transformer ratio r of 2-5, under condition of $RL = 15$ dB

r	FBW	Impedance Parameters (Ω)					
		Z_1	Z_2	Z_3	Z_4	Z_{S1}	Z_{S2}
2	100%	56.5	21.1	18.9	35.9	8.5	132.5
3	100%	84.7	31.6	26.3	40.8	13.2	91.8
4	100%	113	42.1	33.1	44.4	18.2	77.6
5	100%	141.3	52.7	39.4	47.3	23.3	70.1

transformation ratios are 6, 5.5, 5, and 4.5. Regarding structure in Fig. 1 (b), when the FBWs are selected as 70%, 80%, 90%, and 100%, the maximum achievable impedance transformation ratios are 6.2, 5.8, 5.4, and 5. Table 2 summarizes the impedance parameters of the filtering transformers with FBW of 100%, impedance transformer ratio r of 2–5, under condition of $RL = 15$ dB. As the impedance ratio r increases, the impedance Z_1, Z_2, Z_3, Z_4, and Z_{s1} increases while the impedance Z_{s2} decreases. Generally, the available impedance is lower than 150 Ω, thus the maximum available impedance transformer ratio is 5 when the FBW is chosen as 100%.

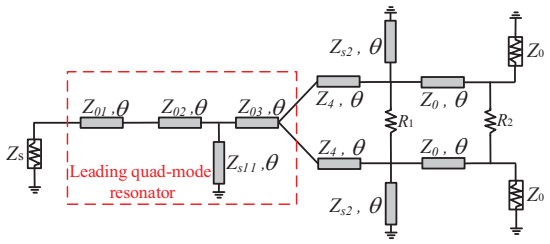

Fig. 4. Proposed wideband filtering power divider with leading quad-mode resonator.

Figure 4 shows the schematic of the proposed wideband filtering power divider with leading quad-mode resonator. The leading part introduces four poles and jointly realizes five-pole Chebyshev response. The isolation response also has four approximate matching points. Attributing to the leading quad-mode resonator, wide operating bandwidth and isolation bandwidth are both achieved. As shown in Fig. 4, isolation resistors R_1 and R_2 are added between the two filtering branches. To demonstrate the function of the isolation resistor, theoretical results of the proposed wideband filtering transformer are designed and simulated. The wideband power divider with center frequency of 2.4 GHz, FBW $=$ 100%, and $RL = 15$ dB is simulated with one isolation resistor and two isolation resistors. The circuit parameters in Fig. 4 are $Z_{01} = 28.2\ \Omega$, $Z_{02} = 10.5\ \Omega$, $Z_{03} = 9.5\ \Omega$, $Z_4 = 35.9\ \Omega$, $Z_{s11} = 4.2\ \Omega$, and $Z_{s2} = 132.5\ \Omega$.

By trading off the matching property and isolation performance, the values of the isolation resistors can be selected. Figure 5 illustrates the theoretical results of the proposed wideband filtering transformer with one isolation resistor $R_1 = 47\ \Omega$, under condition of *RL* bandwidth of 100% and *RL* of 15 dB. The five-pole Chebyshev response has been well achieved. Unfortunately, the responses of $|S_{22}|, |S_{33}|, |S_{32}|$ are degraded. To solve the problem, an additional resistor R_2 is introduced as 130 Ω, good matching property of $|S_{11}|, |S_{22}|, |S_{33}|$, and $|S_{32}|$ are realized, as shown in Fig. 6. The fully matching bandwidth and the isolation bandwidth are both 100%.

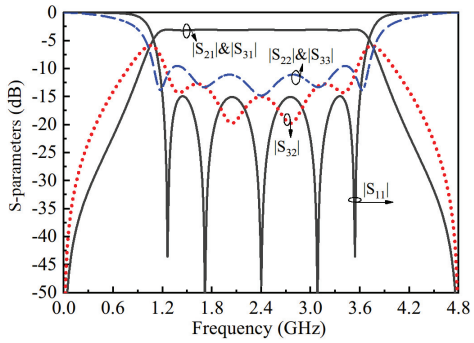

Fig. 5. Theoretical results of proposed wideband filtering transformer with one isolation resistor R_1, under condition of bandwidth of 100% and *RL* of 15 dB.

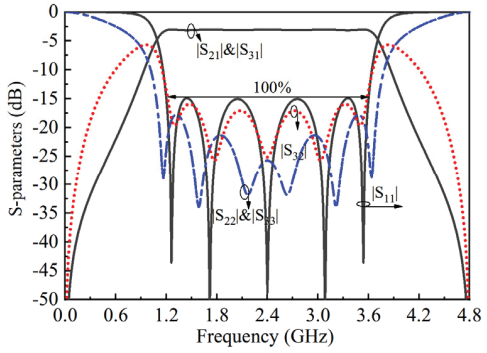

Fig. 6. Theoretical results of proposed wideband filtering transformer with two isolation resistors R_1 and R_2, under condition of bandwidth of 100% and *RL* of 15 dB.

III. SIMULATION AND EXPERIMENT

For verification, a wideband impedance transformer with center frequency of 2.4 GHz, $r = 0.5$, FBW = 90%, and *RL* = 20 dB is designed, simulated in ADS software, and fabricated on RO4003C substrate with relative permittivity of 3.55 and thickness of 0.508 mm. The impedance parameters are $Z_1 = 33.6\Omega, Z_2 = 23.7\Omega, Z_{s1} = 44.9\ \Omega$, and $Z_{s2} = 57.3\ \Omega$. As such, the strip widths and lengths of the two short-circuited microstrip-line stubs are determined as: $W_{S1} = 1.34$, $L_{S1} = 19.69, W_{S2} = 0.9$, and $L_{S2} = 19.85$. The strip widths and lengths of the two microstrip-line sections in the middle are equal to: $W_1 = 2.16, L_1 = 18.74, W_2 = 3.22$, and $L_2 = 18.39$ (unit: mm). The photograph of the fabricated wideband filtering impedance transformer is shown in Fig. 7. During measurement, the TRL calibration procedure is applied to calibrate out the effects of the SMA connectors and feeding microstrip lines. The scattering parameters are measured between the two 50 Ω ports and referenced to a 50 Ω source and a 25 Ω load impedance. As illustrated in Fig. 8, the measured center frequency, *RL* bandwidth, maximal *RL*, and minimal insertion loss are 2.41 GHz, 100%, 16.1 dB, and 0.3 dB, respectively. The $15-$dB *RL* bandwidth is from 1.2 to 3.62 GHz. The simulated and measured results show close agreement, validating the design's effectiveness.

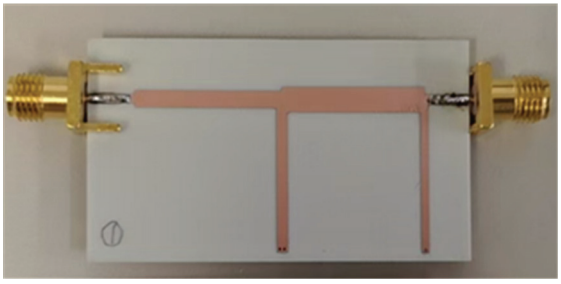

Fig. 7. Photograph of filtering impedance transformer in Fig. 1 (a).

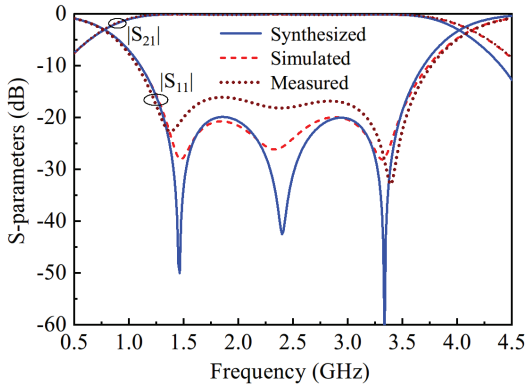

Fig. 8. Simulated and measured results of designed filtering transformer circuit in Fig. 1 (a).

To verify the proposed method, a wideband power divider shown in Fig. 4 with FBW = 100% and *RL* = 15 dB is designed, simulated in ADS software, and fabricated on RO4003C substrate with relative permittivity of 3.55 and thickness of 0.305 mm. Figures 9

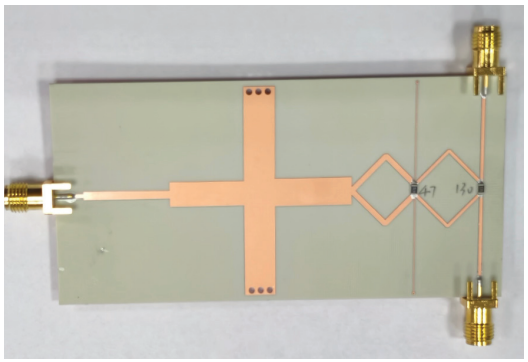

Fig. 9. Photograph of wideband power divider in Fig. 4.

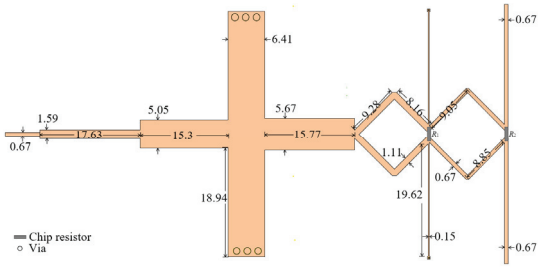

Fig. 10. Dimensions of proposed power divider.

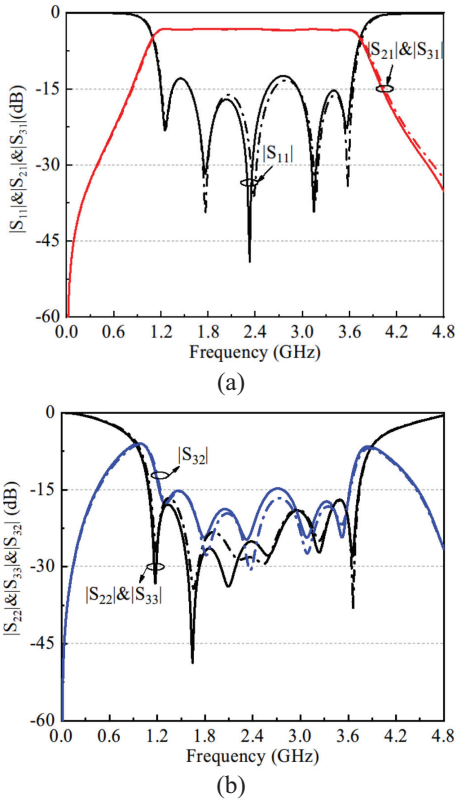

Fig. 11. Simulated and measured S-parameters of proposed wideband filtering power divider: (a) magnitude response of $|S_{11}|, |S_{21}|$, and $|S_{31}|$ and (b) magnitude response of $|S_{22}|, |S_{33}|$, and $|S_{32}|$.

and 10 show the photograph and physical layout of the fabricated wideband power divider. Figure 11 presents the simulated and measured S-parameters of the proposed wideband filtering power divider. Figure 11 (a) shows the simulated and measured magnitude response of $|S_{11}|, |S_{21}|$, and $|S_{31}|$ of the proposed wideband power divider. The simulated operating band range is 1.18–3.65 GHz with 12 dB input *RL* bandwidth of 102.2%, and the measured operating band is 1.18–3.66 GHz with 13 dB input *RL* bandwidth of 102.4%. The measured magnitude curve of $|S_{21}|$ and $|S_{31}|$ range from -3.34 dB to -3.16 dB across the bandwidth. In this frequency range, the measured in-band minimal *RL* is -13.3 dB and the simulated one is -12.4 dB, respectively. Figure 11 (b) presents the isolation performance $|S_{32}|$ and matching property $|S_{22}|$ and $|S_{33}|$. Within the passband, the simulated and measured in-band isolation $|S_{32}|$ achieves better than -14.7 dB and -15.3 dB, respectively. The measured isolation bandwidth is better than -15 dB, and the simulated isolation bandwidth is better than -14 dB, both achieving 100%. Moreover, the simulated and measured magnitudes of $|S_{22}|$ and $|S_{33}|$ are with corresponding -15 dB bandwidths of 109.7%. The simulated and measured S-parameters of the designed power divider is in good agreement with the theoretical results shown in Fig. 6. The experimental results of the design example have validated the effectiveness of the design method.

Table 3: Comparison of proposed power divider and recently published works

Ref.	Freq. (GHz)	FBW	Filtering Implanted	Isolation Bandwidth
25	3.54	17.3%	yes	17.3% (-25 dB)
16	0.5	20%	no	20% (-20 dB)
17	1	27%	no	63% (-20 dB)
20	2	65%	no	65% (-15 dB)
26	2.35	70%	yes	70% (-24 dB)
27	1.8	73%	yes	73% (-18.5 dB)
22	2.5	78%	yes	78% (-17 dB)
This Work	2.4	102%	yes	100% (-14 dB)

Table 3 tabulates the comparison of proposed power divider and recently published works. The classic Wilkinson power divider in [16] exhibits a limited bandwidth. The modified Wilkinson power divider in [17] enhances the isolation bandwidth, but its operational bandwidth remains constrained. The modified Gysel power divider in [20] achieves broader bandwidth. However, the references in [16, 17, 20] all lack integrated filtering functionality. In contrast to the filtering power divider reported in [25–27], the proposed design shows

superior performance in both matching and isolation bandwidths. Furthermore, our work is guided by a systematic synthesis procedure that allows direct circuit derivation from stated specifications.

IV. CONCLUSION

This paper has proposed two novel classes of wideband filtering impedance transformers with designable operating bandwidth and enhanced impedance transformation ratio, addressing the limitations of existing designs that lack systematic synthesis methods or suffer from narrow bandwidth. The proposed topologies generate multiple transmission poles within the passband, achieving wider bandwidth and enhanced impedance transformation ratios. The proposed synthesis method enables direct and systematic design of impedance transformers with specified bandwidth, *RL*, and transformation ratio, which significantly enhances design flexibility for practical RF front-end modules. To validate this approach, a wideband filtering transformer with 90% fractional bandwidth, impedance ratio of $r = 0.5$, and 20-dB *RL* is designed, simulated, and measured. In addition, a wideband power divider based on the proposed filtering transformer is implemented, demonstrating good filtering and isolation performance. Future research will extend the proposed synthesis method to develop tunable or reconfigurable impedance transformers for multiband matching, and to integrate them into multifunctional circuits such as balanced-to-unbalanced filtering networks or Doherty power amplifiers, where wideband impedance transformation is required.

ACKNOWLEDGMENT

This work was supported in part by the Zhejiang Provincial Natural Science Foundation of China under Grant LQN26F010015.

REFERENCES

[1] S. Chen, G. Zhao, M. Tang, and Y. Yu, "Wideband filtering impedance transformer based on transversal interaction concept," *Electron. Lett.*, vol. 54, no. 6, pp. 368–370, Oct. 2018.

[2] P. Kim, G. Chaudhary, and Y. Jeong, "Wideband impedance transformer with out-of-band suppression characteristics," *Microw. Opt. Technol. Lett.*, vol. 56, no. 11, pp. 2612–2616, June 2014.

[3] X. Wang, Z. Ma, T. Xie, M. Ohira, C.-P. Chen, and G. Lu, "Synthesis theory of ultra-wideband bandpass transformer and its Wilkinson power divider application with perfect in-band reflection/isolation," *IEEE Trans. Microw. Theory Techn.*, vol. 67, no. 8, pp. 3377–3390, Aug. 2019.

[4] M. Chongcheawchamnan, S. Patisang, S. Srisathit, R. Phromloungsri, and S. Bunnjaweht, "Analysis and design of a three-section transmission-line transformer," *IEEE Trans. Microw. Theory Techn.*, vol. 53, no. 7, pp. 2458–2462, July 2005.

[5] R. Darraji, M. M. Honari, R. Mirzavand, F. M. Ghannouchi, and P. Mouavi, "Wideband two-section impedance transformer with flat real-to-real impedance matching," *IEEE Microw. Wireless Compon. Lett.*, vol. 26, no. 5, pp. 313–315, May 2016.

[6] Q. Wu and L. Zhu, "Wideband impedance transformers on parallel-coupled and multisection microstrip lines: Synthesis design and implementation," *IEEE Trans. Compon. Packag. Manuf. Technol.*, vol. 6, no. 12, pp. 1873–1880, Dec. 2016.

[7] Q. Wu and L. Zhu, "Wideband impedance transformers with good frequency selectivity based on multisection quarter-wave lines and short-circuited stubs," *IEEE Microw. Wireless Compon. Lett.*, vol. 26, no. 5, pp. 337–339, May 2016.

[8] Q. Wu and L. Zhu, "Synthesis design of a wideband impedance transformer consisting of two-section coupled lines," *IET Microw. Antennas Propag.*, vol. 11, no. 1, pp. 144–150, July 2017.

[9] P. Kim, G. Chaudhary, and Y. Jeong, "Ultra-high transforming ratio coupled line impedance transformer with bandpass response," *IEEE Microw. Wireless Compon. Lett.*, vol. 25, no. 7, pp. 445–447, July 2017.

[10] C. W. Hsieh, S. C. Lin, and J. Y. Li, "Bandpass impedance transformers with extremely high transforming ratios using Π-tapped feeds," *IEEE Access*, vol. 6, pp. 28193–28202, June 2018.

[11] Z. Zhuang, Y. Wu, M. Kong, and W. Wang, "High-selectivity single-ended/balanced DC-block filtering impedance transformer and its application on power amplifier," *IEEE Trans. Circuits Syst. I, Reg. Papers*, vol. 67, no. 12, pp. 4360–4369, Dec. 2017.

[12] F. Liu, K. Fan, X. Zhang, Q. Tan, X. Zhang, and L. Liu, "A millimeter-wave wideband low-sidelobe slotted antenna array based on a high power divider ratio microstrip ridge gap waveguide feed network," *IEEE Antennas Wireless Propag. Lett.*, vol. 24, no. 12, pp. 4780–4784, Dec. 2025.

[13] S. Y. Zheng, Z. W. Liu, Y. M. Pan, Y. Wu, W. S. Chan, and Y. Liu, "Bandpass filtering Doherty power amplifier with enhanced efficiency and wideband harmonic suppression," *IEEE Trans. Circuits Syst. I, Reg. Papers*, vol. 63, no. 3, pp. 337–346, Mar. 2016.

[14] O. Kasar, M. Kahriman, and M. A. Gozel, "Application of ultra wideband RF energy harvesting by using multisection Wilkinson power combiner," *Int. J. RF Microw. Comput.-Aided Eng.*, vol. 29, no. 1, pp. 1–8, 2019.

[15] D. M. Pozar, *Microwave Engineering*, 3rd ed. New York: Wiley, 2005.

[16] E. Wilkinson, "An N-way hybrid power divider," *IEEE Trans. Microw. Theory Tech.*, vol. 8, no. 1, pp. 116–118, Jan. 1960.

[17] R. Mirzavand, M. M. Honari, A. Abdipour, and G. Mordi, "Compact microstrip Wilkinson power dividers with harmonic suppression and arbitrary power division ratios," *IEEE Trans. Microw. Theory Techn.*, vol. 61, no. 1, pp. 61–68, Jan. 2013.

[18] C. Bao, X. Wang, Z. Ma, C.-P. Chen, and G. Lu, "An optimization algorithm in ultrawideband bandpass Wilkinson power divider for controllable equal-ripple level," *IEEE Microw. Wireless Compon. Lett.*, vol. 30, no. 9, pp. 861–864, Sep. 2020.

[19] S. Kouhpayeh-Zadeh-Esfahani, K. Afrooz, and E. Moradi, "A 10:1 unequal Gysel power divider/combiner," *Microw. Opt. Technol. Lett.*, vol. 58, no. 11, pp. 2689–2692, Aug. 2016.

[20] X. Wang, K.-L. Wu, and W.-Y. Yin, "A compact Gysel power divider with unequal power-dividing ratio using one resistor," *IEEE Trans. Microw. Theory Techn.*, vol. 62, no. 7, pp. 1480–1486, July 2014.

[21] H. Chen, Y. Zhou, T. Zhang, W. Che, and Q. Xue, "N-way Gysel power divider with arbitrary power-dividing ratio," *IEEE Trans. Microw. Theory Techn.*, vol. 67, no. 2, pp. 659–669, Feb. 2019.

[22] Y. Liu, L. Zhu, and S. Sun, "Proposal and design of a power divider with wideband power division and port-to-port isolation: A new topology," *IEEE Trans. Microw. Theory Techn.*, vol. 68, no. 4, pp. 1431–1438, Dec. 2019.

[23] B.-G. Liu, J.-C. Pu, H. Tang, Y. Cheng, and C.-H. Cheng, "Compact quadruple-mode FSIW filtering power divider with high isolation using embedded capacitive isolation network," *IEEE Trans. Circuits Syst. II, Exp. Briefs*, vol. 71, no. 8, pp. 3750–3754, Aug. 2024.

[24] L. Jiao, Y. Wu, Y. Liu, Q. Xue, and Z. Ghassemlooy, "Wideband filtering power divider with embedded transversal signal-interference sections," *IEEE Microw. Wireless Compon. Lett.*, vol. 27, no. 12, pp. 1068–1070, Dec. 2017.

[25] D. Li, L. Zhang, J. Wang, Y. Liu, and Q. Chen, "Characteristic analysis of parallel and anti-parallel coupled line structures and their integrated design in filtering power dividers," *IEEE Trans. Compon. Packag. Manuf. Technol.*, vol. 13, no. 11, pp. 1845–1856, Nov. 2023.

[26] L. Liu, L. Zhu, Z.-B. Wang, and Y.-R. Zhang, "Proposal and synthesis of self-packaged wideband bandpass power divider with constant power ratio and full phase difference range," *IEEE Trans. Microw. Theory Tech.*, vol. 73, no. 3, pp. 1646–1658, Mar. 2025.

[27] Y. Zhang, H. Liu, S. Chen, Z. Wang, and S. Fang, "All-port-reflectionless wideband filtering power divider using five-line coupled structure," *IEEE Microw. Wireless Technol. Lett.*, vol. 35, no. 1, pp. 31–34, Jan. 2025.

[28] R. Levy and L. F. Lind, "Synthesis of symmetrical branch-guide directional couplers," *IEEE Trans. Microw. Theory Tech.*, vol. 16, no. 2, pp. 80–89, Feb. 1968.

[29] M. C. Horton and R. J. Wenzel, "General theory and design of optimum quarter-wave TEM filters," *IEEE Trans. Microw. Theory Tech.*, vol. 13, no. 3, pp. 316–327, Jan. 1965.

[30] H. J. Carlin and W. Kohler, "Direct synthesis of band-pass transmission line structures," *IEEE Trans. Microw. Theory Tech.*, vol. 13, no. 5, pp. 283–297, Dec. 1965.

[31] L. Zhu, S. Sun, and R. Li, *Microwave Bandpass Filters for Wideband Communications*. New York, NY: Wiley, 2012.

[32] P. Chen, X. Wang, L. Zhu, and G. Lu, "Design of wideband bandpass filters based on three types of coupled stub-loaded resonators," *IEEE Trans. Microw. Theory Tech.*, vol. 73, no. 12, pp. 10617–10631, Dec. 2025.

Haili Zhang received the B.S. degree from Henan University, China, in 2003 and the M.S. degree in material engineering from university of electronic science and technology of China, in 2008. From 2006 to 2009, he was a quality engineer with the Chinese People's Liberation Army 3303 Factory. He has worked in three companies as R&D manager: Dongguan ACE Technology Co. Ltd., Guangdong Shenglu Telecommunication Technology Co. Ltd., and Shenzhen Dafu Telecommunication Technology Co. Ltd. In 2010, he joined Zhejiang Fashion Institute of Technology and founded the faculty of urban railway communication, engaging in management, teaching, and researching. He is currently studying for a Ph.D. degree at the Faculty of Electrical Engineering and Computer Science, Ningbo University. His research interests include RF modules, smart antenna, and radar.

Zhenzhong Chen received the Ph.D. degree in electromagnetic field and microwave technology from Nanjing University of Science and Technology, Nanjing, China, in 2023. He is currently a Lecturer with Ningbo University, Ningbo. He serves as an Active Reviewer for multiple academic journals. His research interests include array antenna, filtering antenna, phased-array antennas, and microwave/millimeter-wave circuit integration.

Taijun Liu (Senior Member, IEEE) received the B.S. degree in applied physics from the China University of Petroleum, Dongying, China, in 1986, the M.Eng. in electrical engineering from the University of Electronic Science and Technology of China, Chengdu, in 1989, and he received the Ph.D. degree at the École Poly technique de Montréal, Université de Montréal, Montréal, QC, Canada, in 2005. He is currently working with Faculty of Electrical Engineering and Computer Science, Ningbo University, as a professor. His current research interests are nonlinear modeling and linearization of wide-band transmitters/power amplifiers, and design of ultra linear highefficiency intelligent power amplifiers for broadband wireless and satellite communications system.

Development of Mesh-Based Generated Reluctance Network Using Trapezoidal Elements Based on Lumped Parameter Model

Dat Vu Van[1], Duc Quang Nguyen[4*], Tuan Phung Anh[1], Chi Phi Do[2], Tung Doan Duc[3], Hao Chen[5], and Vuong Dang Quoc[1*]

[1]School of Electrical and Electronic Engineering
Hanoi University of Science and Technology, Vietnam
dat.vv221904@sis.hust.edu.vn, tuan.phunganh1@hust.edu.vn, vuong.dangquoc@hust.edu.vn

[2]Faculty of Electrical-Electronics
Cao Thang Technical College, Vietnam
dochiphi@caothang.edu.vn

[3]Faculty of Engineering and Technology
Quy Nhon University, Vietnam
tung.doanduc@ qnu.edu.vn

[4] Department of Electrical Engineering
Electric Power University, Viet Nam
quangndhtd@epu.edu.vn

[5] School of Electrical Engineering
China University of Mining and Technology, China
hchen@cumt.edu.cn

[*]Corresponding Authors

Abstract – This paper develops a novel Mesh-Based Generated Reluctance NetWork (MBGRN) model, which is based on the lumped parameter modeling method. The mesh-based approach automates network generation, replacing the manual flux path definitions required in traditional magnetic equivalent circuit (MEC). In this approach, the computational domain is represented in a polar coordinate system where the mesh elements are defined as isosceles trapezoids. The model utilizes a rotation simulation to bypass the remeshing processes common in the finite element method (FEM). A key advantage of the proposed MBGRN method is that the number of computational elements is reduced by half compared to the conventional FEM. This leads to a significant reduction in computation time, ranging from 10 to 15 times faster than traditional FEM, while maintaining a calculation error of less than 1% relative to the FEM. The development of this method is validated through a practical benchmark problem: the surface-mounted permanent magnet synchronous motor under no-load condition. The results obtained from the MBGRN model are thoroughly compared with those from the 2D FEM.

Index Terms – Finite element method, isosceles trapezoidal elements, lumped parameter model, magnetic equivalent circuit, mesh-based generated reluctance network.

I. INTRODUCTION

The traditional finite element method (FEM) is commonly used to calculate and simulate electromagnetic problems with nonlinearities and complex geometric structures [1]. However, high computational costs and extended processing times limit the applicability of the FEM for tasks requiring rapid simulation, parameter sweeping, or the evaluation of multiple rotor configurations during the design stage [2]. This requirement becomes increasingly critical in modern optimization contexts, which demand a substantial number of iterative calculations.

Lumped parameter models (LPMs) have been developed as an approach to reduce computational costs by representing the electromagnetic domain through reluctance networks and magnetomotive force (MMF) sources [3]. The models based on flux tubes or assumed

Submitted On: December 07, 2025
Accepted On: March 27, 2026

https://doi.org/10.13052/2026.ACES.J.410410

flux distributions have been utilized in various electrical machine configurations [4–10]. Nevertheless, these methods rely heavily on geometric assumptions or predefined flux paths; consequently, they may exhibit limitations when applied to complex structures or when accounting for regions of deep saturation.

Another research avenue involves the direct discretization of the computational domain into standard geometric elements [11–16]. These methods enable a more generalized representation of the electromagnetic field, eliminating the need for a priori assumptions regarding flux paths, while offering the capability to accurately capture leakage and fringing phenomena. However, the majority of existing models employ Cartesian grids [3, 12, 17] and none of these cited studies have addressed the implementation of rotary motion. Given that rotating electrical machines inherently exhibit rotational symmetry, the effective exploitation of polar coordinates remains a significant area of potential.

In this context, the paper proposes a mesh-based generated reluctance network (MBGRN) by using trapezoidal elements based on the LPM. The model employs a single element type with a geometry that naturally accommodates the rotationally symmetric structure of rotating machines, facilitating the direct implementation of periodic boundaries. The rotor motion is modeled by shifting element indices along the angular direction, thereby eliminating the requirement for mesh regeneration or interpolation within the air gap region. Furthermore, the model establishes reluctance branches in two principal directions (radial and tangential), enabling the effective representation of leakage fluxes and local saturation effects. To address material nonlinearity, a damped fixed-point iteration algorithm is utilized to ensure convergence stability.

The validation of the proposed model is tested via the benchmark problem on a surface-mounted permanent magnet synchronous machine (SPMSM), specifically through the no-load condition, in which it is compared against the FEM results in terms of both accuracy and computation time. The model also demonstrates good agreement for fundamental electromagnetic quantities across the investigated scenarios, while achieving a significant reduction in computational cost.

The paper is structured as follows. Section II presents the modeling of the mesh element structure. Section III develops mathematic model and application test. Section IV shows the validation test on the practical benchmark problem and discussion. Section V presents conclusions and outlines future research directions.

II. PROPOSED MODEL STRUCTURE

A. Modeling of element mesh structure

A.1. Mesh structure

In rotating electrical machines, the electromagnetic cross-section typically exhibits a circular and centrally symmetric geometry; consequently, the computational domain for the two-dimensional problem is defined in a polar coordinate system (r, θ). Depending on the simulation scope, this domain may be configured as an annular sector when examining a fractional segment of the machine—such as one or multiple stator-rotor pole pitches—or as a closed circular region when analyzing the entire electromagnetic space.

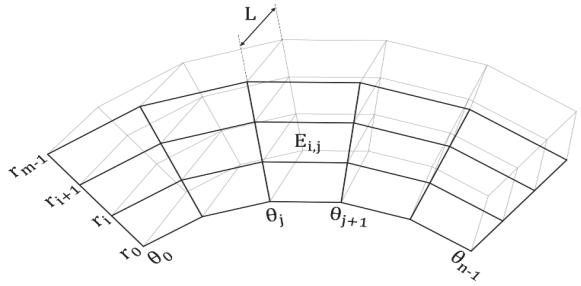

Fig. 1. Modeling of isosceles trapezoidal element mesh.

The domain is discretized using two coordinate vectors: the radial vector $R = [r_0, r_1, \ldots, r_{m-1}]$ and the angular position vector $\Theta = [\theta_0, \theta_1, \ldots, \theta_{n-1}]$. Notably, the angular positions are uniformly spaced to facilitate the implementation of rotor rotation (to be detailed in a subsequent section). These coordinates generate a mesh comprising $N_E = (m-1) \cdot (n-1)$ isosceles trapezoidal elements, each bounded by consecutive radii (r_i, r_{i+1}) and adjacent angles (θ_j, θ_{j+1}), as illustrated in Fig. 1. The advantages of utilizing an isosceles trapezoidal mesh in polar coordinates include a superior capability to conform to the curved boundaries of the computational domain compared to rectangular grids in Cartesian coordinates. Furthermore, the periodic computational domain can be naturally closed by interconnecting elements in the first and last columns. This topology also facilitates the elimination of non-critical elements located inside the rotor yoke (motor shaft) or outside the stator yoke as shown in Fig. 2.

A.2. Elements

Each element comprises a central node connected to four peripheral nodes located at the radial positions (*top* (t), *bottom* (b)) and tangential positions (*right* (r), *left* (l)). These nodes are linked to the center via a branch

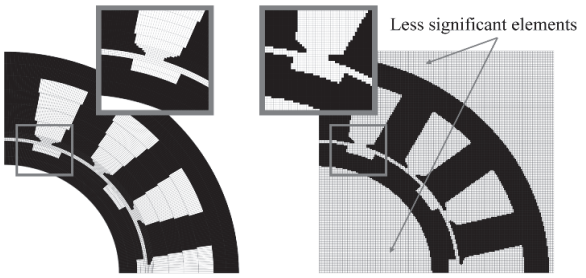

Fig. 2. Isosceles trapezoidal mesh in polar coordinates (left) and rectangular mesh in Cartesian coordinates (right).

consisting of a reluctance in series with a MMF source. By convention, the MMF sources are oriented radially outward for the radial branches (F_t, F_b) and in the clockwise direction for the tangential branches (F_r, F_l). For elements situated at specific boundaries, such as the inner or outer edges, certain nodes or branches may be deactivated in accordance with the imposed boundary conditions as presented in Fig. 3.

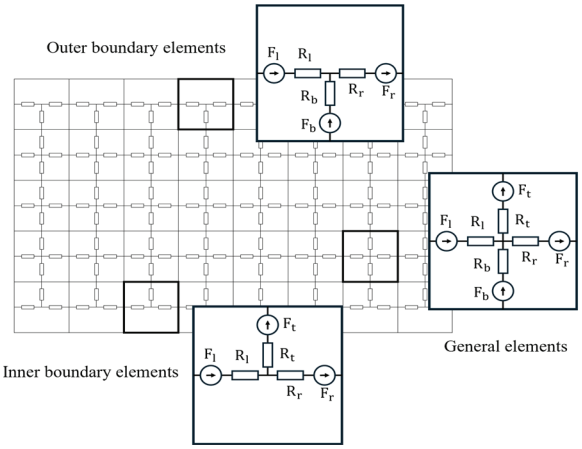

Fig. 3. Structural configuration and spatial distribution of elements within the 2D mesh grid.

The reluctances of element $\mathrm{E_{i,j}}$, bounded by the coordinates $(r_i, r_{i+1}, \theta_j, \theta_{j+1})$ as depicted in Fig. 1, are determined by:

$$R_t = \frac{1}{\mu_0 \mu_r L} \cdot \frac{r_{i+1} - r_i}{3r_{i+1} + r_i} \cdot \cot\left(\frac{|\theta_{j+1} - \theta_j|}{2}\right), \tag{1}$$

$$R_b = \frac{1}{\mu_0 \mu_r L} \cdot \frac{r_{i+1} - r_i}{r_{i+1} + 3r_i} \cdot \cot\left(\frac{|\theta_{j+1} - \theta_j|}{2}\right), \tag{2}$$

$$R_l = R_r = \frac{1}{\mu_0 \mu_r L} \cdot \frac{(r_{i+1} + r_i)\sin\left(\frac{|\theta_{j+1} - \theta_j|}{2}\right)}{(r_{i+1} - r_i)\left[1 + \cos\left(\frac{|\theta_{j+1} - \theta_j|}{2}\right)\right]}, \tag{3}$$

where L denotes the element axial length (m), μ_0 is the permeability of free space, and μ_r is the relative permeability.

A.3. Assigning materials to elements

The spatial region bounded by an element $(r_i, r_{i+1}, \theta_j, \theta_{j+1})$ may physically encompass multiple distinct materials. However, each element is assigned a single homogeneous material property, determined based on the material occupying the predominant surface area. While this discretization approach may induce geometric distortion or staircase artifacts at complex interfaces, these effects can be effectively mitigated by employing a sufficiently fine mesh as pointed out in Fig. 4.

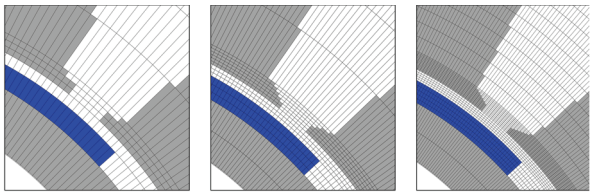

Fig. 4. Computational domain discretized with varying mesh densities.

A.4. Modeling of magnetomotive force sources

For the computational domain of rotating electrical machines, the magnetic field is generated by two primary sources of excitation: permanent magnets (PMs) and windings. Consequently, the MMF sources assigned to the network branches are determined by:

$$F_t = F_b = \frac{1}{2} \cdot (F_m \cos\delta_m + F_w \cos\delta_w), \tag{4}$$

$$F_r = F_l = \frac{1}{2} \cdot (F_m \sin\delta_m + F_w \sin\delta_w), \tag{5}$$

where F_t, F_b, F_r, and F_l denote the branch MMFs for each element as depicted in Fig. 3; δ_m and δ_w represent the angular deviations of the PM magnetization and the winding orientation with respect to the radial axis, respectively; and F_m and F_w correspond to the MMF magnitudes of the magnet and winding, determined by:

$$F_m = H_c \cdot l_m, \quad F_w = I \cdot N, \tag{6}$$

where $F_m(A)$ denotes the magnitude of the PM, $H_c(A/m)$ represents the magnet coercivity, and l_m (m) is the element length along the direction of magnetization. Additionally, $F_w(A)$ indicates the magnitude of the winding MMF, $I = [i_a, i_b, \ldots, i_n]$ is the vector of phase excitation currents, and $N = [N_a, N_b, \ldots, N_n]^T$ is the vector representing the corresponding number of winding turns associated with each element.

B. Boundary conditions

In rotating electrical machine modeling, the computational domain is typically restricted to a fractional segment of the motor, corresponding to one or multiple pole pitches. Consequently, the domain exhibits periodicity along the angular direction (θ). Periodic boundary conditions are applied to the two angular boundaries, as described in [3], ensuring that the magnetic flux distribution at these interfaces is identical, thereby reflecting the inherent symmetry of the electromagnetic structure. In this study, this boundary condition is implemented by interconnecting the elements of the first and last columns via the loop flux variable associated with the final column of the corresponding row, as illustrated in Fig. 5.

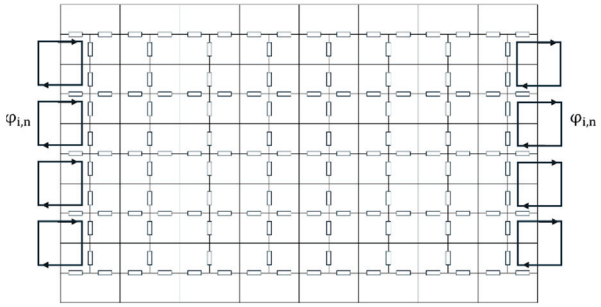

Fig. 5. Application of periodic and parallel boundary condition.

Along the radial coordinate r, the elements situated in the innermost and outermost rows correspond to the inner boundary (e.g., the rotor shaft) and the outer boundary (e.g., the stator housing), respectively. A parallel boundary condition is imposed on these interfaces by eliminating the unconnected reluctances located within the innermost and outermost rows (given already in Fig. 3).

C. Implementation of rotary motion

For rotating electrical machines, it is essential to account for the relative motion between the stator and rotor when calculating time- or position-dependent quantities, like flux linkage and back electromotive force (back EMF). In the proposed mesh-based reluctance network, the angular discretization vector $\Theta = [\theta_0, \theta_1, \ldots, \theta_{n-1}]$ exhibits a uniform spacing of $\Delta_\theta = \theta_{j+1} - \theta_j$. Consequently, the geometric dimensions of all elements situated within the same radial row are identical. This uniformity facilitates the simulation of rotor rotation by an angle $k \cdot \Delta_\theta$ through the simultaneous translation of elements representing the rotating components in the direction of motion via an index-shifting operation:

$$E_{r,j} \leftarrow E_{r,(j+k)\ mod\ n}, \tag{7}$$

where $E_{r,j}$ denotes the elements located in the rows representing the rotating components, k is the discrete angular step, and n is the total element number along the angular direction (θ). The modul operation $(j+k)\ mod\ n$ ensures that any index exceeding the limit wraps around to the initial columns, preserving the cyclic continuity of the domain as shown in Fig. 6.

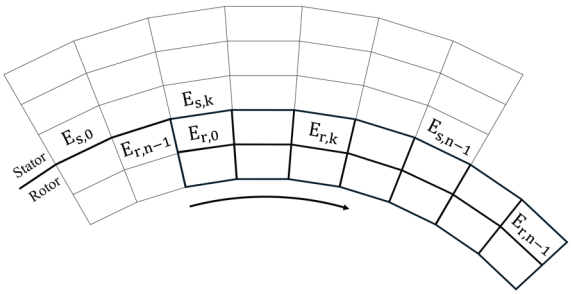

Fig. 6. Illustration of the k-step element shift operation within the rotating domain.

This approach enables the simulation of rotary motion in a natural manner via element index shifting, thereby completely eliminating the need for remeshing or complex interpolation algorithms at the sliding interface. Consequently, this method addresses the fundamental limitations associated with the conventional FEM, such as the moving band technique, which typically incur significant computational overhead due to mesh handling and frequently introduce spurious numerical ripples in torque and EMF waveforms arising from variations in element topology [18–20].

III. MATHEMATIC MODEL AND APPLICATION TEST

A. Application test

To visualize the formulation and solution procedure of the generated mesh-based reluctance network, an illustrative example is conducted using the SPMSM. The machine features a 15-slot/10-pole topology equipped with concentrated windings for the threephase stator. The model is constructed within a twodimensional domain representing the machine's crosssection. The parameters of the proposed motor are given in Table 1.

B. Problem formulation and solution procedure

B.1. Computational domain definition

For electric motors exhibiting periodic and symmetric structures, the entire 2π rad geometry can be decomposed into k identical periodic sectors, where k denotes

Table 1: Specifications of the benchmark SPMSM

Parameter	Value	Unit
Rated power	7500	W
Rated voltage	200	V
Rated current	15	A
Rated speed	1500	rpm
Rated torque	48	N.m
Number of slots	15	–
Stator outer diameter	190	mm
Stator inner diameter	120	mm
Tooth width	15	mm
Slot depth	25	mm
Slot opening depth	1	mm
Slot opening width	5	mm
Tooth tip angle	30	mm
Rated power	7500	W
Rated voltage	200	V
Rated current	15	A
Rated speed	1500	rpm
Rated torque	48	N.m
Number of poles	10	–
Magnet thickness	3	mm
Magnet coercivity	852	kA/m
Magnet arc	140	degree
Air gap length	1.5	mm
Shaft diameter	96	mm
Number of phases	3	–
Winding type	Concentrated	–
Turns per phase	25	turns

the symmetry order. Leveraging this symmetry, the computational burden can be significantly reduced by simulating a single periodic sector rather than the entire machine. Periodic boundary conditions are imposed at the sector boundaries to ensure that the simulation results accurately reflect the magnetic field and current distribution of the full machine. Figure 7 illustrates the computational domain configured for the benchmark motor using the parameters listed in Table 1, where an adaptive mesh is employed.

C. Formulation of the system of equations

Two primary approaches exist for interconnecting mesh elements: the nodal magnetic potential method and the loop flux method [3]. In this study, the loop flux formulation is adopted to establish and solve the governing system of equations. Consider a mesh comprising $n_r \times n_\theta$ elements. Given the imposed boundary conditions, a total of $m = (n_r - 1) \cdot n_\theta$ loop flux variables

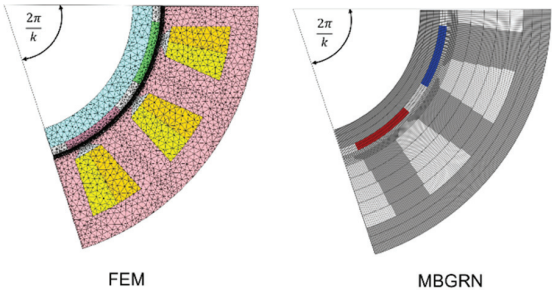

Fig. 7. Reduced periodic computational domain.

are required to fully interconnect the elements within the computational domain. The matrix system is defined as:

$$R(\Phi) \cdot \Phi = F, \tag{8}$$

where $R \in R^{m \times m}$ denotes the reluctance matrix, $\Phi \in R^{m \times \mathbb{1}}$ represents the vector of loop flux variables, and $F \in R^{m \times \mathbb{1}}$ corresponds to the MMF source vector.

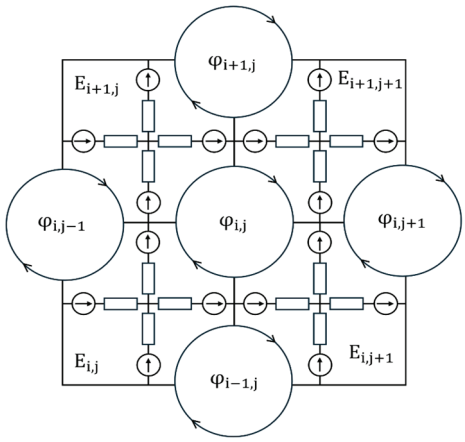

Fig. 8. Components involved in a mesh equation.

Figure 8 illustrates the components constituting the equation associated with the loop flux variable (i, j). These include the central variable $\varphi_{i,j}$ and its neighboring variables $\varphi_{i+1,j}, \varphi_{i,j+1}, \varphi_{i-1,j}, \varphi_{i,j-1}$, along with the corresponding elements $E_{i,j}, E_{i+1,j}, E_{i+1,j+1}$, and $E_{i,j+1}$.

The governing equation connecting the elements at this specific location is formulated by ensuring that the algebraic sum of magnetic voltage drops around the closed loop equates to zero. Loop flux variables that are rendered invalid due to the imposed boundary conditions are constrained to zero [3]:

$$\begin{aligned}
&\varphi_{i,j}(R_{l,E_{i+1,j}} + R_{r,E_{i+1,j+1}} + R_{b,E_{i+1,j+1}} + R_{t,E_{i,j+1}} \\
&\quad + R_{l,E_{i,j+1}} + R_{r,E_{i,j}} + R_{t,E_{i,j}} + R_{b,E_{i+1,j}}) \\
&\quad - \varphi_{i+1,j}(R_{l,E_{i+1,j}} + R_{r,E_{i+1,j+1}}) \\
&\quad - \varphi_{i,j+1}(R_{b,E_{i+1,j+1}} + R_{t,E_{i,j+1}})
\end{aligned}$$

$$
\begin{aligned}
&-\varphi_{i-1,j}(R_{l,E_{i,j+1}}+R_{r,E_{i,j}})\\
&-\varphi_{i,j-1}(R_{t,E_{i,j}}+R_{b,E_{i+1,j}})\\
&=F_{l,E_{i+1,j}}+F_{r,E_{i+1,j+1}}-F_{b,E_{i+1,j+1}}-F_{t,E_{i,j+1}}\\
&-F_{l,E_{i,j+1}}-F_{r,E_{i,j}}+F_{t,E_{i,j}}+F_{b,E_{i+1,j}}. \qquad (9)
\end{aligned}
$$

Equation (9) exhibits a nonlinear nature, as the elements within the reluctance matrix R are directly dependent on the material properties (μ_r and B). Rather than employing the Newton-Raphson method, which is known to be sensitive to discontinuities in the derivative of the magnetization curve, this study selects the Fixed-Point Iteration method due to its inherent simplicity and robustness [21, 22]. To mitigate numerical oscillations frequently observed in regions of deep saturation, an under-relaxation technique is integrated into the solution update process. Consequently, the solution at the $(k+1)$-th iteration is modulated via a relaxation coefficient t_n:

$$\Phi_{k+1}=(1-t_n)\Phi_k+t_n(R(\Phi_k)^{-1}F), \qquad (10)$$

where Φ_k denotes the loop flux vector at the current iteration k, R represents the reluctance matrix, F corresponds to the source vector, and t_n is the underrelaxation factor (where $0<t_n\leq 1$). In this study, the relaxation factor is empirically selected within the range of $0.1\leq t_n\leq 0.3$. The detailed solution procedure is schematically illustrated in Fig. 9.

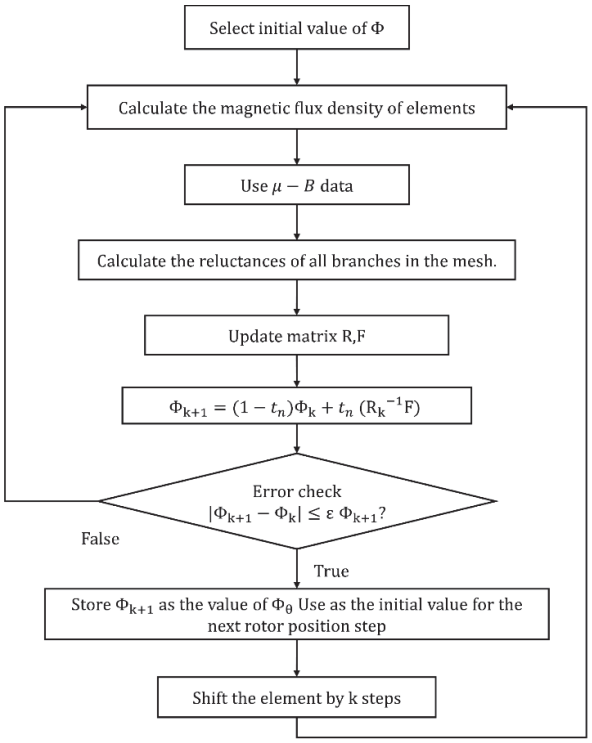

Fig. 9. Flowchart of the solution procedure using damped fixed-point iteration.

D. Computation of electromagnetic quantities

D.1. Magnetic flux distribution

Upon obtaining the solution to Equation (9), the magnetic fluxes flowing through the element branches are determined through the algebraic combination of the associated loop flux variables, governed by the following rule:

$$\varphi_{t,E_{i,j}}=-\varphi_{i,j-1}+\varphi_{i,j}, \qquad (11)$$

$$\varphi_{r,E_{i,j}}=-\varphi_{i,j}+\varphi_{i-1,j}, \qquad (12)$$

$$\varphi_{b,E_{i,j}}=-\varphi_{i-1,j-1}+\varphi_{i-1,j}, \qquad (13)$$

$$\varphi_{l,E_{i,j}}=-\varphi_{i,j-1}+\varphi_{i-1,j-1}. \qquad (14)$$

The magnetic flux density within each element is determined based on its geometric dimensions and the respective branch flux values:

$$B^2_{E_{i,j}}=B^2_{r,E_{i,j}}+B^2_{\theta,E_{i,j}} \qquad (15)$$

$$B_{r,E_{i,j}}=\frac{\varphi_{t,E_{i,j}}+\varphi_{b,E_{i,j}}}{A_{t,E_{i,j}}+A_{b,E_{i,j}}}, \qquad (16)$$

$$B_{\theta,E_{i,j}}=\frac{\varphi_{r,E_{i,j}}+\varphi_{l,E_{i,j}}}{A_{r,E_{i,j}}+A_{l,E_{i,j}}}. \qquad (17)$$

The magnetic flux density distribution on the benchmark motor is presented in Fig. 10.

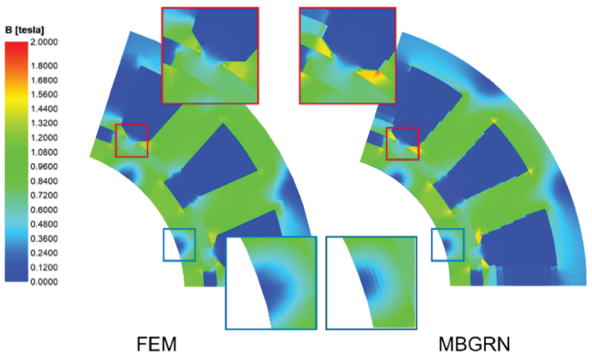

Fig. 10. Comparative magnetic flux density distributions between FEM and MBGRN at a specific rotor position.

The comparative magnetic flux density distributions between FEM and MBGRN at a specific rotor position are shown in Fig. 10. It can be demonstrated that the magnetic flux distribution calculated by the MBGRN method exhibits a high degree of consistency with that obtained from the FEM. Notably, complex electromagnetic phenomena, including local saturation, leakage flux, and magnetically inactive regions, are accurately captured. This confirms that the MBGRN

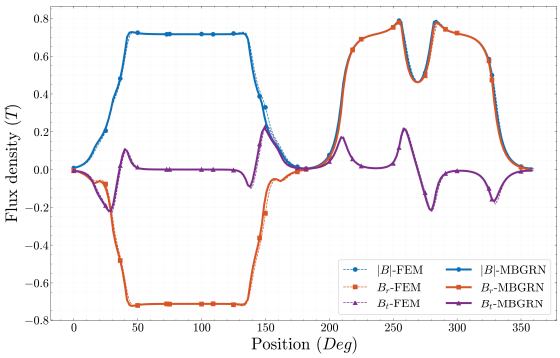

Fig. 11. Comparison of air-gap magnetic flux density distribution between FEM and MBGRN.

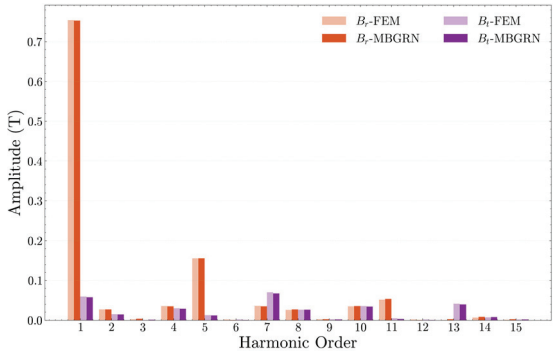

Fig. 12. Harmonic spectrum of the air-gap flux density: Comparison between FEM and the proposed MBGRN.

method achieves a generalized representation of the electromagnetic field without requiring the a priori definition of flux paths, a constraint typical of classical magnetic equivalent circuit (MEC) approaches. Furthermore, the identification of these magnetically inactive regions suggests the potential applicability of the proposed method for multi-physics optimization (e.g., via axial material removal) as investigated in [23, 24].

The following quantitative analyses are performed to objectively evaluate the proposed MBGRN method. The magnetic flux density distribution at the air gap is presented in Fig. 11. Specifically, the statistical results show that the average magnitude of the flux density ($|B|$) calculated by MBGRN is 0.4719 T, representing a negligible error of 0.36% compared to the 0.4736 T obtained from FEM. Furthermore, for the radial component (B_r), the MBGRN yields an RMS value of 0.5475 T and a peak value of 0.7794 T, which are in excellent agreement with the FEM results of 0.5481 T (0.1% error) and 0.7731 T, respectively. Moreover, the harmonic analysis of both B_r and B_t components illustrated in Fig. 12 also reveals highly consistent results, further verifying the accuracy of the proposed method in the spectral domain. This high consistency, both numerically and visually, validates that the MBGRN, using isosceles trapezoidal elements, accurately captures the electromagnetic field distribution.

D.2. Flux linkage

The flux linkage associated with the i-th phase is determined by:

$$\lambda_i = k \cdot \sum_{k=0}^{n_E} N_{i,E_k} \cdot \varphi_d, \tag{18}$$

where λ_i denotes the flux linkage of phase i, k represents the magnetic circuit symmetry factor, n_E is the total number of elements within the reluctance network, N_{i,E_k} is the number of turns of phase i wound on element E_k, and φ_d is the flux component flowing through element E_k in the direction orthogonal to the winding cross-section. The calculated phase flux linkages are illustrated in Fig. 13. Specifically, for Phase A, the MBGRN yields a peak flux linkage of 0.2375 Wb and an RMS value of 0.1613 Wb, demonstrating excellent agreement with the FEM results of 0.2399 Wb and 0.1629 Wb, respectively. The maximum relative errors for the peak and RMS values across all phases are approximately 1.04% and 1.13%, respectively. Furthermore, the harmonic analysis presented in Fig. 14 shows a high level of consistency in the spectral domain, confirming that the proposed MBGRN accurately captures the fundamental and harmonic components of the flux linkage compared to the FEM.

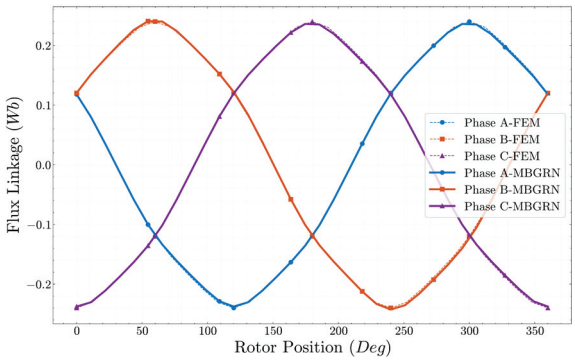

Fig. 13. Distribution of flux linkage.

D.3. Back electromotive force

The back EMF of the i-th phase is determined by the time derivative of the corresponding flux linkage:

$$e_i = -\frac{d\lambda_i}{dt}. \tag{19}$$

The phase back-EMF results, obtained by calculating the time-derivative of the phase flux linkages, are illustrated in Fig. 15. The proposed MBGRN method accurately

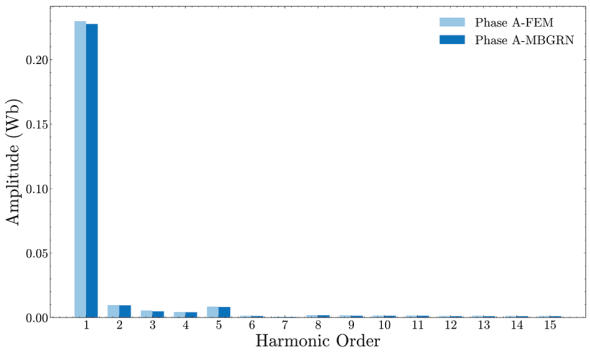

Fig. 14. Harmonic spectrum of the flux linkage: comparison between FEM and MBGRN.

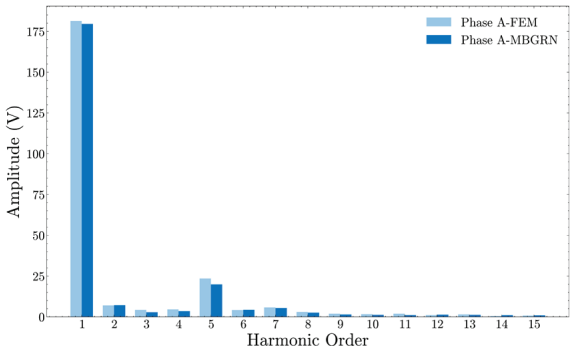

Fig. 16. Harmonic spectrum of the back EMF: comparison between FEM and MBGRN.

predicts the induced voltage, maintaining a high degree of consistency with the FEM results in terms of both peak and root mean square (RMS) magnitudes. Specifically, for Phase A, the MBGRN yields a peak back-EMF of 193.92 V and an RMS value of 128.09 V, showing excellent agreement with the FEM results of 197.03 V and 129.69 V, respectively. The maximum relative error for the peak voltage across all phases is approximately 1.57%, while the RMS deviation remains within 1.6%. Furthermore, the harmonic analysis presented in Fig. 16 substantiates this accuracy in the spectral domain, confirming that the fundamental and higher-order components, including ripples caused by slot openings, are effectively captured by the MBGRN method.

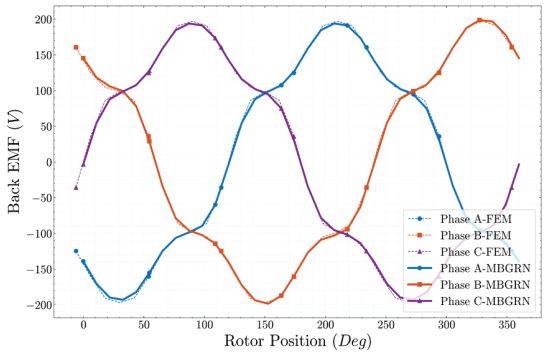

Fig. 15. Distribution of back EMF.

D.4. Electromagnetic and cogging torque

For two-dimensional electromagnetic field models, the electromagnetic torque (T_e) can be computed by integrating the Maxwell stress tensor as detailed in [25]:

$$T_e = k \cdot \frac{L}{\mu_o} \int_0^{\frac{2\pi}{k}} r^2 B_r B_\theta d\theta, \tag{20}$$

where k is the magnetic circuit symmetry factor, L is the active axial length of the machine, r is closed surface of radius, B_r and B_θ represent the radial and tangential magnetic flux densities, respectively.

In the MBGRN model, Equation (20) is discretized, where $E_{i_g,j}$ denotes the elements situated in the i_g-th row (representing the stator-rotor air gap):

$$T_e = k \cdot \frac{L}{\mu_o} \sum_{j=1}^{n} r_{E_{i_g,j}}^2 B_{r,E_{i_g,j}} B_{t,E_{i_g,j}} \Delta\theta. \tag{21}$$

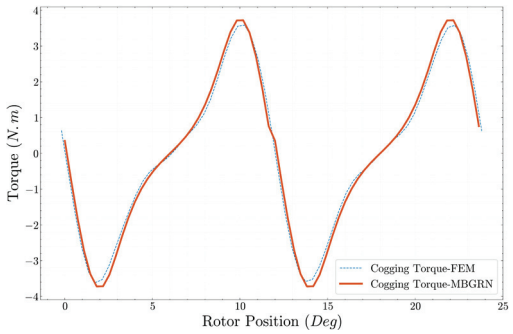

Fig. 17. Cogging torque simulation results.

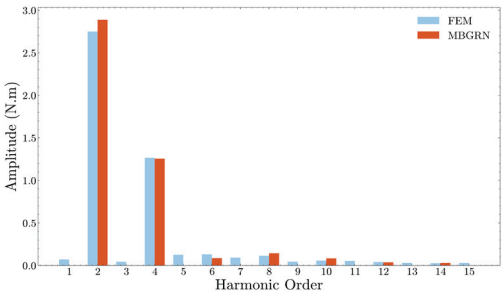

Fig. 18. Harmonic spectrum of the cogging torque: comparison between FEM and MBGRN.

The cogging torque characteristics, which are highly sensitive to mesh density and geometric accuracy, are illustrated in Fig. 17. The comparison shows that the proposed MBGRN method effectively predicts the

cogging torque profile, with results closely matching the FEM data. Specifically, the MBGRN yields a peak cogging torque of 3.72 Nm and an RMS value of 2.23 Nm, compared to the FEM results of 3.61 Nm and 2.15 Nm, respectively. The maximum relative error for the peak value is approximately 2.98%, while the RMS deviation remains within 3.8%. Furthermore, the harmonic analysis presented in Fig. 18 confirms that the MBGRN accurately captures the dominant harmonic components of the cogging torque, demonstrating the reliability of the proposed model in evaluating parasitic torque components.

IV. BENCHMARKING AND VALIDATION

To assess the accuracy and efficiency of the proposed MBGRN, a parametric study is conducted by varying key parameters that exert a significant influence on the computational results. The evaluated parameters include number of mesh elements (which governs both computational speed and solution accuracy), air gap length (a critical determinant of the main flux magnitude), and magnet thickness (which directly correlates with the magnitude of the MMF sources).

To objectively quantify the agreement between the two waveforms, the Normalized Root Mean Square Error (NRMSE) is utilized:

$$NRMSE = \frac{\sqrt{\frac{1}{n}\sum_{i=1}^{n}(y_i - \widehat{y}_i)^2}}{y_{max} - y_{min}}, \tag{22}$$

where n is the total number of data samples, y_i represents the reference value (FEM) at the i-th data point, $\widehat{y}_i$ indicates the computed value (MBGRN) at the i-th sample, and y_{max} and y_{min} correspond to the maximum and minimum values within the reference dataset, respectively.

The results presented in the subsequent sections were obtained on a workstation featuring a 4-core Intel Core i7-7660U CPU at 2.50 GHz and 8 GB of RAM. The proposed MBGRN algorithm was implemented in Python 3.13 and validated against Ansys Motor-CAD as the industry-standard FEA tool.

A. Sensitivity analysis of mesh resolution

In this section, a comparative evaluation is performed on both the FEM and MBGRN by varying the mesh element count for both methods. The primary objectives are to assess the computational speed of the MBGRN and to establish an equitable mesh configuration, thereby ensuring a fair baseline for subsequent comparisons.

Figures 19 and 20 indicate that the convergence solutions on both the FEM and MBGRN to a stable solution as the number of mesh elements becomes sufficiently large. Notably, the MBGRN method exhibits

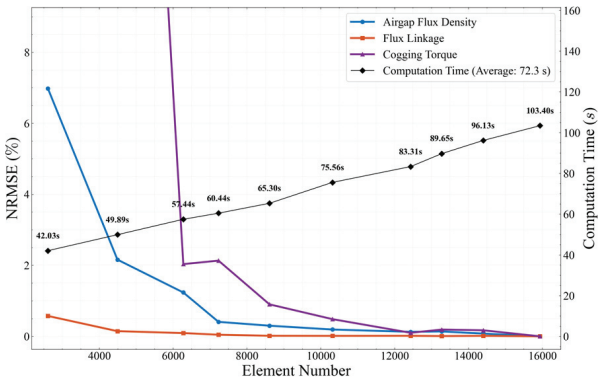

Fig. 19. Convergence solution on the mesh of FEM.

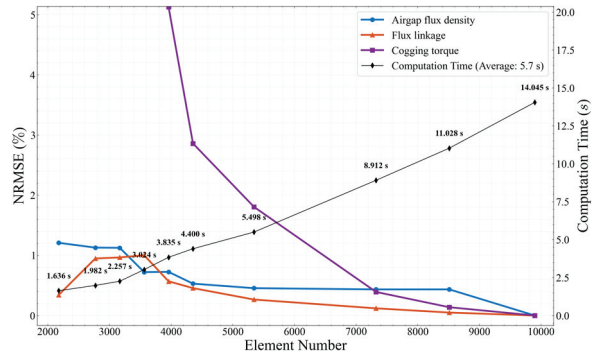

Fig. 20. Convergence solution on mesh of MBGRN.

an average computational speedup of 12.7 times, while requiring an element count approximately half that of the FEM to achieve comparable accuracy. The deviation relative to the method's asymptotic reference value remains below 2% (representing a mesh density sufficient for convergence).

B. Sensitivity analysis of physical parameters

Figures 21 and 22 assess the robustness and accuracy of the MBGRN model under variations in critical physical parameters: air gap length and magnet thickness. The results are presented in terms of the NRMSE, quantifying the discrepancy with the reference FEM results.

Figure 21 shows the error and computation time as the air gap length is varied (0.5 mm to 5 mm). The discrepancies for Flux Linkage and Back EMF remain exceptionally low, consistently below 1% across the entire range of air gap lengths tested. This confirms the MBGRN's high reliability in predicting the main flux magnitude, regardless of the air gap size. Discrepancies for air-gap flux density are maintained below 3%, while the cogging torque error remains below 6% throughout the entire range of air-gap length variations. The MBGRN consistently maintains an average speed up of

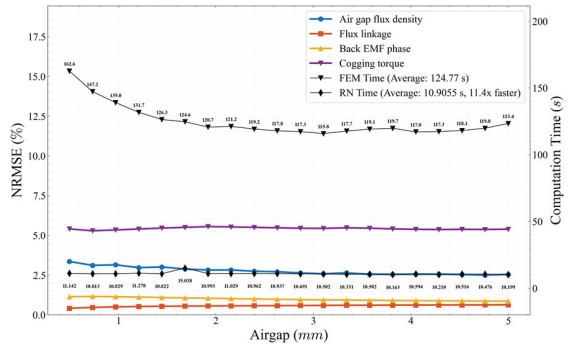

Fig. 21. Discrepancy between MBGRN and FEM under air-gap length variations.

11.4 times over FEM computation time throughout the variation. Figure 22 shows the error and computation time as the magnet thickness is varied (0.5 mm to 4 mm). Similar to the air gap analysis, the NRMSE for flux linkage and back EMF remains very low, consistently below 1%. This confirms the model's robust performance in predicting these core quantities even when the MMF source magnitude is changed. The NRMSE for air-gap flux density is consistently maintained below 5%, while the cogging torque error gradually increases with magnet thickness, reaching approximately 6% at a thickness of 4 mm. The significant advantage in computation speed is maintained, with the MBGRN being an average of 10.9 times faster than the FEM.

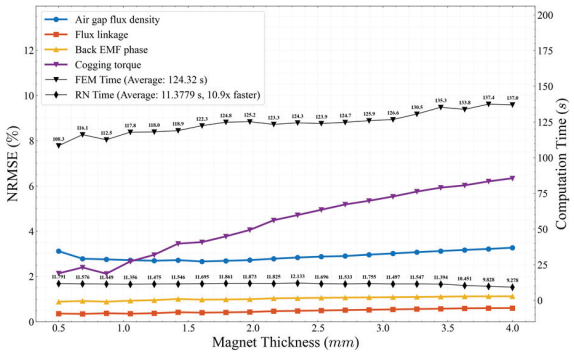

Fig. 22. Discrepancy between MBGRN and FEM under magnet thickness variations.

V. CONCLUSION

This paper has successfully developed and implemented the MBGRN model within a polar coordinate system. This encompasses the entire modeling process, including mesh generation using isosceles trapezoidal elements, material assignment, system formulation, nonlinear handling, and the simulation of rotary motion via a unique index-shifting technique. This approach eliminates the requirement for mesh regeneration or complex interpolation algorithms at the sliding interface, providing a more natural representation of motion compared to conventional FEM techniques. As an LPM, the MBGRN is a discrete approximation that effectively accounts for local magnetic saturation. While it is not intended to replace high-fidelity FEM continuum analysis, it serves as an efficient alternative for rapid design. Optimized for rotational symmetry, the current framework is limited to symmetric domains and does not account for asymmetric configurations such as rotor eccentricity. For these symmetric cases, MBGRN offers significant speed advantages in parameter sweeping while maintaining the ability to capture nonlinear magnetic behavior. Validation results obtained from the SPMSM under the no-load condition demonstrate that the model achieves high accuracy. Specifically, it yields discrepancies of less than 1% for primary quantities such as flux linkage and back EMF. Discrepancies are also below 5% for air-gap magnetic flux density and cogging torque. Furthermore, the model achieves a computational speedup of 10 to 15 times compared to the FEM. This speedup is realized while requiring approximately half the number of elements. These findings confirm the potential of the MBGRN for applications requiring rapid simulation, parametric analysis, and design optimization of rotating electrical machines. The significant reduction in computation time confirmed in this study is especially critical for expanding this framework to 3D models, where the computational cost of traditional FEM often becomes prohibitive.

Building upon the proposed MBGRN framework and the robust iterative solver, future research directions will focus on several key areas:

- Expanding application to machines with stronger nonlinearity (IPMSM, SynRM).
- Investigation of full-load conditions and the incorporation of magnetic losses within the magnetic circuit.
- Prioritizing a 3D model to capture axial end effects and end-winding leakage flux, maximizing speed advantage over 3D FEM.
- Integrating with topology optimization for multi-physics challenges, particularly optimizing rotor voids for inertia reduction and enhanced cooling.

The full source code of the proposed method is given at: https://github.com/iamvuvandat/Mesh_Based_Reluctance_Generated_Network_2D. The provided GitHub repository includes the following key components and scripts:

- Core solver with nonlinear magnetic iteration.
- Mesh generation tools in polar coordinates using isosceles trapezoidal elements.

- Scripts for computing flux density, flux linkage, back EMF and cogging torque.
- Benchmark configurations used in this paper to ensure reproducibility.

ACKNOWLEDGMENT

This research is funded by Hanoi University of Science and Technology (HUST) under project number T2025-PC-082.

REFERENCES

[1] M. N. Sadiku, "A simple introduction to finite element analysis of electromagnetic problems," *IEEE Transactions on Education*, vol. 32, no. 2, pp. 85–93, 2002.

[2] G. Lei, J. Zhu, Y. Guo, C. Liu, and B. Ma, "A review of design optimization methods for electrical machines," *Energies*, vol. 10, no. 12, p. 1962, 2017.

[3] S. Yang, S. Asfirane, S. Hlioui, S. Mezani, G. Krebs, and Y. Amara, "Introduction to mesh based generated lumped parameter models for electromagnetic problems," *CES Transactions on Electrical Machines and Systems*, vol. 5, no. 2, pp. 152–162, 2021.

[4] E. Fleurot, F. Scuiller, and J.-F. Charpentier, "Analytical models for fast and accurate calculation of electromagnetic performances of segmented permanent magnet synchronous machines with large angular gaps," *Applied Sciences*, vol. 11, no. 1, p. 459, 2021.

[5] R. M. Bhashini and K. Ragavan, "Magnetic equivalent circuit for surface-mounted pm motor," in *2018 IEEE International Conference on Power Electronics, Drives and Energy Systems* (*PEDES*), pp. 1–5, 2018.

[6] S.-M. Kim, W.-S. Jung, W.-H. Kim, T.-K. Bang, D.-H. Lee, Y.-J. Kim, and J.-Y. Choi, "Optimal design of permanent magnet synchronous machine based on random walk method and semi 3D magnetic equivalent circuit considering overhang effect," *Energies*, vol. 15, no. 21, p. 7852, 2022.

[7] C. Rasmussen and E. Ritchie, "A magnetic equivalent circuit approach for predicting PM motor performance," in *IAS'97. Conference Record of the 1997 IEEE Industry Applications Conference Thirty Second IAS Annual Meeting*, vol. 1, pp. 10–17, 1997.

[8] L. Dang, N. Bernard, N. Bracikowski, and G. Berthiau, "Analytical model and reluctance network for high-speed PMSM design optimization application to electric vehicles," in *2016 XXII International Conference on Electrical Machines* (*ICEM*), pp. 1359–1365, 2016.

[9] R. Jayarajan, N. Fernando, A. Mahmoudi, and N. Ullah, "Magnetic equivalent circuit modelling of synchronous reluctance motors," *Energies*, vol. 15, no. 12, p. 4422, 2022.

[10] V. Naeini and N. Sadeghi, "Optimum design of the outer rotor brushless DC permanent magnet motor with minimum torque ripples," *Journal of Operation and Automation in Power Engineering*, vol. 14, no. 1, pp. 70–76, 2026.

[11] S. Yang, Y. Amara, W. Hua, and G. Barakat, "Development of a generic framework for lumped parameter modeling," *Open Physics*, vol. 18, no. 1, pp. 365–373, 2020.

[12] S. Ouagued, Y. Amara, and G. Barakat, "Comparison of hybrid analytical modelling and reluctance network modelling for pre-design purposes," *Mathematics and Computers in Simulation*, vol. 130, pp. 3–21, 2016.

[13] K. Pluk, J. Jansen, and E. Lomonova, "3-D hybrid analytical modeling: 3-D Fourier modeling combined with mesh-based 3-D magnetic equivalent circuits," *IEEE Transactions on Magnetics*, vol. 51, no. 12, pp. 1–14, 2015.

[14] Z. Liu, C. Tang, Y. He, and J. Chen, "A 2D generalized equivalent magnetic network model for electromagnetic performance analysis of surface-mounted permanent magnet electric machines," *Electronics*, vol. 14, no. 8, p. 1642, 2025.

[15] W. Lu, J. Zhu, Y. Fang, and P.-D. Pfister, "A hybrid analytical model for the electromagnetic analysis of surface-mounted permanent-magnet machines considering stator saturation," *Energies*, vol. 16, no. 3, p. 1300, 2023.

[16] S. Asfirane, S. Hlioui, Y. Amara, and M. Gabsi, "Study of a hybrid excitation synchronous machine: Modeling and experimental validation," *Mathematical and Computational Applications*, vol. 24, no. 2, p. 34, 2019.

[17] D. Ceylan, L. A. Friedrich, K. O. Boynov, and E. A. Lomonova, "Convergence analysis of the fixed-point method with the hybrid analytical modeling for 2-D nonlinear magnetostatic problems," *IEEE Transactions on Magnetics*, vol. 57, no. 2, pp. 1–5, 2020.

[18] X. Shi, Y. Le Menach, J.-P. Ducreux, and F. Piriou, "Comparison of slip surface and moving band techniques for modelling movement in 3D with FEM," *COMPEL-The International Journal for Computation and Mathematics in Electrical and Electronic Engineering*, vol. 25, no. 1, pp. 17–30, 2006.

[19] S. L. Ho, W. Fu, and H. Wong, "Direct modeling of the starting process of skewed rotor induction motors using a multi-slice technique," *IEEE Transactions on Energy Conversion*, vol. 14, no. 4, pp. 1253–1258, 2002.

[20] A. Demenko, "Movement simulation in finite element analysis of electric machine dynamics," *IEEE Transactions on Magnetics*, vol. 32, no. 3, pp. 1553–1556, 1996.

[21] E. Dlala, A. Belahcen, and A. Arkkio, "A fast fixed-point method for solving magnetic field problems in media of hysteresis," *IEEE Transactions on Magnetics*, vol. 44, no. 6, pp. 1214–1217, 2008.

[22] A. Zhou, D. Lin, C. Lu, M. Rosu, and D. Ionel, "An adaptive fixed-point iteration algorithm for finite element analysis with magnetic hysteresis materials," *IEEE Transactions on Magnetics*, vol. 53, no. 10, pp. 1–5, 2017.

[23] T. CherriÃ¨re, S. Hlioui, L. Laurent, F. Louf, H. B. Ahmed, and M. Gabsi, "Topology optimization of asymmetric PMSM rotor," in *2022 International Conference on Electrical Machines* (*ICEM*), pp. 469–475, 2022.

[24] S. Sato, T. Sato, and H. Igarashi, "Topology optimization of synchronous reluctance motor using normalized gaussian network," *IEEE Transactions on Magnetics*, vol. 51, no. 3, pp. 1–4, 2015.

[25] D. M. Ionel, M. Popescu, M. I. McGilp, T. Miller, and S. J. Dellinger, "Assessment of torque components in brushless permanent-magnet machines through numerical analysis of the electromagnetic field," *IEEE Transactions on Industry Applications*, vol. 41, no. 5, pp. 1149–1158, 2005.

Dat Vu Van is currently a student at the School of Electrical and Electronic Engineering, Hanoi University of Science and Technology, Vietnam. His research interests include the modeling of electrical machines, analytical and finite element methods.

Duc Quang Nguyen received his Engineer diploma degree from the Hanoi University of Science and Technology, Vietnam, in 2007; M.S. from Lille 1 University, France, in 2009, and Ph.D. from the Ecole Nationale Superieure d'Arts et Metiers Paristech, France, in 2013. All were in electrical engineering. He is currently a Lecturer in the Department of Electrical Engineering, at the Electric Power University, Vietnam. His research interests are in the fields of numerical modeling methods, electromagnetic field, electrical machines, and BESS.

Tuan Phung Anh obtained his Ph.D. degree in Electrical Engineering in 2006 from Grenoble Institute of Technology (Grenoble INP), France. He is currently a Senior Lecturer at the Faculty of Electrical Engineering, School of Electrical and Electronic Engineering, Hanoi University of Science and Technology (HUST), Vietnam. His research interests include electromagnetic design, optimization algorithms, magnetic field stealth, and the application of advanced materials in electrical engineering.

Chi Phi Do is a Dean in Electrical-Electronic Engineering, Cao Thang Technical College, Ho Chi Minh City, Vietnam. He received his Ph.D. from Hanoi University of Science and Technology in 2016. His research interests include electrical engineering, electrical installation skills, design and install of solar or lighting systems, ability to operate, assemble, maintain electrical equipment, electrical systems, and solve problems related to electricity and equipment in the production.

Tung Doan Duc received the B.Eng. degree in Electrical Engineering in 2000, the M.Eng. degree in Electrical Engineering in 2004, and the Ph.D. degree in Electrical Engineering in 2009, all from Hanoi University of Science and Technology, Vietnam. He is currently Rector of Quy Nhon University. He became an Associate Professor in 2019. His research interests include electrical machines, optimization techniques in electrical machines and power systems, and smart grids.

Hao Chen (Senior Member, IEEE) received the B.S. and Ph.D. degrees in electrical engineering from the Department of Automatic Control, Nanjing University of Aeronautics and Astronautics, Nanjing, China, in 1991 and 1996, respectively. In 1998, he became an Associate Professor at the School of Information and Electrical Engineering, China University of Mining and Technology, Xuzhou, where he has been a Professor since 2001. From 2002 to 2003, he was a Visiting Professor at Kyungsung University, Busan, South Korea. Since 2008, he is Adjunct Professor at The University of Western Australia, Perth, WA, Australia. He is the author of one book and has authored more than 300 papers. He holds 15 US patents, 87 Chinese invention patents, and six Chinese utility model patents.

Vuong Dang Quoc received his Ph.D. degree in 2013 from the Faculty of Applied Sciences at the University of Liège in Belgium. He joined Hanoi University of Science and Technology in September 2013, where he is currently working as a deputy director, Training Center of Electrical Engineering, School of Electrical Engineering, University of Science and Technology, Hanoi, Vietnam. He became an associate professor in 2020. Dang Quoc Vuong's research domain encompasses modeling of electromagnetic systems, electrical machines, optimization method, numerical methods, and subproblem methods.